DOT/FAA/TC-18/7

Federal Aviation Administration
William J. Hughes Technical Center
Aviation Research Division
Atlantic City International Airport
New Jersey 08405

Low-Cost Accurate Angle of Attack System

January 2018

Final Report

U.S. Department of Transportation
Federal Aviation Administration

NOTICE

Technical Report Documentation Page

1. Report No.	2. Government Accession No.	3. Recipient's Catalog No.
DOT/FAA/TC-18/7		

4. Title and Subtitle	5. Report Date
LOW-COST ACCURATE ANGLE OF ATTACK SYSTEM	January 2018
	6. Performing Organization Code

7. Author(s)	8. Performing Organization Report No.
David F. Rogers, Borja Martos[1], and Francisco Rodrigues[1]	

[1] Embry-Riddle Aeronautical University Eagle Flight Research Center/College of Engineering 1585 Aviation Parkway, Suite 606 Daytona Beach, FL 32114	10. Work Unit No. (TRAIS)
	11. Contract or Grant No. 2014-G-013

12. Sponsoring Agency Name and Address	13. Type of Report and Period Covered
U.S. Department of Transportation Federal Aviation Administration Central Regional Office 901 Locust St Kansas City, MO 64106	Final Report
	14. Sponsoring Agency Code AIR-690

15. Supplementary Notes

The FAA William J. Hughes Technical Center Aviation Research Division COR was Robert J. McGuire.

16. Abstract

A low-cost ($100/see table A-1 of appendix A) differential pressure-based commercial off-the-shelf (COTS) angle of attack (AoA) data acquisition system was designed, successfully reduced to practice, wind tunnel tested, and flight tested. The accuracy of the differential pressure AoA system was determined to be ¼ to ½ of a degree. The repeatability of the data from the COTS system was excellent. Using un-normalized differential pressure (P_{fwd}-P_{45}) does not provide adequate accuracy throughout the aircraft's AoA range. This technique is dynamic pressure-dependent. For a limited range of high angles of attack near stall, a linear fit to the data provides adequate accuracy. However, the accuracy at low AoA, such as those required by cruise, is poor. Therefore, systems similar to that tested using a linear calibration are basically stall warning devices. A physics-based determination of AoA was successful, provided that a reasonably accurate aircraft lift curve was determined. The calculation of the lift curve slope was within 0.01 degrees of the value determined by the flight test using an alpha/beta probe. A calibration curve based on the ratio of P_{fwd}/P_{45} was studied and determined to be linear throughout the aircraft's AoA when the probe was located on the wing's lower surface between an estimated 25% and 60% of the local wing chord.

17. Key Words	18. Distribution Statement
Angle of attack, General aviation, Sensors, Instrumentation	This document is available to the U.S. public through the National Technical Information Service (NTIS), Springfield, Virginia 22161. This document is also available from the FAA William J. Hughes Technical Center at actlibrary.tc.faa.gov.

19. Security Classif. (of this report)	20. Security Classif. (of this page)	21. No. of Pages	22. Price
Unclassified	Unclassified	117	

ACKNOWLEDGEMENTS

Dave Rogers gratefully acknowledges the critical contributions of Francisco Rodriguez, specifically his conversion of concepts into electronic and computer code. He also acknowledges the professional support of Borja Martos, of Eagle Flight Research Center, for the exceptional conduct of the flight test program. Martos is an outstanding flight test engineer and a superb pilot whose skills facilitated excellent datasets.

Rogers also acknowledges the support of Peter Osterc, Alfonso Noriega, and Yosvanny Alonso, students of the Eagle Flight Research Center, for their efforts as computer flight test engineers on the various test flights.

Additionally, Rogers wishes to thank Dave Sizoo of the FAA Small Airplane Directorate and Bob McGuire of the FAA William J. Hughes Technical Center for their willingness to support the flight test program.

TABLE OF CONTENTS

LIST OF FIGURES

LIST OF ACRONYMS

ADS	Air data system
AoA	Angle(s) of attack
AR	Aspect ratio
CFD	Computation fluid dynamics
COTS	Commercial off-the-shelf
CPT	Control position transducers
DAS	Data acquisition system(s)
DFRDAS	David F. Rogers Data Acquisition System
EAS	Equivalent airspeed
ERAUDAS	Embry-Riddle Aeronautical University Data Acquisition System
FEA	Finite element analysis
FRL	Fuselage reference line
FTE	Flight test engineers
GA	General aviation
GAJSC	General Aviation Joint Steering Committee
GPS	Global Position System
IMU	Inertial measurement unit
KEAS	Knots equivalent airspeed
LOC	Loss of control
OAT	Outside air temperature
POH	Pilot's Operating Handbook
PPT	Precision static pressure transducer
TAS	True airspeed(s)

EXECUTIVE SUMMARY

The rate of general aviation (GA) accidents and fatalities is the highest of all aviation categories and has been nearly constant for the past decade. According to the National Transportation Safety Board, in 2010, GA accidents accounted for 96% of all aviation accidents, 97% of fatal aviation accidents, and 96% of all fatalities for U.S. civil aviation. However, GA accounted for 51% of the estimated total flight time of all U.S. civil aviation in 2010.

The FAA identified the top three causes of fatal GA accidents to be: 1) loss of control (LOC) in flight, 2) controlled flight into terrain, and 3) system or component failure/power plant. Additionally, the General Aviation Joint Steering Committee (GAJSC) recently published its final report on LOC, approach, and landing. The GAJSC LOC working group recommended angle of attack (AoA) systems as one of its top safety enhancements for GA aircraft. Current differential pressure AoA systems for light GA aircraft concentrate on the slow flight/stall regime. Typically, outside of this flight regime, these AoA systems are inaccurate. Therefore, they are not usable for critical flight regimes other than the stall region.

This study examined such systems. It was found that using unnormalized differential pressure (P_{fwd}-P_{45}) does not provide adequate accuracy throughout the aircraft's AoA range. Using unnormalized differential pressure (P_{fwd}-P_{45}) does not yield accurate AoA data throughout the aircraft's normal operating envelope. The calibration curve is nonlinear. For a limited range of high AoA near stall, a linear fit to the data near stall provides adequate accuracy. However, accuracy at low AoA, such as that required by cruise, is poor. Therefore, systems using unnormalized differential pressure—similar to that tested, which use a linear calibration—are basically stall warning devices.

Four alternate techniques were flight tested using the two pressure ports designated as P_{fwd} and P_{45} on the probe used with the commercial off-the-shelf (COTS) AoA data acquisition system (DAS). The flight test configurations were: the ratio of P_{fwd}/P_{45}; (P_{fwd}-P_{45})/P_{45}, which is just (P_{fwd}/P_{45})-1; (P_{fwd}-P_{45})/q; and (P_{fwd}-P_{45}). Only the ratio of P_{fwd}/P_{45} provided an accurate AoA throughout the aircraft's normal operating environment, including into and recovery from the stall region. The calibration curve based on the ratio of P_{fwd}/P_{45} was studied and determined to be linear throughout the aircraft's AoA provided that the probe was located on the wing's lower surface between an estimated 25% and 60% of the local wing chord.

The resulting calibration curve was linear because of the smooth laminar flow on the lower wing surface including when the upper wing surface was partially or fully separated. Normalizing (P_{fwd}-P_{45})/q (i.e., normalizing differential pressure with dynamic pressure) also produced a linear calibration curve, provided that the aircraft's true freestream dynamic pressure was used. Similar results may be expected for other differential pressure systems.

A low-cost ($100/table A-1 of appendix A) differential, pressure-based COTS AoA DAS was designed, successfully reduced to practice, wind tunnel tested, and flight tested. The accuracy of the COTS differential pressure AoA system was determined to be ¼ to ½ of a degree. The repeatability of the data from the COTS system was excellent. Differential pressure AoA systems are dynamic pressure-dependent. A physics-based determination of AoA was successful, provided

that a reasonably accurate aircraft lift curve was determined. Calculation of the lift curve slope was within 0.01 degrees of the value determined by the flight test, using an alpha/beta probe.

1. INTRODUCTION

Accurate angle of attack (AoA) information is important for safe and efficient operation throughout the aircraft's flight envelope. Accurate knowledge of AoA in the low speed/high AoA regime is important to prevent the typical low-altitude base to final stall/spin, approach, and departure/go-around accident. In most cases, such a stall or stall/spin is unrecoverable. Current differential pressure AoA systems for light GA aircraft concentrate on this flight regime. Typically, outside of this flight regime, these AoA systems are inaccurate. Therefore, they are unusable for critical flight regimes other than the stall region.

At AoA between the AoA for minimum power required (maximum endurance) and stall, the aircraft is operating on the backside of the power required curve. In this regime, the effect of power application is reversed (i.e., the pilot must add power to fly slower); this is counterintuitive. Furthermore, in this flight regime, the aircraft does not have speed stability. These characteristics frequently lead to inadvertent controlled flight into terrain. Providing accurate AoA information to the pilot that clearly depicts this flight regime is useful in preventing departure from controlled flight.

Lower than the AoA for minimum power required, the AoA for maximum lift-to-drag ratio corresponds to maximum range and maximum glide ratio for a piston engine propeller aircraft. This AoA does not change with density altitude, weight, load factor, etc. Therefore, in a fuel-critical or an engine-failure situation, it is crucial that the pilot have accurate access to this AoA.

With current fuel costs, the Carson Cruise AoA, which represents the most efficient way to fly fast with the least increase in fuel consumption, is of significant interest.

2. THE AIRCRAFT FUNDAMENTAL ANGLE OF ATTACK[1]

According to the researcher's findings, there is a fundamental AoA for an aircraft. The information presented in figure 1 shows curves of the power required to maintain level flight versus true airspeed (TAS) for various altitudes on a standard day. Clearly, the power required changes with altitude.

It is well known that, for a piston/propeller aircraft, a line drawn through the origin tangent to the power required curve yields the speed for maximum lift-to-drag ratio, as the dashed line in figure 1 shows. The speed for maximum lift-to-drag ratio is also the speed for maximum range and for best glide. The single dashed line touches each power-required curve for the various altitudes. The power required curve slides along the line for the maximum lift-to-drag ratio with increasing altitude. Therefore, the TAS increases with increasing altitude.

However, the angle between the line for maximum lift-to-drag ratio remains the same (i.e., there is only one dashed line for all altitudes). The angle between the dashed line and the abscissa

[1] The following is based on a paper, "Fundamental Angle of Attack," by David F. Rogers, which is available online at http://www.nar-associates.com/technical-flying/angle_of_attack/FundamentalAoA_wide_screen.pdf.

(*x*-axis) is directly related to the absolute AoA for maximum lift-to-drag ratio. Therefore, the AoA for the maximum lift-to-drag ratio does not depend on density altitude.

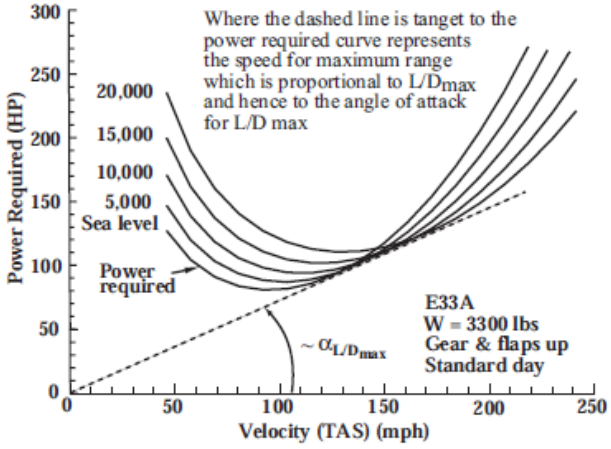

Figure 1. Altitude effect on power required

2.1 NONDIMENSIONALIZATION

Figure 1 suggests nondimensionalizing the velocity with the velocity for maximum lift-to-drag ratio, $V_{L/Dmax}$, and the power required with that required for the maximum lift-to-drag ratio, $PR_{L/Dmax}$ [1].

The result is shown in figure 2. Not only does nondimensionalization collapse the effect of density altitude, σ (sigma), on the power required, it also collapses the effects of weight, W; load factor, *n*; and aircraft configuration (i.e., *e*, the Oswald aircraft efficiency factor, and f, the aircraft equivalent parasite drag area) into a single curve. The formulas for the velocity and power required for maximum lift-to-drag ratio are given in figure 2, where *b* is the aircraft wing span. The results in figure 2 allow for the determination of the power required for any altitude, weight, load factor, and configuration for any velocity.

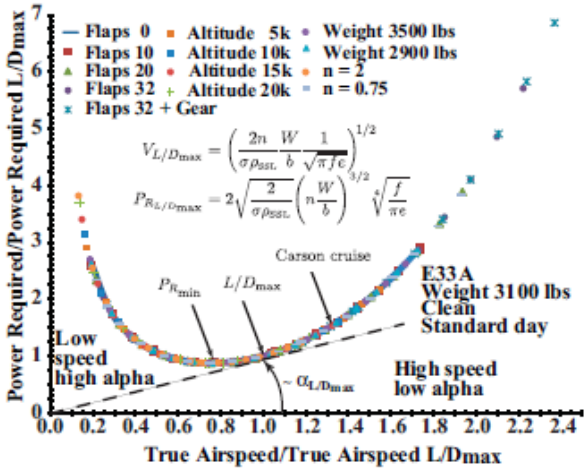

Figure 2. Nondimensional power required—multiple effects

2.2 RELATION BETWEEN ANGLE OF ATTACK AND VELOCITY

Discussion has previously been couched in terms of velocity. Absolute value of AoA will now be examined. The absolute AoA varies inversely with the square of the velocity—that is, from:

$$C_L = a\alpha = \frac{2n}{\sigma\rho_{SSL}}\frac{W}{S}\frac{1}{V^2} \quad \text{we have} \quad \alpha = \frac{1}{a}\frac{2n}{\sigma\rho_{SSL}}\frac{W}{S}\frac{1}{V^2} \propto \frac{1}{(V^2)} \tag{1}$$

where C_L is the lift coefficient, a is the linear lift curve slope, ρ_{SSL} is the density at sea level on a standard day, and S is the wing area.

Figure 3 illustrates the relationship between absolute AoA and velocity nondimensionalized with AoA and velocity for maximum lift-to-drag ratio, respectively. The result is a parabolic (second degree or quadratic) curve. Notice that the AoA decreases significantly with increasing velocity. Conversely, the AoA increases significantly with decreasing velocity. Again, the formulas for absolute AoA and power required for maximum lift-to-drag ratio are given in figure 3. Notice that, again, the results for all the various configurations collapse into a single curve.

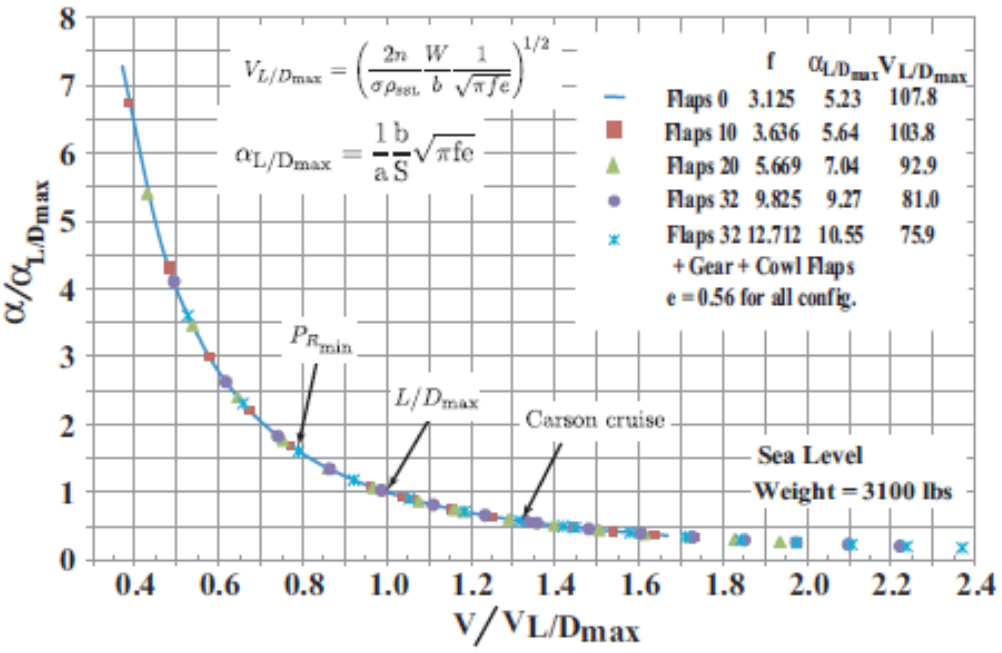

Figure 3. Relationship between nondimensional velocity and nondimensional angle of attack

2.3 FUNDAMENTAL ANGLE OF ATTACK — $\alpha_{L/DMAX}$

Figure 3 shows that the absolute AoA for maximum lift-to-drag ratio is a fundamental aircraft AoA. Closer examination of the absolute AoA shows that it is independent of density altitude and aircraft weight. In fact, it depends only on aircraft design parameters (i.e., characteristics that are built into the aircraft). Specifically:

$$\alpha_{L/Dmax} = \frac{1}{a}\frac{b}{S}\sqrt{\pi fe} \tag{2}$$

which does not depend on weight, W; load factor, *n*; or density altitude, *σ*. The absolute AoA for L/D_{max} depends only on aircraft design parameters: lift curve slope, *a*; wing span, *b*; wing area, *S*; parasite drag, *f*; and the Oswald aircraft efficiency factor, *e*. Although the parasite drag, *f*, and the Oswald efficiency factor, *e*, can be changed in flight (e.g., by extending gear/ flaps or opening cowl flaps), they are still aircraft design parameters.

In addition, there are two other AoA that are simple numerical multiples of the absolute AoA for maximum lift-to-drag ratio. They are the absolute AoA for minimum power required (maximum endurance) and the absolute AoA for Carson Cruise. Specifically, the corresponding AoA for P_{Rmin} and Carson Cruise are:

$$\alpha_{P_{R_{min}}} = \sqrt{3}\alpha_{L/D_{max}} = 1.73\alpha_{L/D_{max}} \quad \text{and} \quad \alpha_{CC} = \frac{1}{\sqrt{3}}\alpha_{L/D_{max}} = 0.58\alpha_{L/D_{max}} \tag{3}$$

Therefore, the absolute AoA for minimum power required is simply $1.73\alpha_{L/Dmax}$, whereas the absolute AoA for Carson Cruise is $0.58\alpha_{L/Dmax}$, as shown in figure 3. These AoA are also independent of density altitude, weight, and load factor.

Recalling that the velocity for $V_{L/Dmax}$ is:

$$V_{L/D_{max}} = \left(\frac{2n}{\sigma\rho_{SSL}}\frac{W}{b}\frac{1}{\sqrt{\pi fe}}\right)^{1/2} \tag{4}$$

the velocities for V_{PRmin} and V_{CC} are also multiples of the $V_{L/Dmax}$. Specifically:

$$V_{P_{R_{min}}} = \frac{1}{\sqrt[4]{3}}V_{L/D_{max}} = 0.76V_{L/D_{max}} \text{ and } V_{CC} = \frac{1}{\sqrt[4]{3}}V_{L/D_{max}} = 1.32V_{L/D_{max}} \tag{5}$$

However, the velocity (TAS) for $V_{L/Dmax}$ does depend on weight, density, altitude, and load factor, as shown in the equations above and in figure 3. Therefore, the velocity for minimum power required and Carson Cruise also depends on weight, density, altitude, and load factor.

2.4 POWER REQUIRED AND ANGLE OF ATTACK

Recalling the inverse square relationship between AoA and velocity allows recasting the nondimensional power required in terms of the AoA. However, it is convenient to recast it in terms of the nondimensional square root of the absolute AoA over the AoA, as shown in figure 4. Here, we see that figure 4 appears similar to figure 2. Specifically, the line through the origin tangent to the curve is again related to the absolute AoA for the maximum lift-to-drag ratio. That is why it was recast in terms of the square root of the absolute AoA for the maximum lift-to-drag ratio divided by the absolute AoA.

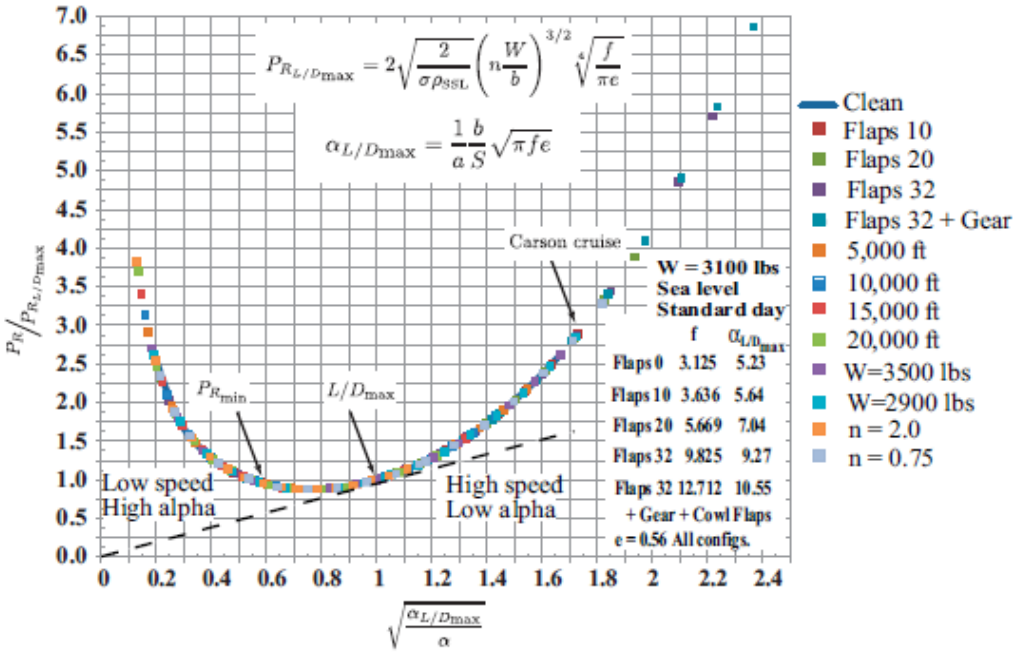

Figure 4. Relationship between nondimensional power required and nondimensional AoA

2.5 WHY IS FLYING ANGLE OF ATTACK IMPORTANT?

Why is it important to understand that $V_{L/Dmax}$ varies with weight, but $\alpha_{L/Dmax}$ does not? Look at the speed for L/D_{max} (best range speed) for a typical 3300 lb. single-engine retractable-gear aircraft. With a single pilot and some equipment aboard, that aircraft might typically depart with full fuel at 2900 lbs. The pilot operating handbook gives the equivalent airspeed (EAS) in knots equivalent airspeed (KEAS) at full gross weight as 105 KEAS. That aircraft might carry 74 gallons of useable fuel.

The KEAS for $V_{L/Dmax}$ decreases with decreasing weight as the square root of the weight ratio. For full fuel at 2900 lb., the EAS for $V_{L/Dmax}$ is approximately 98 KEAS. At half fuel, it is approximately 95 KEAS. With empty tanks, it is approximately 90 KEAS. However, the AoA, $\alpha_{L/Dmax}$, remains constant. Flying AoA might make the mission possible whether it is to the mission destination or, in an emergency, a glide to an on-airport landing rather than an off-airport landing. Furthermore, no calculations are required; the AoA must simply be flown. Similar arguments apply to Carson Cruise and minimum power required (figure 2).

3. WIND TUNNEL TESTS

Rogers [2] conducted wind tunnel tests of a typical differential pressure AoA probe. The probe is shown mounted in the wind tunnel in figure 5. Typically, in flight, the probe is mounted on the bottom of the wing of a single-engine aircraft or on the underside of the nose of a twin-engine aircraft. The probe contains two pressure ports, each 0.1 inches in diameter. One pressure port, called P_{fwd} in figure 6, is nominally aligned with the airstream direction under the wing. In

high-speed cruise flight, P_{fwd} nominally measures total pressure. The second pressure port, called P_{45} in figure 6, is located on the flat 45° surface.

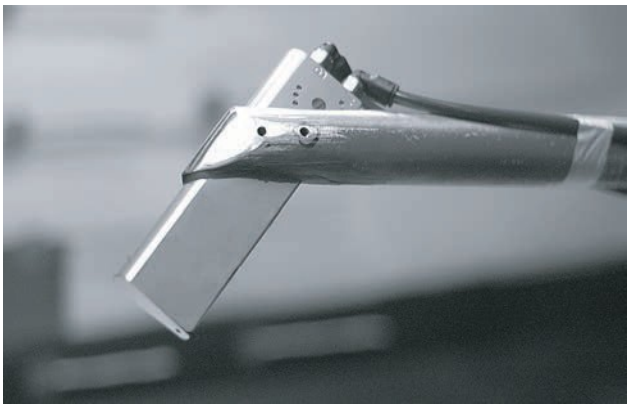

Figure 5. Probe mounted in the wind tunnel

Figure 6. Probe pressure port locations

The differential pressure P_{fwd}-P_{45} is related to AoA. Conceptually, it is similar to the classical spherical or cylindrical-based differential pressure AoA probe [3, 4, and references therein].

Tests were conducted for a range of AoA (pitch), yaw, and roll for various dynamic pressures. The pressures at P_{fwd} and P_{45} were directly measured using an inclined alcohol manometer. As expected, both pressures varied linearly with AoA. However, P_{fwd} P_{45}, and the differential pressure P_{fwd}-P_{45} exhibited a dynamic pressure effect, as shown in figure 7. Normalizing the differential pressure P_{fwd}-P_{45} with the dynamic pressure collapsed the data to a single linear relationship, as shown in figure 8. Therefore, the effects of speed and density altitude are removed when deriving AoA from differential pressure.

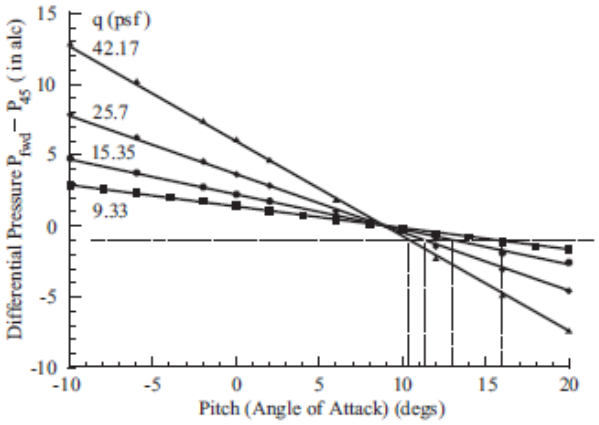

Figure 7. P_{fwd}-P_{45} as a function of AoA

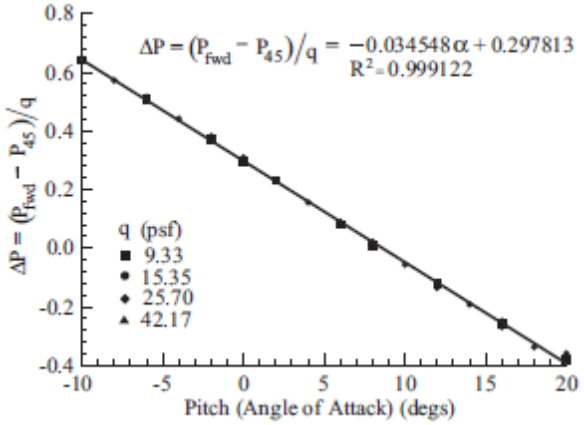

Figure 8. P_{fwd}-P_{45} normalized with dynamic pressure

3.1 THE CALIBRATION EFFECT

From the definition for the lift coefficient and the equation for the normalized differential pressure shown in figure 8, along with appropriate aircraft parameters, the variation of differential pressure as a function of AoA can be obtained specifically from:

$$C_L = a\alpha = \frac{2W}{\rho_{SSL}(EAS)^2 S} \quad \text{we have} \quad \alpha = \frac{1}{a}\frac{2W}{\rho_{SSL}(EAS)^2 S} \tag{6}$$

where EAS is the EAS and ρ_{SSL} is the density at sea level on a standard day. In terms of the EAS, the dynamic pressure is given by:

$$q = 1/2\, \rho_{SSL}(EAS)^2 \tag{7}$$

Using the equation for the normalized differential pressure from figure 8, the differential pressure as a function of AoA—called the flight line—is obtained, as shown in figure 9. As expected from the discussion above, the flight line is a parabolic function of the AoA.

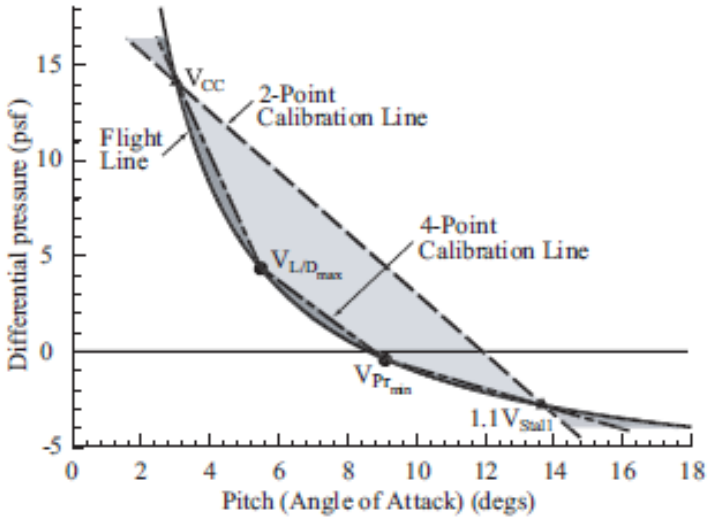

Figure 9. Flight line and the effect of two-point and four-point linear calibration

3.2 CALIBRATION TECHNIQUES

Simple differential, pressure-based AoA probes typically use a 2-point calibration with linear interpolation between the two calibration points. The dashed line in figure 9, labeled "2-Point Calibration Line," shows the resulting calibration line when the Carson Cruise speed and a speed 10% above stall speed are used as the calibration points. The light-gray shaded area illustrates the error in the displayed AoA that results from this technique. The error can be significant.

Figure 9 suggests using a multiple-point linear chordwise approximation to increase the accuracy of the calibration curve. The line labeled "4-Point Calibration Line," using the speed for Carson Cruise, the speed for maximum lift-to-drag ratio, the speed for minimum power required, and a speed 10% above stall, speeds results. The dark-gray shaded area illustrates the considerably smaller error in the displayed AoA resulting from this technique. However, neither of these linear chordwise calibration techniques account for the dynamic pressure effect.

3.3 ALTERNATE NORMALIZATION TECHNIQUES

The calibration techniques shown in figure 9 do not account for the dynamic pressure effects shown in figure 7. Because the FAA does not consider an AoA system on a GA aircraft that accesses the aircraft pitot-static system [5] a minor alteration, an alternate method of normalizing the differential pressure independent of the aircraft pitot-static system, as suggested by Rogers [2], is shown in figure 10. Here, the pressure P_{fwd} is normalized using the pressure from the 45° surface, P_{45}. Figure 10 clearly shows that the results for all four dynamic pressures tested in the wind tunnel collapse into a single parabolic curve. Similar results, not shown, are obtained by normalizing the

differential pressure P_{fwd}-P_{45} by P_{45}. This technique of normalizing was used throughout the development of the David F. Rogers Data Acquisition System (DFRDAS) for the flight-test portion of this study. Figure 11 shows AoA as a function of P_{fwd}/P_{45} for the wind tunnel tests.

In a wind tunnel study, the independent variables are often pitch angle (AoA), yaw angle, and roll angle along with dynamic pressure. In a wind tunnel, any pitch angle, yaw angle, or roll angle can be obtained for any dynamic pressure within the capability of the tunnel. These variables are, therefore, frequently used as the independent variable when presenting results. However, in steady flight, AoA, sideslip, and roll are linked to dynamic pressure simply because AoA—and, to a lesser extent, sideslip and roll (bank angle)—control speed. Consequently, as will be covered in this report later, careful selection of the independent variable is key to obtaining appropriate results.

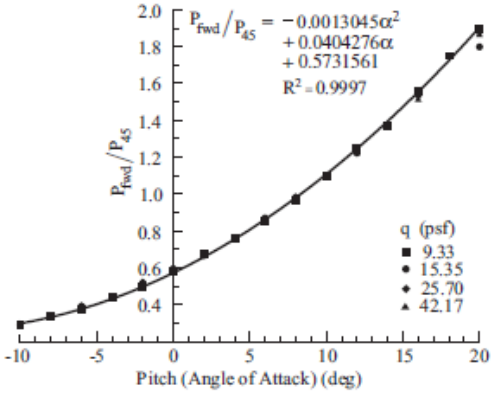

Figure 10. An alternate method of normalizing the pressure

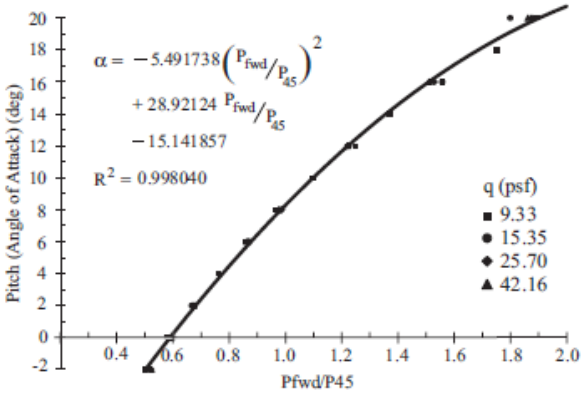

Figure 11. AoA as a function of P_{fwd}/P_{45}

4. DESIGN OF THE DATA ACQUISITION SYSTEM

The fundamental considerations for the design of the data acquisition system (DAS) were accuracy and low cost. These considerations, especially cost, dictated a commercial-off-the-shelf (COTS) approach to make the system available to the largest number of light GA aircraft owners.

4.1 ACCURACY

Accuracy is driven by the relatively small range of absolute AoA in which a typical light GA aircraft operates. The absolute AoA range from cruise to stall is typically 20°–22° or less. Furthermore, the dividing lines between critical conditions are on the order of 1–2°. For example, the difference between a stalled and unstalled wing is on the order of 1°. Similarly, to receive the benefits of Carson Cruise or to operate at L/D_{max}—the speed for best range—the AoA should be held within ±1° (i.e., within a 2° band). These requirements dictate an accuracy of ±1/4° to ±1/2°.

4.2 PRESSURE RANGE

One way to establish the required pressure range is to recall that on a standard day at sea level, the pressure exerted by a 20″ column of water corresponds to a dynamic pressure resulting from a speed of 200 mph. A pressure of 20″ of water equates to approximately 0.72 psi. The dynamic pressure corresponding to a speed of 200 knots equates to a pressure just under 1.0 psi (i.e., 0.94 psi). Similarly, in the low-speed range at and near stall, the dynamic pressure at 50 mph equates to approximately 11/4″ of water, or 0.045 psi. These are very small pressures. Furthermore, these small numbers have implications for the required accuracy of the pressure sensors.

Referring to the equation in figure 8, a 1º change in AoA (α) corresponds to approximately $\Delta P/q = 0.26$. Near stall, the dynamic pressure is approximately 0.045 psi. Therefore, the differential pressure is approximately 0.012 psi. If the pressure sensor, full scale, is 1.0 psi, and ±1/4° of AoA is the required accuracy, then a full-scale accuracy of 1/4% is required.

4.3 REFERENCE PRESSURE

All pressure measurements are differential. A so-called absolute pressure gauge is simply a differential pressure gauge with a built-in reference pressure. An example is the Bourdon tube in an altimeter. The original wind tunnel tests used the local atmospheric pressure for the reference pressure. The question becomes: What should be used as a reference pressure for the digital DAS while in flight? This becomes particularly important considering the range of "local" atmospheric pressure and temperature as the aircraft climbs and descends.

4.4 PRESSURE SENSORS

The Measurement Specialties MS4525DO differential pressure sensor was chosen because of commercial availability and its low cost ($21/table A-1 of appendix A). Specifically the MS4525DO-DS-5-A-I-001-D-P was used [7]. This unit, shown in figure 12, is a small, ceramic-based, personal-computer, board-mounted, low-power pressure transducer with a 14-bit digital temperature-compensated (11-bit) output. Full-scale output is 1.0 psi, with an accuracy of ±1/4% of full-scale. The 1/8″ barbed pressure ports mate securely with 3/32 ID tubing. The sensor is designed to operate at either 3.3 or 5.0 VDC. The sensor is compatible with either the I2C or SPI bus. Multiple I2C addresses are specified, although only one I2C address was available for the sensors used for the DAS.

Because of concerns with the reference pressure, an additional sensor was included in the DAS design. The Bosch BMP085 [6] was chosen because of commercial availability and cost. The BMP085, shown in figure 13, and its replacement (the BMP180), are high-precision, ultra-low-power, barometric pressure sensors. Their accuracy is of the order of 2.5 hPa, with low noise level down to 0.03 hPa, which is equivalent to an altitude change of approximately 8″. Conversion to local atmospheric pressure is straightforward. Digital temperature measurement is also available from the sensor. The BMP085 is about the size of a quarter. The BMP085 and BMP180 are also compatible with the I2C bus.

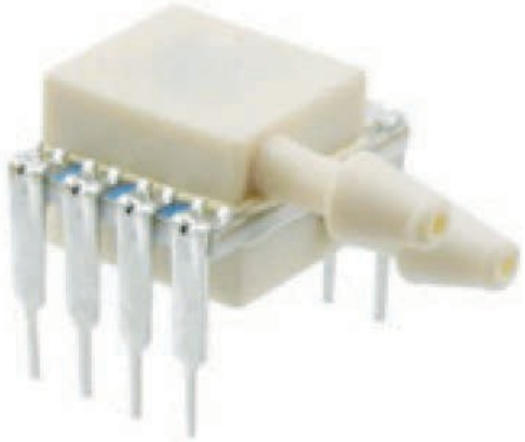

Figure 12. MS4525 differential pressure sensor

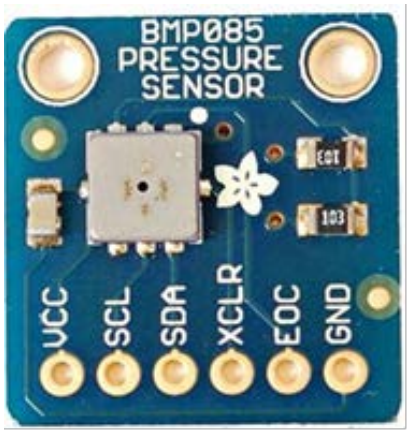

Figure 13. Bosch BMP085 altitude/pressure absolute pressure sensor

4.5 DEVELOPMENT SYSTEM

The Arduino UNO was chosen as the microcontroller development system because of cost, simplicity, and availability of hardware and software support systems.

The Arduino UNO, shown in figure 14, is a microcontroller board based on the 16-bit ATmega328 16U2. The ATmega328 has 32 kB of flash memory, of which 0.5 kB are used by the boot loader, and 2 kB of SRAM memory. The board has 14 digital input/output pins, six analog inputs, a USB connection, a power jack, an ICSP header, a reset button, and a 16 MHz ceramic resonator. Bidirectional communication between the UNO and a standard personal computer is facilitated via a USB cable. The UNO can be powered from the development computer via a USB cable, a separate AC-to-DC adapter, or a separate battery. Operating voltage is 5 VDC.

Figure 14. Arduino UNO R3 development microcontroller system

Software support is available for Windows®, macOS™, and Linux®. The open-source Arduino Software Integrated Development Environment allows writing code on the host computer and uploading the correctly compiled code to the board. The software environment is written in Java™ and other open-source software. A serial monitor is included in the Arduino software, which allows simple textual data to be sent to and from the Arduino board. When data are transmitted over the USB connection to the computer, RX (receive) and TX (transmit) light-emitting diodes on the board flash.

A SoftwareSerial library allows for serial communication on any of the UNO's digital pins. A Wire library is included in the software to simplify communication with the I2C bus. A specific library is available for SPI bus communication. The ATmega328 on the Arduino UNO comes pre-burned with a bootloader that allows uploading code without using a separate hardware programmer. The UNO PC board is 2.7″ long and 2.1″ wide. The USB connector and power jack extend beyond the board edge. Four screw holes are provided for mounting the board.

4.6 BASIC DESIGN OF THE DFRDAS

The COTS DAS consists of the Arduino UNO, two Measurement Specialties MS4525 0–1 psi differential pressure sensors, a Bosch BMP085 altitude/pressure sensor, and various resistors and capacitors, as detailed in the block diagram in appendix A. The pressure sensors, Bosch BMP085 (or BMP180), and the small parts are mounted on a Proto shield that attaches to the UNO. The pinouts are also given in the block diagram in appendix A.

4.7 SOFTWARE DESCRIPTION

A block diagram of the DFRDAS software, along with a full listing of the software, is given in appendix A. The program begins with a declaration of the global variables followed by setting up the pins, allowing communication with the hardware. The main loop first gets the atmospheric pressure from the Bosch BMP085 or BMP180. Because only MS4525 sensors with a common address were available, it was necessary to multiplex—accessing the two MS4525 pressure sensors for P_{fwd} and P_{45}. The P_{fwd} and P_{45} pressure values are acquired as raw counts in the range of 0–16,383. These values are corrected by subtracting the "noload" values corresponding to 0

differential pressure. The ratio P_{fwd}/P_{45} is then calculated using the noload-corrected P_{fwd} and P_{45} values. The AoA, α, is then determined from the calibration equation. Finally, the result is either printed or displayed, as required.

4.8 WIND TUNNEL TESTING OF THE DFRDAS BREADBOARD

To ensure that the breadboard DAS, shown in figure 15, worked correctly and provided appropriate accuracy, a wind tunnel test was conducted. The AoA probe was set up in the wind tunnel exactly as reported by Rogers [2], with the exception that the P_{fwd} and P_{45} pressure lines were connected to the breadboard DAS. Fifty samples were simultaneously collected by the breadboard DAS, whereas the inclined alcohol manometer was manually read. The AoA probe was pitched from−6◦–18◦ in 4-degree increments for dynamic pressures of 2.2″, 5.1″, 8.9″, 15.4″, and 19.9″ of alcohol. The samples acquired by the breadboard DAS were corrected for the noload condition and then averaged to yield P_{fwd}/P_{45}. The local barometric pressure was used as the reference pressure for both the inclined alcohol manometer and MS4525 pressure sensors in the breadboard DAS. The results for the alcohol DAS and the breadboard DAS are shown in figure 16. The accuracy of the pitch attitude of the wind tunnel balance is 0.1°. Clearly, the breadboard DAS is of equal or better accuracy under the flow conditions present in the wind tunnel.

In the static environment of the wind tunnel room, using the local room atmospheric pressure as the reference pressure for the DAS was clearly satisfactory. However, considering the large variation of atmospheric pressure with altitude, the question remained: Would using the local atmospheric pressure as the reference pressure work for the MS4525 sensors?

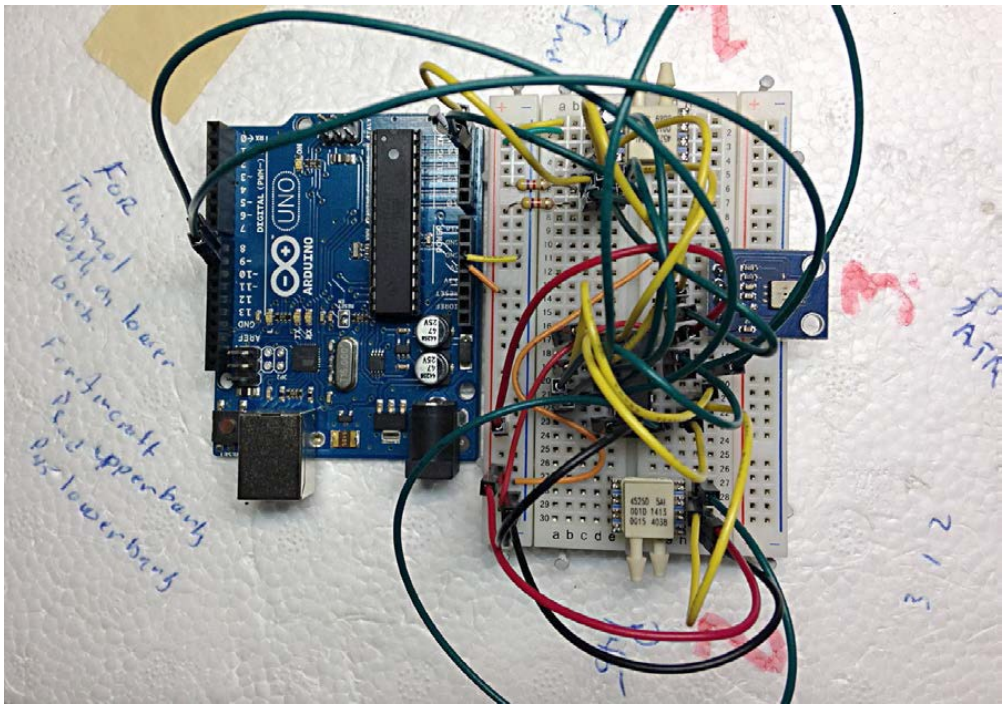

Figure 15. DFRDAS breadboard as used for wind tunnel verification tests

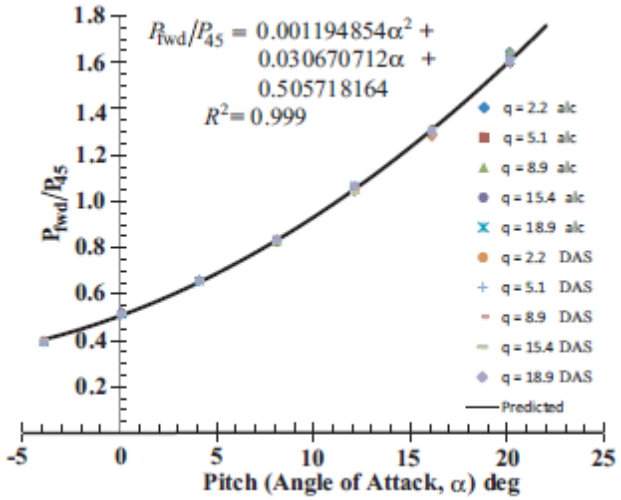

Figure 16. Comparison of wind tunnel result for the breadboard DAS and the results read from the inclined manometer

4.9 NOLOAD ALTITUDE TEST

The breadboard DAS was tested for variation in the noload (bias) values at altitudes from near sea level (15') to 6000' in 1000' increments. While in steady level flight, a sample of 500 noload values was taken for both the P_{fwd} and P_{45} sensors. The standard deviation for the 500 noload values was on the order of 10 counts of 16,383 possible counts. The maximum observed change in the noload value was 22 counts. For P_{fwd}, the noload count decreased slightly with increasing altitude, whereas for P_{45}, the noload count increased slightly for increasing altitude. These changes are small and attributable to individual sensor calibration by the manufacturer and, possibly, temperature changes with altitude. The maximum observed change represents approximately 0.1% of full-scale for the sensor.

5. ROAD TESTS

The wind tunnel used for the AoA probe tests is a straight-through design (Eiffel) tunnel that uses the surrounding room as the plenum; the test section is sealed. Therefore, both the P_{fwd} and P_{45} pressures are below atmospheric pressure. Consequently, the lower (No. 1) barb on the MS4525 is used to measure pressure. The upper barb is left open to the local atmospheric pressure.

However, in flight, P_{fwd} at typical flight attitudes is nominally the total pressure (i.e., the dynamic pressure plus the static pressure). In flight, the static pressure is nominally the local atmospheric pressure. Thus, P_{fwd} is normally greater than the local atmospheric pressure, and therefore positive, and the lower (no. 1) barb on the MS4525 is used to measure P_{fwd}, whereas the upper (no. 2) barb is used for the reference pressure.

If the local atmospheric pressure is used as the reference pressure for P_{45}, the result is not as clear. If the pressure at P_{45} is less than the local atmospheric pressure, then, when corrected for the noload value, a negative value of P_{45} results. If that is the case, solving the quadratic calibration

equation presented in figure 16 is problematic, especially at the low dynamic pressures associated with speeds near stall.

Consequently, a rig was developed which, mounted on a truck, allowed testing the breadboard DAS at low speeds. The rig consisted of a PVC pipe attached to a pair of roof racks on the truck cab. The pipe projected forward over the truck hood. The probe was mounted to the forward end of the PVC pipe.

Road tests were conducted at 25 and 60 mph for all four possible barb connections. The results suggested that both P_{fwd} and P_{45} are positive for the anticipated probe pitch angles. Therefore, both P_{fwd} and P_{45} pressure sensors were connected to the lower No. 1 position, as shown in the MS4525 data sheet [7] for the flight tests. In addition, the turbulence on the highway was clearly shown in the acquired data, which suggested that the DFRDAS was both fast enough and sensitive enough.

6. PROOF OF CONCEPT FLIGHT TEST

An initial proof of concept flight test was conducted at Bay Bridge Airport (W29) on January 21 and 22, 2015. The purpose of the flight tests was to confirm that:

- The DFRDAS mechanically and electrically worked in flight.
- The DFRDAS had an adequate data acquisition sample rate in flight.
- The local atmospheric pressure, as the reference pressure when determining P_{fwd}/P_{45}, correctly normalized the pressures.
- The P_{fwd}/P_{45} curves for different altitudes collapsed into a single curve.

7. THE AIRCRAFT

The aircraft used was a Cessna 182Q. The aircraft was not equipped with an AoA/angle of sideslip (α/β) boom for these flights. A standard GA differential pressure AoA probe, as used in the wind tunnel tests, was mounted on the left wing in an inspection port centered approximately 13″ outboard of the wing strut attachment. The center of the probe inspection port was approximately 4″ aft of the leading edge, which placed P_{fwd} approximately at the leading edge.

Mounting the differential pressure AoA probe at the leading edge is outside of the manufacturer's recommendation. Mounted this far forward, the probe is in the upwash field ahead of the wing. It may also be in the critical area where the surface pressure on the wing changes from positive to negative with respect to the local atmospheric pressure [8] as the aircraft's AoA changes.

8. THE JANUARY 21 AND 22, 2015 FLIGHTS

Two flights were conducted—one at 2000' pressure altitude and the second at 6000' pressure altitude—to confirm that the results were independent of altitude. A single DFRDAS (DFRDAS-1) DAS, connected to the differential AoA probe mounted on the left wing, was used. The calibration curve from the wind tunnel test results shown in figure 16 was coded into the DFRDAS-1 software. Raw counts from both MS4525 sensors and the BMP85 sensor were recorded. Outside air temperature (OAT) was manually recorded from the Aspen Avionics Evolution 1000.

The 4-leg Global Position System (GPS) horseshoe heading technique [9, 10, 2] was used to acquire multiple data points for various indicated airspeeds. Indicated airspeed, altitude, manifold pressure, and engine RPM were manually recorded and maintained constant for each of the legs of the 4-leg GPS box pattern. Using the onboard fuel computer, the fuel remaining was manually recorded for each leg of the 4-leg GPS pattern.

TAS was determined from the GPS ground speed on four headings 90° apart. Aircraft weight for each of the four GPS legs was determined by subtracting the fuel used from the initial aircraft weight.

The flight test points were chosen based on the best glide velocity from the Pilot's Operating Handbook [11] at full gross weight (i.e., $V_{L/Dmax}$ = 71 kts [$\alpha_{L/Dmax} \approx 12^{o}$]). An additional test point

was Carson Cruise (i.e., V_{CC} = 1.32 $V_{L/Dmax}$ ≈ 95 kts [α_{CC} ≈ 7º]). Additional points fleshed out the data at intermediate, slower, and faster speeds.

8.1 PHYSICS-BASED DETERMINATION OF ABSOLUTE AOA

From the basic definition of the lift coefficient:

$$C_L = a\alpha = n\frac{W}{S}\frac{1}{(1/2\rho V^2)} = n\frac{W}{S}\frac{1}{q} \quad \text{which yields} \quad \alpha = 2\frac{1}{a}\frac{n}{\rho}\frac{W}{S}\frac{1}{V^2} \propto \frac{1}{(V^2)} \tag{8}$$

where C_L is the lift coefficient, a is the lift curve slope, α is the absolute AoA, W is the weight of the aircraft, n is the load factor, ρ (rho) is the air density, V is the TAS, and S is the wing area. The Cessna 182Q wing area is S = 174 ft^2 with a span b = 35' 10″, which yields an aspect ratio (AR) = 7.38.

Here, $q = \frac{1}{2}\rho V^2$ is the dynamic pressure (i.e., the pressure resulting from the motion of the aircraft through the air). It is sometimes called ram (impact) pressure. Dynamic pressure is a force per unit area.

Noting that the TAS is known from the 4-leg GPS horseshoe heading calculations, for any individual box pattern (TAS data point) flown at constant altitude, constant indicated airspeed, known weight, and OAT, the absolute AoA can be determined if the aircraft lift curve slope, a, is known.

The linear portion of the aircraft lift curve slope can be estimated from [1 or 12]:

$$a = \frac{a_o}{1+\frac{a_o}{\pi AR}} = 0.081/deg \tag{9}$$

where a_o is the lift curve slope of the wing airfoil section and AR is the wing aspect ratio, taper ratio, and AR. The Cessna 182Q uses an NACA 2412 airfoil section, which has a sectional lift curve slope of 0.101/deg. [13] and yields a = 0.081/deg., as indicated in equation 9. The AR and taper ratio reduce this value somewhat. Lifting surface theory for an AR, AR= 7.38, gives a value of 0.080/deg. [14]. Therefore, a lift curve slope of a = 0.080/deg. is used for the linear portion of the CL versus α curve.

8.2 THE RESULTS OF THE JANUARY 21 AND 22, 2015 FLIGHT TESTS

The results for the January 21 and 22, 2015 proof-of-concept flight tests are shown in figure 17. Clearly, the results for both the 2000' and 6000' pressure altitude flight collapse into a single curve. Therefore, the use of the local atmospheric pressure as the reference pressure is acceptable.

The curve in figure 17 represents a second order polynomial (parabolic) fit to both the 2000' and 6000' flight test data. The AoA in figure 17 is the physics-based absolute AoA estimate discussed above. The equation in figure 17 represents the calibration curve for this AoA probe location. The AoA represented by the calibration curve is within the required DAS accuracy of ±1/4° to ± 1/2°.

The highest AoA shown in figure 17 is significantly lower than the stall AoA. If the calibration curve is continued closer to the stall AoA, it begins to curve upward. This upward curvature can potentially result in difficulty in solving the parabolic calibration curve for absolute AoA given the measured P_{fwd}/P_{45}. The measured sample rate for the DFRDAS-1, written to the file on the laptop computer, was better than 17 samples/sec.

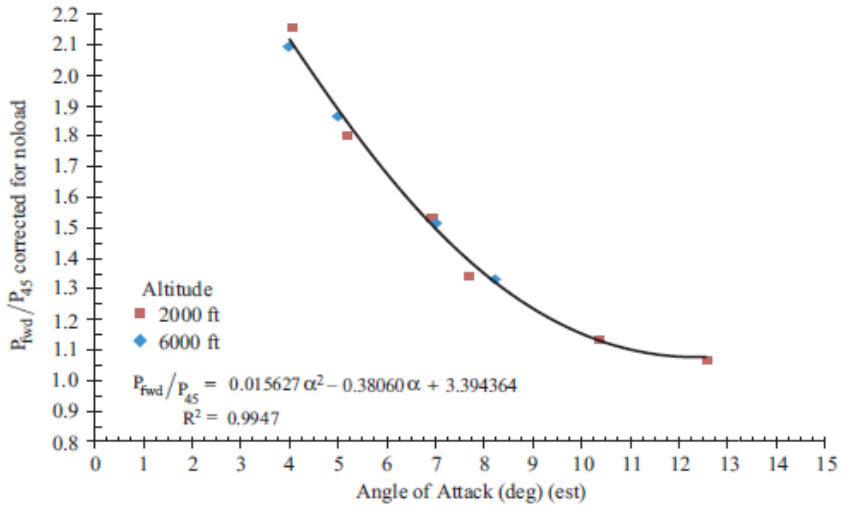

Figure 17. Combined results for the January 21 and 22, 2015 flight tests

9. AIR DATA PROBE AND ALPHA/BETA BOOM

Subsequent to the January 21 and 22, 2015 flight tests, an air data probe was mounted on the aircraft. The air data probe consists of alpha and beta vanes and a swivel-head pitot-static system. The probe extends approximately one mean aerodynamic chord length (≈ 60 1/2 inches) in front of the wing leading edge, as shown in figures 18 and 19. Only the AoA and pitot-static system were used as a source for the current AoA study.

Figure 18. Alpha/beta probe mounted on the aircraft

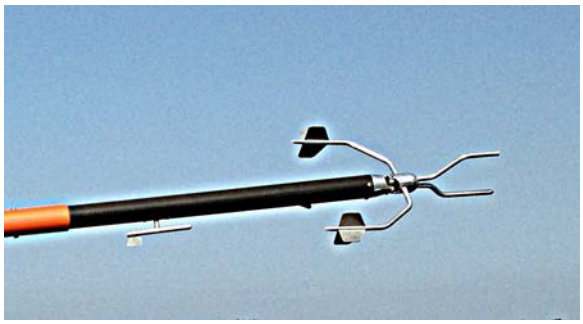

Figure 19. Alpha/beta probe head

The air data probe was installed on the right wing tip. The probe-supporting structure was integrated into the outboard rib. The supporting structure is constructed of 6061-T6 aluminum and carbon fiber. The probe was analyzed using loads in regulation Title 14 Code of Federal Regulations Part 23.337 [15] for utility category (4.4 G). An aerodynamic load, at V_D and 10º angle of sideslip, was superimposed and assumed as a worst-case condition. Static and dynamic structural analyses were conducted. These analyses included hand calculations and finite element analysis (FEA) [16] using two commercial software packages. An additional computation fluid dynamics (CFD) analysis [17] was also conducted in support of the structural analysis. Selected results, as well as representative part and installation drawings, are included in appendix B.

Ground structural testing represented the design 4.4 G case. Point loads (weights) were used along the length of the probe to simulate the calculated shear and bending moment diagrams [18]. The FEA analysis predicted a maximum deflection of 0.219″ at the tip of the probe. During ground testing, the maximum deflection was 0.288″, which represents a 31.5% error in the calculations. The test limit was set at 1 in deflection. As the boom was unloaded, the tip returned to its initial position. A post-test inspection included all brackets, fasteners, and rivets on the probe, supporting structure, and the aircraft's right wing. There were no signs of cracks, fatigue, or deformation in any of the inspected elements.

The aircraft DAS collects data from the inertial measurement system, GPS unit, total and static digital pressure transducers, and AoA and angle of sideslip control position transducers (CPT). All sensor signals were interpreted by a National Instruments CompactRIO (reconfigurable input/output) communications module in real time at 50 Hz. The CompactRIO simultaneously logs data in a raw format and outputs the data to the flight test engineers' (FTE's) laptop. The laptop serves as master control module for the Embry-Riddle Aeronautical University Data Acquisition System (ERAUDAS) and as a data processing and logging device. The OAT and fuel quantities were manually entered on the FTE laptop throughout the flight. The laptop saves the processed data into a comma-separated value file that is then reduced and interpreted post-flight.

Ground calibrations for the total and static digital pressure transducers and AoA and angle of sideslip CPT were performed prior to the first flight. All ground calibrations utilized the DAS and were performed "end to end." The AoA measured by the alpha/beta probe was calibrated with respect to the fuselage reference line (FRL). Details of the ground calibration setup and results are included in appendix B.

Prior to the first flight, a safety review board was convened. Configuration control requests, hazard and risk assessments, and flight test cards were reviewed and approved. A safety finding and flight permit were issued. Subsequent to the first flight, a second safety review board was convened. The aircraft was cleared for research flights and an updated safety finding and a flight permit were issued. Details of the safety review board process are included in appendix F.

Prior to all research data flights, several in-flight calibrations were required for the air data probe. The probe pitot-static system was calibrated using a GPS 4-leg maneuver. The probe AoA vane was calibrated using steady trim shots during the GPS 4-leg maneuver. Details of in-flight calibrations, theory, practical considerations, and results are included in appendix B.

10. THE RESULTS OF THE 22 APRIL 2015 FLIGHT TEST

A single test flight was conducted at Daytona Beach (KDAB) on April 22, 2015. Two separate DFRDAS systems were installed on the flight test aircraft. The left wing Alpha System probe location and orientation was not changed from the January 21 and 22, 2015 flight tests. The calibration curve from figure 17 was implemented in the left wing DAS (DFRDAS-1) software. Given P_{fwd}/P_{45} from the DAS, the quadratic equation in figure 17 was solved for the AoA. Code was included in the DFRDAS-1 software to check for a negative radical.

Prior to the April 22, 2015 flight test, a second DFRDAS (DFRDAS-2) was built and installed on the right wing of the flight test aircraft. The second DFRDAS hardware was identical to that of the first DFRDAS (DFRDAS-1). The center of the inspection port for the DFRDAS-2 was located at 38.9% of the local chord at the spanwise position shown in figure 20. The basic software installed on the DFRDAS-2 was the same as previously installed on the DFRDAS-1, with the exception of the calibration curve. The wind tunnel calibration curve was implemented in the DFRDAS-2 software.

A 7-point horseshoe heading level flight performance test was conducted at a pressure altitude of 6000'. Again, data points were taken at speeds corresponding to the $V_{L/Dmax}$, V_{CC}, and V_{PRmin} points and at maximum available power (117 KIAS).[2]

Two standard FAA idle power stalls (1 KIAS per second deceleration) were also conducted at an approximate weight of 2835 lbs. The indicated stall airspeed was 51/52 KIAS.

Figure 20. Spanwise location of the right wing probe DFRDAS-2

10.1 LEFT WING DFRDAS-1 RESULTS

The calibration curve coded in the DFRDAS-1 failed to yield AoA values above approximately 12º because of a negative value in the square root radical. The negative square root can be eliminated by interchanging the dependent and independent variables (*x* and *y* axes), as shown in figure 21. The results in figure 21 are based on the horseshoe heading level flight performance test. P_{fwd}/P_{45} was calculated from the raw sensor counts corrected for noload (bias) offset using individual recorded values or P_{fwd} and P_{45}. The AoA was estimated using a lift curve slope of 0.08/deg.

[2] The flight test aircraft was not equipped with wheel pants.

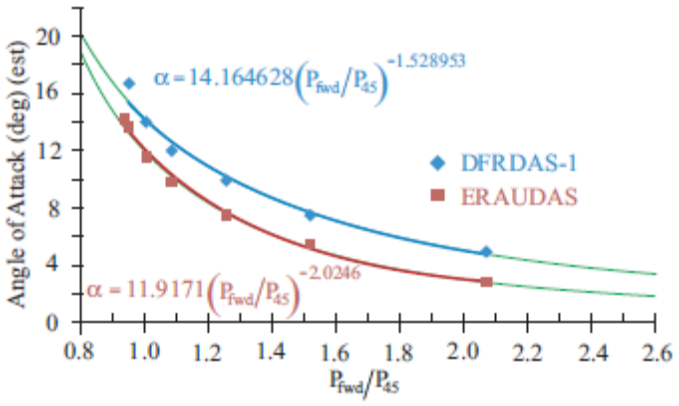

Figure 21. Alpha vs. Pfwd/P45 results for the left wing DFRDAS-1 probe for the April 22, 2015 flight test

Neither a linear nor second-degree (parabolic) fit to the data was acceptable. A power law fit was acceptable, as is shown for both the DFRDAS-1 (blue line) and ERAUDAS (red line). The green lines represent extensions of the appropriate curve fits to both higher and lower AoA. The typical high speed cruise AoA for a retractable light GA aircraft is on the order of 2º. These power law fits provide adequate definition in this AoA range. Furthermore, the power law fits provide adequate definition in the critical AoA range near stall (e.g., 14–18º, as shown by the data in figure 21). The DFRDAS-1 power law curve fit equation, shown in figure 21, is used in the next series of flight tests with the DFRDAS-1.

10.2 RIGHT WING DFRDAS-2 RESULTS

The results for the right wing DFRDAS-2 and ERAUDAS for the horseshoe heading flight test are shown in figures 22 and 23. The AoA for the DFRDAS results was estimated using a lift curve slope of 0.080/deg. The AoA for the ERAUDAS results is based on the alpha/beta probe mounted on the right wing of the aircraft. The values of P_{fwd}/P_{45} are based on the individual values of P_{fwd} and P_{45} corrected for noload (sensor bias) from the DFRDAS-2 AoA DAS. Figure 23 shows that the variation of AoA with P_{fwd}/P_{45} is linear.

The equation in figure 23 was programmed into the DFRDAS-2 for use in later flight tests. The green lines in figure 23 represent extensions of the linear fit equations also presented in figure 23. The black triangle in figure 23 represents the stall AoA determined from the alpha/beta probe mounted on the right wing and ERAUDAS.

The wing-tip alpha/beta boom is calibrated with respect to the FRL (i.e., it is a geometric AoA). The physics-based AoA determined from the horseshoe heading tests is the absolute AoA of the aircraft. The constant term in the fit equations in figure 23 suggests that the angle of 0 lift, with respect to the aircraft's FRL, is $\approx -2.4^{\circ} \pm 0.05^{\circ}$.

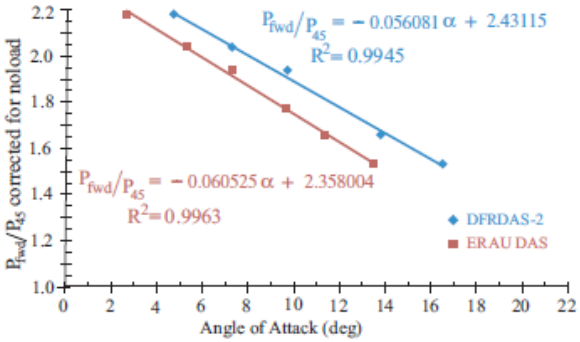

Figure 22. Alpha vs. P_{fwd}/P_{45} results for the right wing DFRDAS-2 probe for the April 22, 2015 flight test

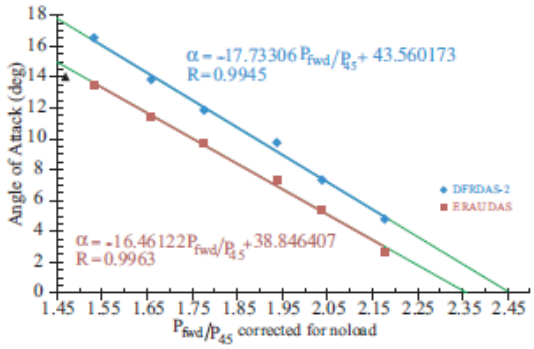

Figure 23. P_{fwd}/P_{45} vs. Alpha results for the right wing DFRDAS-2 probe for the April 22, 2015 flight test

Figure 24 shows AoA plotted against the differential pressure P_{fwd}-P_{45}. This particular presentation is of interest because a number of differential pressure-based AoA systems correlate the differential pressure to AoA. Figure 24 clearly shows that the AoA varies parabolically with differential pressure. P_{fwd}-P_{45} illustrates that in the stall region, the correlation of AoA with P_{fwd}-P_{45} is approximately linear. However, at AoA below the stall region, figure 24 clearly illustrates that the correlation is parabolic. Therefore, at the lower AoA, a linear correlation/calibration provides inadequate accuracy. Thus, differential AoA systems that use a linear correlation with P_{fwd}-P_{45} are essentially only stall warning devices, which are inadequate for other flight regimes.

It should be further noted that normalizing the differential pressure with P_{45} (not shown) eliminates the dependence on dynamic pressure and results in a linear variation.

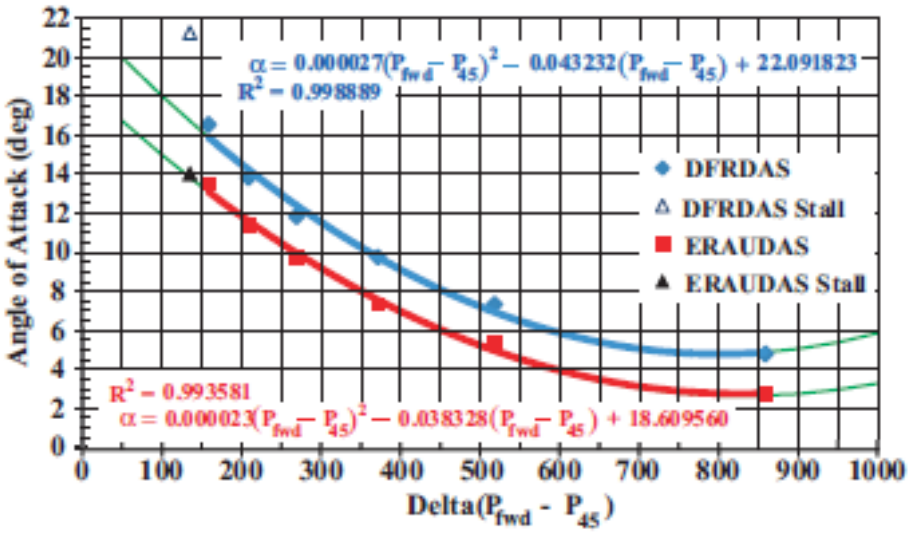

Figure 24. Alpha vs. P_{fwd}/P_{45} results for the right wing DFRDAS-2 for the April 22, 2015 FLIght testStall Flight Tests

Two stall flight tests in the clean configuration were conducted. The standard FAA deceleration of approximately 1 knot per second from approximately 90 KIAS was used. The stall warning horn activated at approximately 58 KIAS. Stall occurred at approximately 51 KIAS.

The results for both tests are shown as CL vs. α curves in figure 25. The AoA used in figure 25 is from the alpha/beta probe mounted on the right wing tip referenced to the aircraft fuselage longitudinal reference line. The dashed black line intercepts the abscissa at approximately -1.75º to yield an estimate of the aircraft angle of 0 lift with respect to the longitudinal reference line. The slopes recorded on figure 25 indicate a lift curve slope of approximately 0.080/deg., which confirms the value calculated above and used to estimate the physics-based absolute AoA.

Figure 26 shows data from Stall 1 acquired using the DFRDAS-2. The absolute AoA was determined using the calibration curve developed from the 4-leg GPS data shown in figure 23. The P_{fwd}/P_{45} values calculated within the DFRDAS-2 during the stall flight test were used to calculate the absolute AoA also within the DFRDAS-1. Figure 26 centers the initial stall break at time 0. Recovery was initiated at approximately 3 seconds and completed at approximately 5 seconds (i.e., a total of approximately 5 seconds from stall break to recovery completion). The maximum absolute AoA was approximately 19.5°, whereas the minimum AoA was approximately 6.5º. Figure 26 clearly indicates that the DFRDAS provides adequate AoA information during stall recovery.

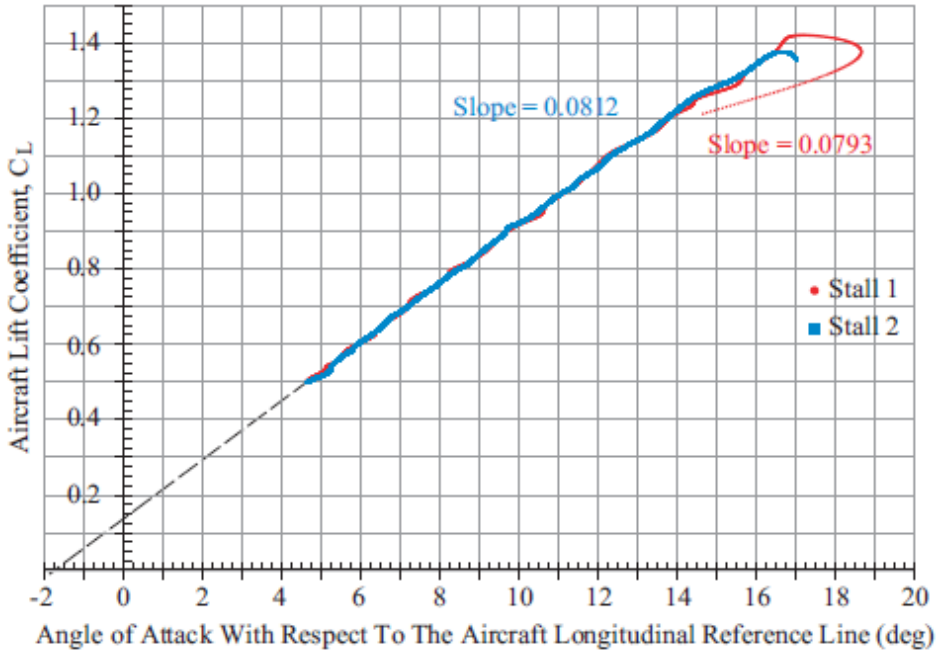

Figure 25. Lift coefficient vs. AoA with respect to the fuselage reference line for two stall flight tests

11. THE RESULTS OF THE MAY 26 AND 27, 2015 FLIGHT TESTS

Two flight tests were conducted at Stevensville, Maryland (W29) on May 26 and 27, 2015. Again, two separate DFRDAS systems were installed on the flight test aircraft. The left wing Alpha System probe location and orientation was not changed from either the January or April 2015 flight tests. The power law calibration curve (blue equation) from figure 21 was implemented in the left wing DAS (DFRDAS-1) software. Code was included in the DFRDAS-1 software to calculate the absolute AoA from the power law calibration equation in real time given P_{fwd}/P_{45}.

Again, the DFRDAS-2 was used to acquire data from the deferential pressure AoA probe mounted at 38.9% local chord on the right wing. The orientation of the right wing probe with respect to the wing's lower surface was not changed from the April 22, 2015 flight test. The software in the DFRDAS-2 used to determine P_{fwd}/P_{45} from the raw pressure sensor output was not changed.

The raw values of $P_{fwd}$and P_{45} were output to data files. These values were used to independently calculate the ratio P_{fwd}/P_{45} and compare to those internally calculated within the DFRDAS.

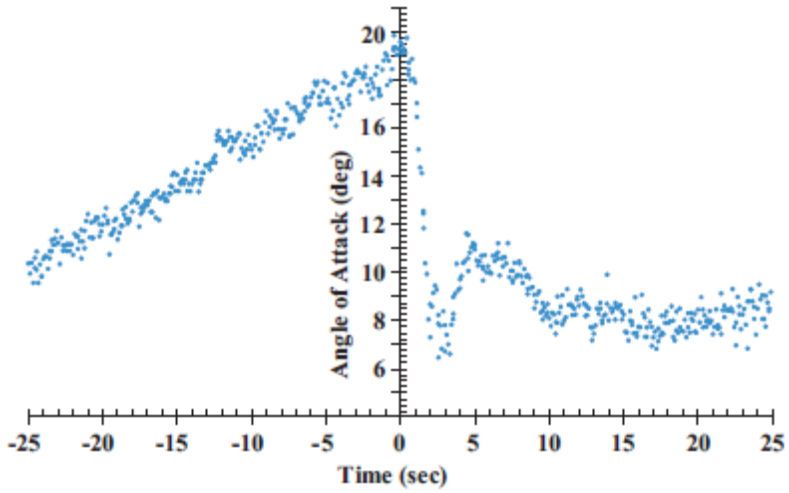

Figure 26. Absolute angle of attack vs. time for stall 1. P_{fwd}/P_{45} data is from DFRDAS-2. The absolute angle of attack is calculated using the calibration curve for the DFRDAS-2 shown in figure 23

A 7-point horseshoe heading level flight performance test was conducted at a pressure altitude of 6000' on May 26, 2015. Again, data points were taken at speeds corresponding to $V_{L/Dmax}$, V_{CC}, and V_{PRmin} intermediate points and at maximum available power (117 KIAS).[3]

A single standard FAA idle power stall in the clean configuration was also conducted on May 26, 2015 at a nominal pressure altitude of 4500'.

The linear calibration curve from the April 22, 2015 flight test, represented by the blue equation in figure 23, was programmed into the software for the DFRDAS-2. Again, software within the DFRDAS-2 was used to determine the absolute AoA from P_{fwd}/P_{45} — calculated in real time by the software.

11.1 LEFT WING DFRDAS-1 RESULTS

The results for the left wing DFRDAS-1, based on the horseshoe heading level flight performance flight test, are shown in figure 27. The blue curve and equation represents a power law fit to the data from the May 26, 2015 flight test. The black curve and equation represent the calibration curve from the April 22, 2015 flight test. Again, a lift curve slope of 0.08/deg. was used to calculate the AoA.

[3] The flight test aircraft was not equipped with wheel pants.

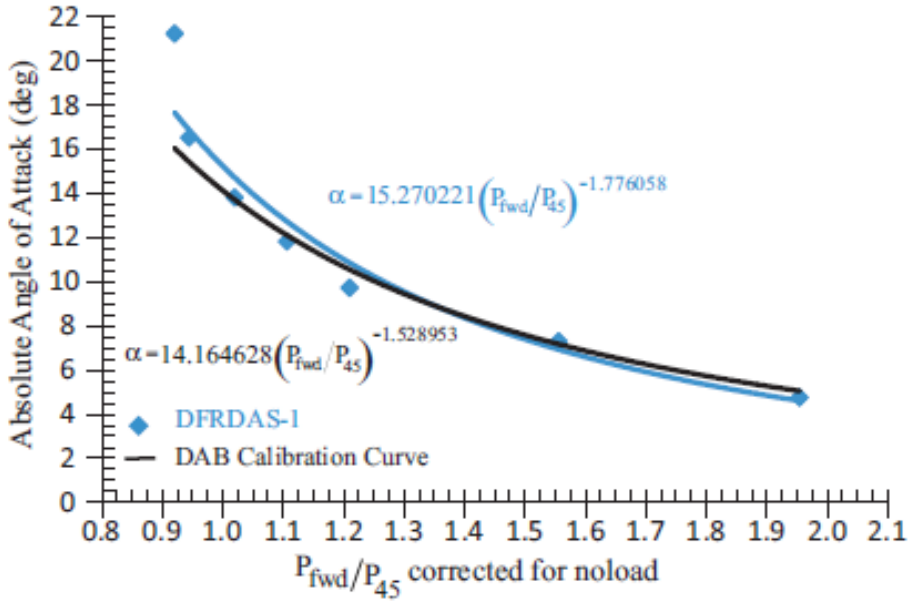

Figure 27. Absolute AoA vs. P_{fwd}/P_{45} for the DFRDAS-1 from the May 26, 2015 FLIght test: the probe is mounted approximately at the leading edge of the left wing of the aircraft

The difference in AoA for a given value of P_{fwd}/P_{45} is likely a result of the method used to determine both the AoA and P_{fwd}/P_{45}. Specifically, the noload value was determined by averaging 100 data points and was not changed, nor should it have been, for the two flight tests. The 100 values for P_{fwd}/P_{45} for each leg of the 4-leg GPS horseshoe heading box pattern were averaged and then the four averaged values averaged again. The four TASs determined from each of the triads of the 4-leg GPS horseshoe heading data were averaged to obtain the TAS for each data point. In short, the values represented by the data points are an average of an average. Finally, the calibration curve was determined by a statistical fit to the averaged data.

The power law curves represent a reasonable approximation to the AoA for medium to low AoA (i.e., for typical cruise and approach conditions). However, notice that near stall, both curves in figure 27 become quite sensitive and tend to underestimate the AoA.

11.2 RIGHT WING DFRDAS-2 RESULTS

The results for the right wing DFRDAS-2 for the horseshoe heading flight test are shown in figure 28. The AoA for the DFRDAS results was estimated using a lift curve slope of 0.080/deg. The values of P_{fwd}/P_{45} are based on the individual values of P_{fwd} and P_{45} corrected for noload (sensor bias) from the DFRDAS-2 AoA DAS. Figure 28 shows the AoA, α, plotted against P_{fwd}/P_{45}. Again, as in the April 22, 2015 test, the variation is linear. The blue equation in figure 25 was programmed into the DFRDAS-2 and is shown here as the black line and equation. The differences between the linear fits to the data represented by the blue and black lines is attributed to the effect of averaging the averages discussed in appendix D.

Some of the scatter in the data is a result of ringing in the pressure sensors. However, a significant amount of the scatter results from the continuous very small changes in AoA made by the pilot to maintain constant airspeed and altitude without changing power or trim during the data run.

11.3 RIGHT WING FLAPS 40º RESULTS

A four point 4-leg GPS horseshoe heading flight test was conducted at 6000' pressure altitude with full flaps (nominally 40°) extended. The results are shown in figure 29. The flaps' 0 calibration curve from figure 28 is shown for comparison. Figure 29 again shows a linear calibration curve with flaps extended. Figure 29 also shows that P_{fwd}/P_{45}, for a given AoA, is larger with flaps extended than without flaps extended. In addition, the slope of the calibration curve is approximately twice that with 40º flaps extended than without flaps extended. It is known from NACA airfoil data [13] that flap extension beyond approximately 30° changes the lift curve slope. Additional flight tests at lower flap extensions may change the results seen with 40° flap extension.

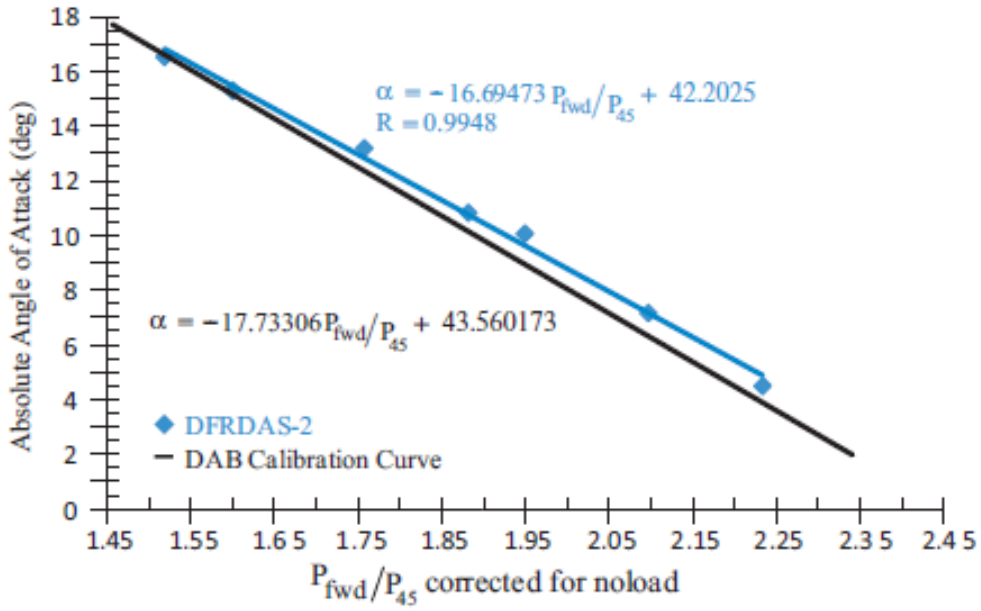

Figure 28. Absolute AoA vs. P_{fwd}/P_{45} for the DFRDAS-2 from the May 26, 2015 flight test: the probe is mounted at 38.9% of the local chord on the right wing of the aircraft

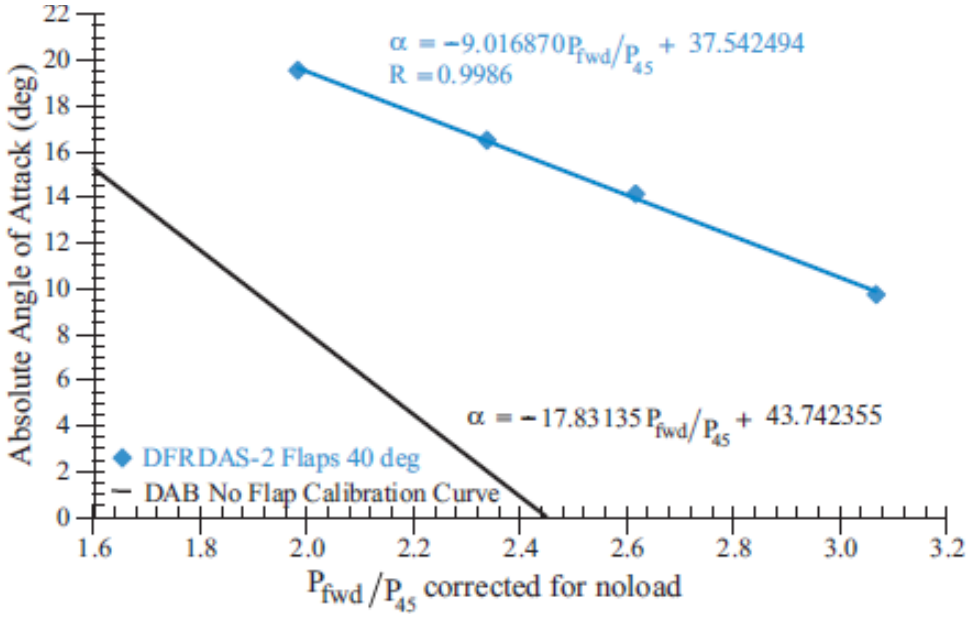

Figure 29. Absolute AoA vs. P_{fwd}/P_{45} for DFRDAS-2 for the May 27, 2015 flight test with flaps extended to 40º: the probe is mounted at 38.9% local chord on the right wing

12. AERODYNAMICS OF WHY A LINEAR CALIBRATION CURVE?

AERODYNAMICS OF WHY A LINEAR CALIBRATION CURVE?

Figure 30 shows two frame grabs (see appendix C for additional information) from a 1938 NACA film [19], which illustrate the underlying principle that results in a linear calibration curve for under wing mounted differential AoA probes. The airfoil in the frame grabs is a symmetrical airfoil.

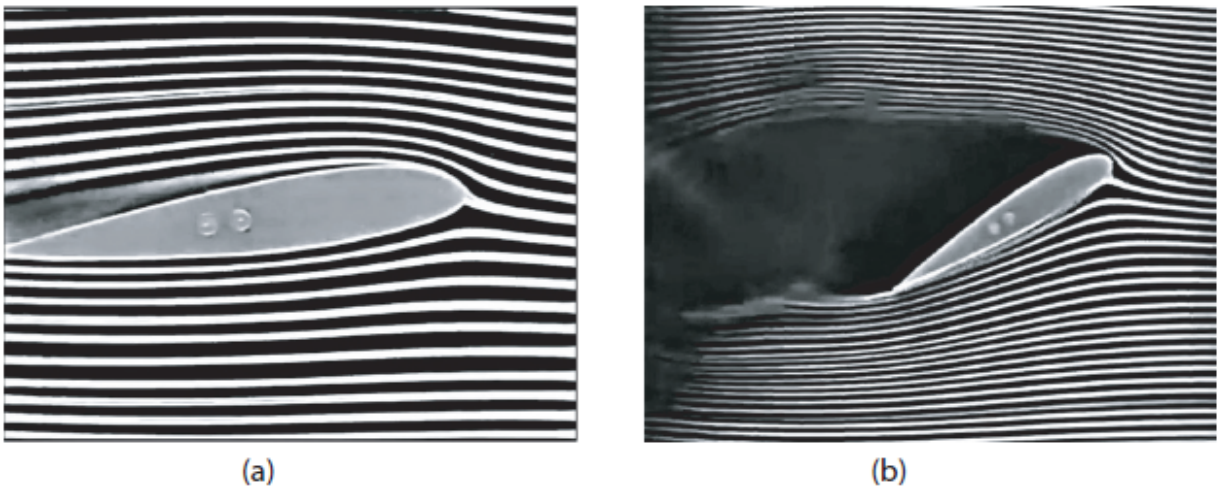

Figure 30. Two frame grabs showing the streamlines around an airfoil without flaps extended

The pressure on the surface of the airfoil referenced to the free stream (atmospheric) pressure is positive in the vicinity of the stagnation point but generally negative on the upper surface and may be negative or positive on the lower surface (figure 31). Generally, other than near the stagnation point, if the pressure relative to the atmosphere pressure is positive on the lower surface, it is positive at low AoA near the trailing edge or when flaps are deployed.

Also pertaining to figure 31, notice that the pressure is typically below atmospheric pressure except near the leading and trailing edges. Therefore, the pressure is increasing away from the airfoil surface. Because P_{fwd} has a significant dynamic pressure component for typical AoA, P_{fwd} is larger than P_{45}. Therefore, provided that the AoA probe is mounted behind the forward stagnation positive pressure region and ahead of the trailing edge positive pressure region, the P_{fwd}/P_{45} pressure ratio smoothly varies as the AoA changes. The data from the current flight tests suggest that the variation is linear.

Figure 32 shows several frame grabs for the video [19] for the same airfoil with a flap deployed. Again, the streamlines on the lower surface are smooth and remain smooth with increasing AoA. Therefore, the pressure field on the bottom of the airfoil is also smooth. Thus, the AoA probe behaves in a similar manner as without a flap deployed, as figure 29 confirms.

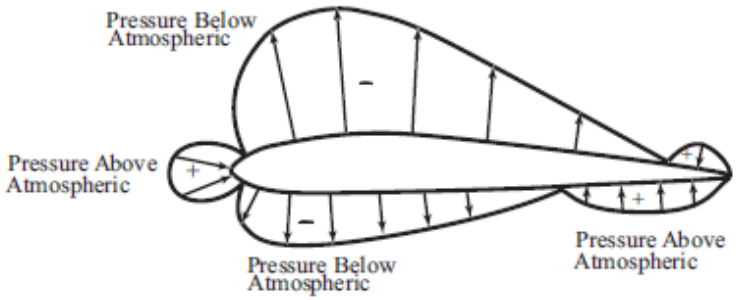

Figure 31. Sketch of the pressure distribution on the surface of a typical airfoil

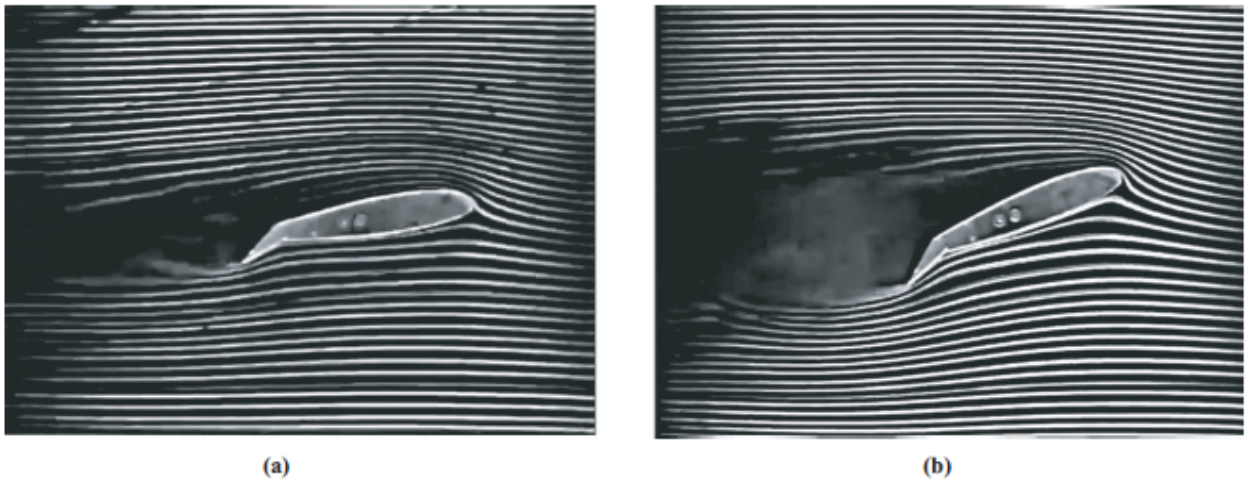

Figure 32. Frame grabs showing the streamlines around an airfoil with a flap extended

13. THE RESULTS OF THE AUGUST 18 AND 19, 2015 FLIGHT TESTS

Additional flight tests were conducted, at Stevensville, Maryland (W29) on August 18 and 19, 2015. The purpose of the flight tests was to investigate the ability of the DFRDAS to provide adequate response during the approach to a stall, during a stall, and during the recovery phase of a stall.

The DFRDAS-2 was used for these flight tests. The orientation of the right wing probe (DFRDAS-2), located at 38.9% of the local chord, was not changed from the April 22, 2015 flight test. The software in the DFRDAS-2 used to determine P_{fwd}/P_{45} from the raw pressure sensor output was not changed. The software in the DFRDAS-2 used to calculate the AoA from P_{fwd}/P_{45} was updated with the linear calibration curve from the May 26, 2015 flight test represented by the blue equation in figure 30.

As in all the flight tests, raw values of P_{fwd} and P_{45} were output to the data files. These values were used to independently calculate the ratio P_{fwd}/P_{45} and compare it to those calculated within the DFRDAS.

A 5-point horseshoe heading level flight performance test was conducted at a pressure altitude of 6000' on August 18, 2015. Data points were taken at speeds corresponding to $V_{L/Dmax}$, V_{CC}, close to stall, and at maximum available power (117 KIAS).
In addition, five standard FAA stalls (1 kts/sec deceleration) were conducted in the clean configuration at 0° bank angle, left and right 20°, and left and right 30° bank angles. Finally, two accelerated stalls (5 kts/sec deceleration) were conducted in the clean configuration.

On August 19, 2015, three standard FAA stalls were conducted with flaps extended 21.5° at 0° bank angle, right 20°, and right 30° bank angles. Finally, two 5 kts/sec deceleration stalls were conducted at 0° bank angle with flaps extended 21.5° and 31°.

13.1 RIGHT WING DFRDAS-2 RESULTS

The results for the right wing DFRDAS-2 for the horseshoe heading flight test are shown in figure 33 combined with the results from the April 22, 2015 and May 26 and 27, 2015 flight tests. Individual flight test results are shown by different colored dots. The black line and equation represent the least squares fit to all horseshoe heading flight tests. Figure 33 clearly illustrates the repeatability of the right wing DFRDAS-2 data. Again, some of the scatter in the data is attributed to using the average of the averages of the DFRDAS-2 data stream and to the small continuous pilot inputs required to maintain heading, airspeed, and altitude without changing the power available or trim.

13.2 STALL RESULTS

The full stall results are presented in appendix E. A selection is presented here.

Figure 34 illustrates the results for a standard FAA stall in the clean configuration. The graph is centered on the stall. The data shown are a result of a 3-point moving average. A 3-point moving

average makes interpretation of the results easier. The red dots spaced along the blue line represent individual data points.

Figure 34 shows a constant AoA increase of approximately 0.2° per second or a deceleration of 1 kts/sec. The stall occurs at approximately 0.5 second and recovery occurs at approximately 3 seconds. During the 2.5-second recovery, approximately 30 red dot data points are displayed.

Figure 35 shows the results for a standard FAA accelerated stall (i.e., a deceleration rate of 5 kts/second or an increase in AoA of approximately 1.0° per second). The stall occurs at time 0, with recovery (pitch down) at one second. There are approximately 16 red dots displayed during the recovery. The graph shows a characteristic AoA increase, of 4° in this case, beginning at 1 second, followed by a secondary AoA decrease. Recovery is completed by a smooth return to a constant AoA.

Figure 36 shows the results for a standard FAA stall in a right 20° bank. Stall occurs at approximately 0.25 second and the initial recovery occurs at approximately 1.5 seconds. There are an estimated 14 red dot data points displayed during the recovery. The maximum AoA recorded is approximately 19.5°. Recovery occurs at approximately 9.5°, followed by the typical increase and decrease in AoA, with a final smooth transition to level flight.

A stall was also conducted in a left 20° bank and the left and right 30° banks with similar results. Complete results are given in appendix E.

On May 27, 2015, a stall was conducted at 0 bank angle and 40° flaps extended. At the stall, the stick was held aft. The aircraft then entered a limit cycle oscillation, as shown in figure 37. After four oscillations, the stick was moved forward for stall recovery. The total indicated AoA change during recovery was approximately 37° in approximately 1 second. The total number of displayed red dot data points acquired, as shown in figure 36, was 16. These figures, along with figure 26, clearly illustrate that the DFRDAS data acquisition rate is acceptable for all normal flight conditions as well as abusive stall cases.

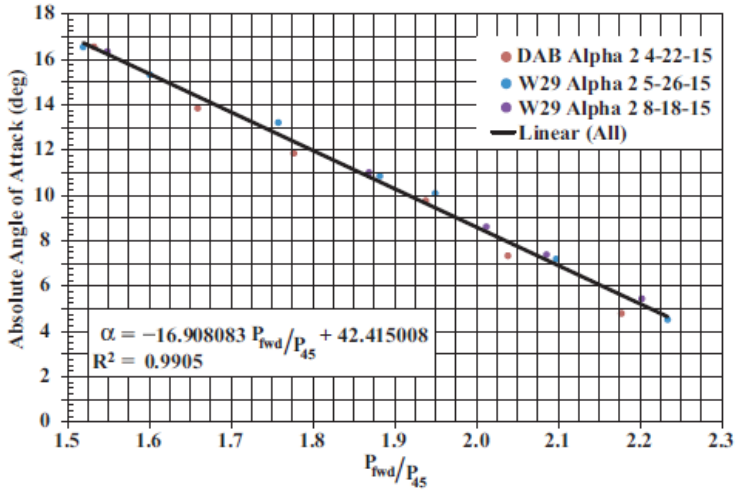

Figure 33. Combined linear fit for absolute AoA vs. P_{fwd}/P_{45} in the clean configuration with the right hand probe at 38.9% of local chord

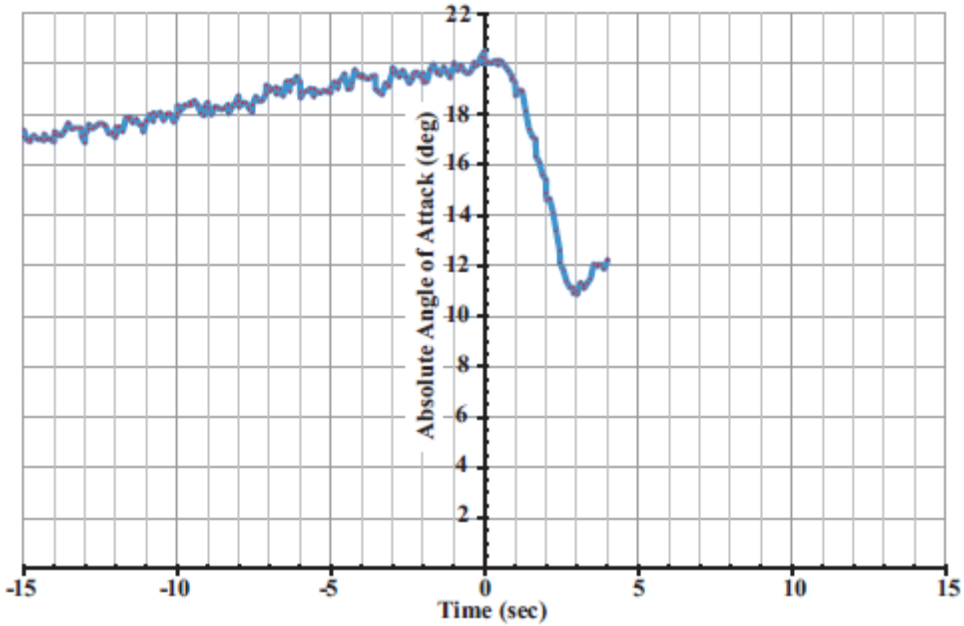

Figure 34. The DFRDAS-2 results for a standard FAA stall in the clean configuration with the probe at 38.9% of the local chord. The curve is based on a 3-point moving average of the raw data. The red dots represent individual smoothed data points

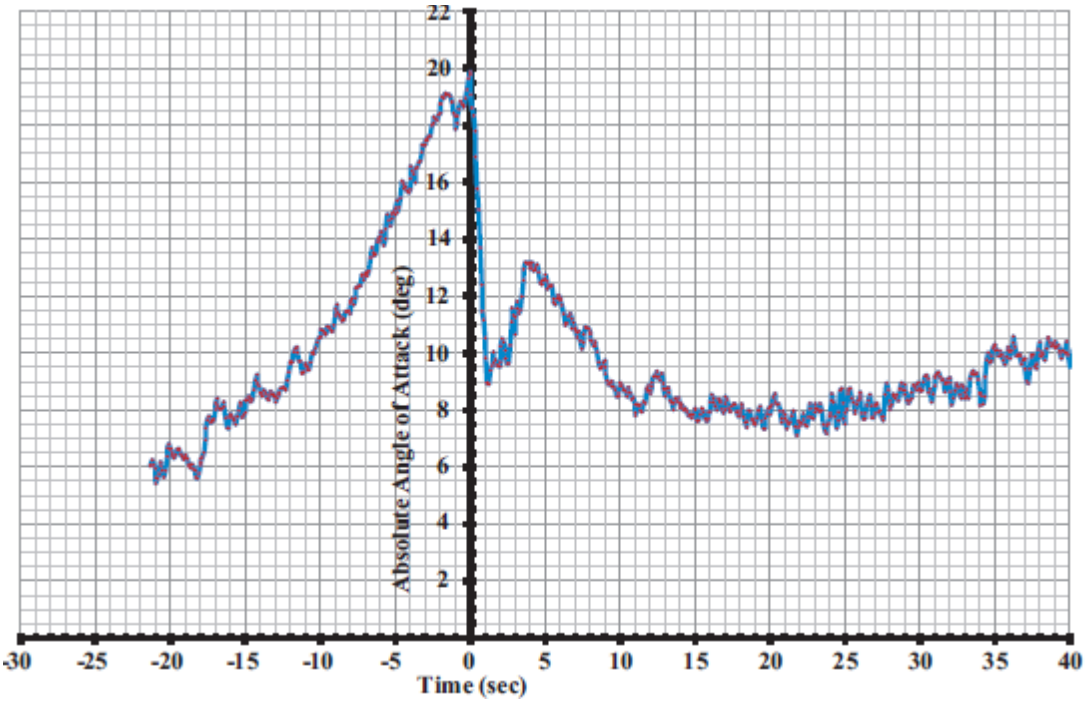

Figure 35. DFRDAS-2 results for a standard FAA stall in the clean configuration with the probe at 38.9% of the local chord. The curve is based on a 3-point moving average of the raw data. The red dots represent individual smoothed data points

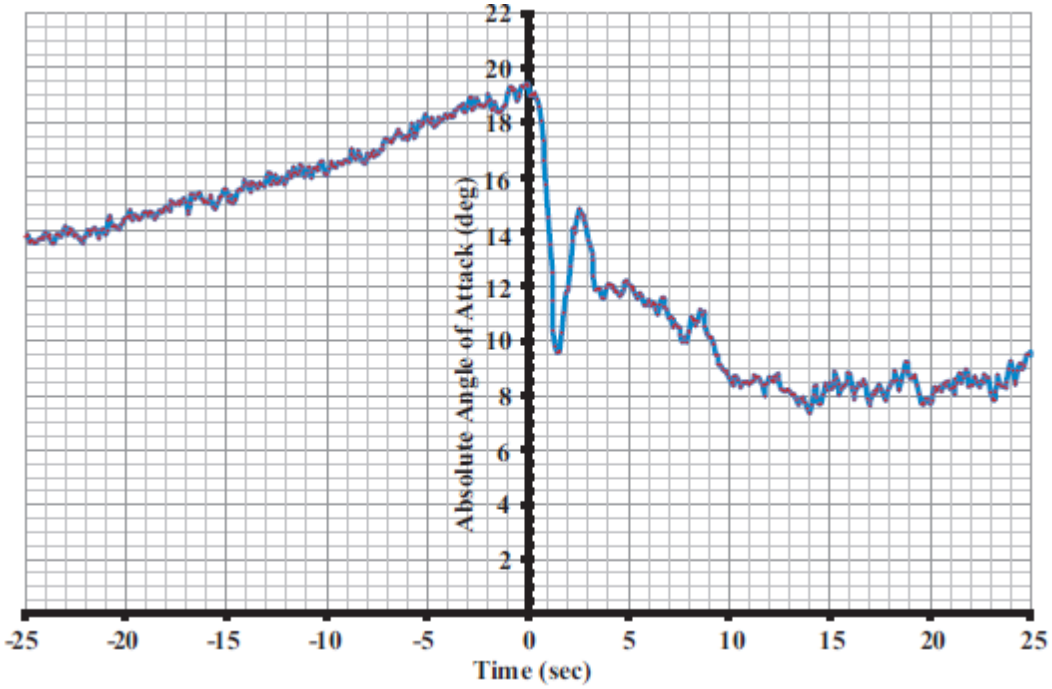

Figure 36. DFRDAS-2 results for a standard FAA stall in the clean configuration in a right 20º bank with the probe at 38.9% of the local chord. The curve is based on a 3-point moving average of the raw data. The red dots represent individual smoothed data points

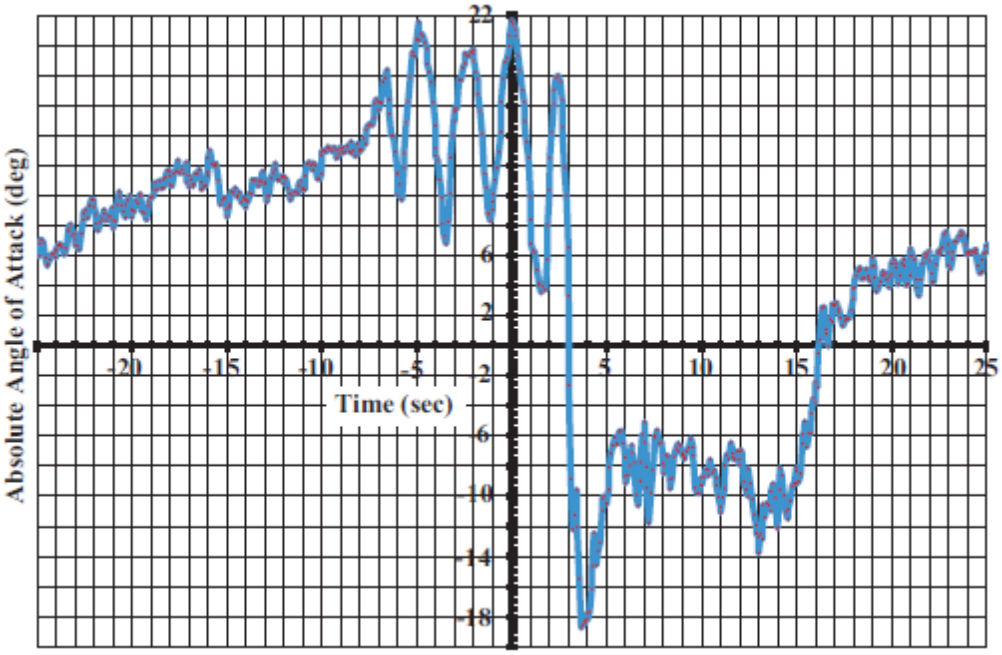

Figure 37. DFRDAS-2 results for a standard FAA stall with 0 bank and 40º flap extended with the probe at 38.9% of the local chord. The curve is based on a 3-point moving average of the raw data. The red dots represent individual smoothed data points

14. WHAT WORKS AND WHAT DOES NOT WORK

Four AoA vs. various pressure relationships were investigated. These were:

a. AoA vs. P_{fwd}/P_{45}
b. AoA vs. $(P_{fwd}-P_{45})/P_{45}$
c. AoA vs. $(P_{fwd}-P_{45})/q$, where q is the freestream dynamic pressure
d. AoA vs. $(P_{fwd}-P_{45})$ (i.e., the unnormalized differential pressure)

The results from the May 26 and 27, 2015 flight tests for the right wing probe mounted at 38.9% of the local chord are used to illustrate which of these techniques yields an accurate AoA throughout the aircraft's AoA range.

Figure 38 illustrates the results obtained for each of the independent parameters listed above. The AoA probe was located on the right wing at 38.9% of the local wing chord. Both the absolute AoA derived from the 4-leg GPS TAS and the geometric AoA referenced to the aircraft longitudinal reference line are shown. Both AoA show consistent behavior. The green lines in figure 38 represent extensions of independent variable for the calibration curve above and below the flight test data.

The highest AoA displayed represents an indicated airspeed of 58 KIAS, whereas the lowest AoA displayed represents an indicated airspeed of 117 KIAS. The aircraft POH gives 70 KIAS for the speed for L/D_{max}. The aircraft calculated AoA for L/D_{max} was approximately 12.4°, represented by the fourth blue dot from the right in figure 38 at an absolute AoA of approximately 11.9°. The

speed for Carson Cruise is estimated at 94 KIAS, represented by the second blue dot from the right in the figure 38. The estimated absolute AoA for Carson Cruise is 7°, again represented by the second blue dot from the left in figure 38 at 7+°.

Figure 38(a), with P_{fwd}/P_{45} as the independent variable, shows linear calibration curves for AoA vs. P_{fwd}/P_{45} throughout the aircraft's AoA range. The absolute AoA, represented by the blue line, is consistently higher than the geometric AoA, as it should be, given that the angle of 0 lift is negative with respect to the aircraft's longitudinal reference line. Figure 38(a) is the best choice for a stable calibration curve. An appropriate calibration curve can be obtained by flying constant heading, altitude, and power at two points. However, three or four points at approximately 1.1–1.2 V_{stall}, $V_{L/Dmax}$, $V_{CC,}$ and typical altitude cruise are recommended for additional accuracy.

Figure 38(b), with $(P_{fwd}\text{-}P_{45})/P_{45}$ as the independent variable, also shows a linear calibration curve throughout the aircraft's AoA range, as expected. After all, $(P_{fwd}\text{-}P_{45})/P_{45} = P_{fwd}/P_{45}\text{-}1$. Notice that the slope of the $(P_{fwd}\text{-}P_{45})/P_{45}$ and the P_{fwd}/P_{45} calibration curves are essentially the same. The values of $(P_{fwd}\text{-}P_{45})/P_{45}$ were calculated from the individual values of P_{fwd} and P_{45}. There may be some advantage, or disadvantage, to directly measuring $(P_{fwd}\text{-}P_{45})$ and separately measuring P_{45}. In the latter case, the issue of the reference pressure for P_{45} needs addressing. This effort was not within the scope of the current investigation.

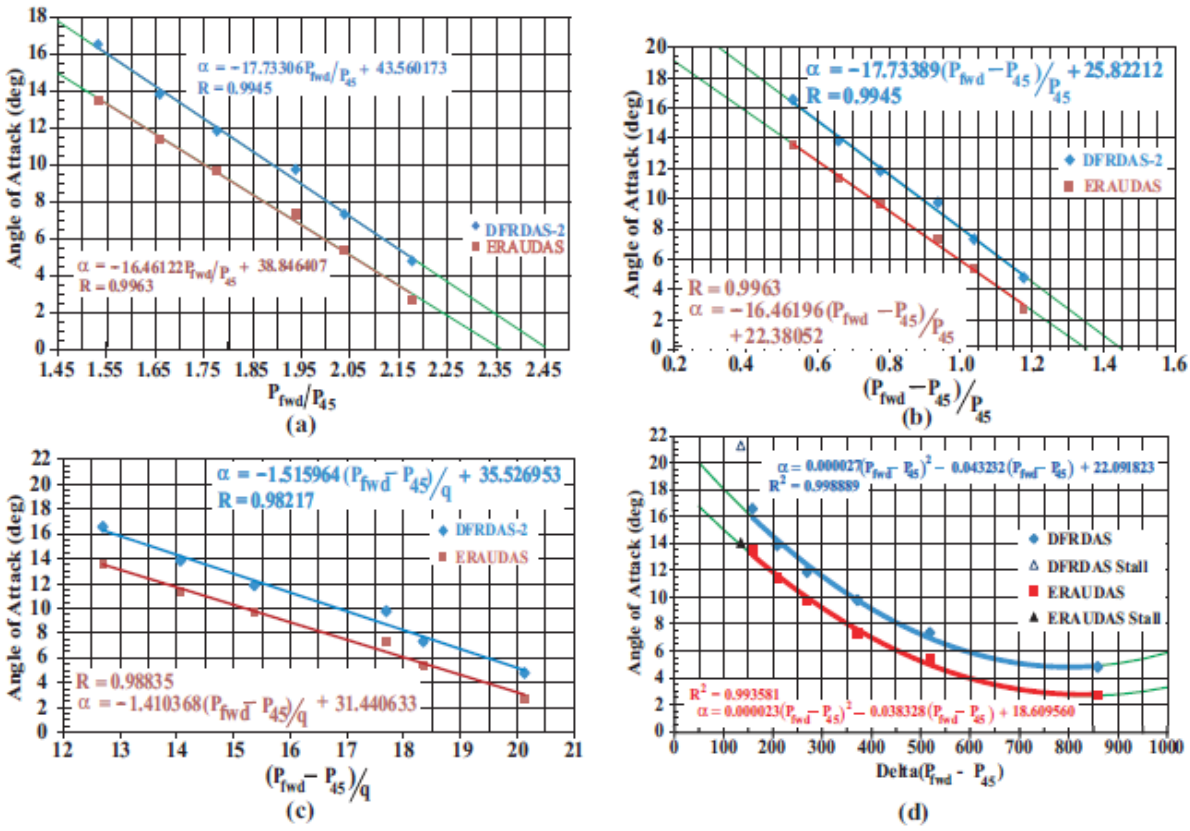

Figure 38. What works and what does not work: AoA vs. (a) P_{fwd}/P_{45}, (b) $(P_{fwd}\text{-}P_{45})/P_{45}$, (c) $(P_{fwd}\text{-}P_{45})/q$, (d) Delta $(P_{fwd}\text{-}P_{45})$

Figure 38(c), with (P_{fwd}-P_{45})/q as the independent variable, shows a linear calibration curve. Recall that (P_{fwd}-P_{45}) is the differential pressure and q is the freestream dynamic pressure. Specifically, q is not the dynamic pressure derived from the pitot-static system. This is a subtle, but important, point. Most aircraft's pitot-static systems require correction at low speed/high AoA near stall because of errors in either the pitot tube or the static pressure readings. If these corrections are not incorporated into the AoA system, it is unlikely that a linear calibration with (P_{fwd}-P_{45})/q will result. Similar results may be expected for other differential pressure systems.

Figure 38(d), with simply the unnormalized differential pressure (P_{fwd}-P_{45}) as the independent variable, does not show a linear calibration for AoA vs. (P_{fwd}-P_{45}). The best fit is a second-degree polynomial, as shown by the red and blue lines in figure 38(d). The green lines represent extensions of the polynomial fits to both lower and higher AoA. In the low AoA (high-speed) regime, the polynomial fit "turns up," which results in an ambiguous AoA. If simple unnormalized differential pressure is used as the independent variable, a multipoint chordwise approximation using a near stall speed, V_{PRmin}, $V_{L/Dmax}$, V_{CC}, normal cruise speed, and high-speed cruise, as suggested by Rogers [2], yields acceptable results.

15. CONCLUSIONS

- A differential pressure-based COTS AoA data acquisition system (DAS) was designed, successfully reduced to practice, wind tunnel tested, and flight tested.
- The accuracy of the differential pressure AoA system was determined to be 0.25–0.5°.
- A data rate of 17 samples/sec or better was achieved during all the flight tests, including during all phases of FAA standard and accelerated stalls, approach to stall, full stall, and stall recovery.
- Use of the local ambient pressure as the reference for the differential pressure sensors was confirmed in practice.
- The repeatability of the data from the COTS DAS was proven in flight tests.
- A calibration curve based on the ratio P_{fwd}/P_{45} was linear throughout the aircraft's AoA range if the probe was mounted in an inspection port on the bottom of the wing, the center of which was located between an estimated 25%–60% of the local wing chord. Similar results may be expected for other differential pressure systems.
- The linear calibration curve results because the flow remains attached on the lower surface of the wing and varies smoothly in the pressure field between the wing's lower surface and the far field static (atmospheric) pressure below the wing throughout the entire aircraft's AoA range, including stall with and without a deflected flap
- A physics-based determination of AoA was successful if a reasonably accurate aircraft lift curve was determined. Calculation of the lift curve slope was within 0.01/deg. of the value determined by the flight test using an alpha/beta probe.
- With the AoA probe mounted at the leading edge of the local chord, a power law calibration curve cast as AoA vs. P_{fwd}/P_{45} provides a better fit to the data than a parabolic or linear fit. For a limited range of high AoA near stall, a linear fit to the data provides adequate accuracy. However, accuracy at low AoA, such as required by cruise, is poor. Therefore, systems similar to that tested, mounted near the leading edge and using a linear calibration, are basically only stall warning devices.

- Using unnormalized differential pressure (P_{fwd}-P_{45}) does not provide adequate accuracy throughout the aircraft's AoA range. This technique is dynamic pressure dependent. Similar results may be expected for other differential pressure systems.
- For a limited range of high AoA near stall, a linear fit to the data provides adequate accuracy. However, accuracy at AoA, such as required by cruise, is poor. Therefore, systems similar to that tested, using a linear calibration, are basically only stall warning devices.
- Normalizing the differential pressure with aircraft dynamic pressure is impractical in the aftermarket because of the necessity to include the aircraft's high AoA (low speed) pitot-static correction to achieve the required accuracy.

16. SUGGESTED FUTURE WORK

- More carefully determine the acceptable local chord range for probe location. Conduct flight tests to confirm proper operation from 25%–60% chord.
- Determine the sensitivity of the probe to flap deflection (e.g., flaps 10°, 20°, and 30°).
- Conduct a literature search to determine whether studies of the lower surface far field exist.
- Explore the behavior of the pressure field between the lower surface of the wing and the far field using particle image velocimetry, computational fluid dynamics, and flight test studies.
- Study the effect of "ringing/jitter" in AoA display, including the ergonomic effect on pilot acceptance and interpretation as well as techniques for reducing or eliminating the effect.
- Little is known about the variation with distance from the wing of the pressure field between the lower surface of the wing and the far field; therefore, the distance between the P_{fwd} and P_{45} ports on the AoA probe may significantly influence the performance of the probe. Use CFD, wind tunnel tests, or flight tests to explore this effect on probe performance.
- Conduct tests of alternate display configurations for presenting AoA information to the pilot.
- Relax the original requirement for installing the probe in an existing inspection plate.
- Convey to the developers that only P_{FWD}/P_{45} or $(P_{FWD}-P_{45})/P_{45}$ correctly (linearly) normalizes the dynamic pressure effect.
- Convey to the developers that using only $P_{FWD}-P_{45}$ does not yield an accurate AoA indication because it is only a stall warning device.
- Convey to the developers that, in their installation instructions, the probe should be mounted on the wing opposite the standard stall warning device to provide stall warning in both a left- and right-hand turn.
- Develop an advisory circular on differential pressure, transducer-based AoA DAS.

17. REFERENCES

1. Perkins, C.D. and Hage, R.E., Airplane Performance Stability and Control, John Wiley & Sons, New York, 1949.

2. Rogers, D.F., "Investigation of a General-Aviation Differential Pressure Angle-of-Attack Probe," Journal of Aircraft, vol. 50, No. 5, September–October 2013, pp. 1668–1671.

3. Gracey, W, "Summary of Methods of Measuring Angle of Attack on Aircraft," NACA TN-4351, August 1958.

4. Arend, D.J. and Saunders, J.D., "An Experimental Evaluation of the Performance of Two Combination Pitot Pressure Probes," NASA Technical Paper TP-2009-215632M, October 2009.

5. Letter from the FAA Small Airplane Directorate to DepotStar Inc., December 15, 2011.

6. BMP085 Digital Pressure Sensor Data Sheet, Bosch Sensortec, Palo Alto, CA 94303.

7. MS4525DO Data Sheet, Measurement Specialties Inc., available at www.meas-spec.com (accessed on 02/01/2016).

8. Garrick, I.E., "Determination of the Theoretical Pressure Distribution for Twenty Airfoils," NACA TR-465, 1934.

9. Fox, D., "Is Your Speed True?" Kitplanes, February 1995, pp. 49–50.

10. Lewis, G., "A Flight Test Technique Using GPS for Position Error Correction Testing," Cockpit, January–March 1997, pp. 20–24.

11. Cessna Model 182Q Pilot's Operating Handbook, Cessna Aircraft Corporation.

12. Anderson, J.D. Jr., Introduction to Flight, McGraw-Hill Publishing Company, New York, 1989.

13. Abbott, I.H., von Doenhoff, A.E., and Stivers, L.S. Jr., "Summary of Airfoil Data," NACA TR-824, 1945. Also available as Abbott, I.H. and von Doenhoff, A.E., Theory of Wing Sections Including a Summary of Airfoil Data, Dover Publications, New York, 1959.

14. Wood, K.D., "Aerospace Vehicle Design, Vol. 1, Aircraft Design," Johnson Publishing Company, Boulder, CO, 1963.

15. "Limit Maneuvering Load Factors," available at http://www.gpo.gov/fdsys/granule/CFR-2011-title14-vol1/CFR-2011-title14-vol1 (accessed on 01/27/2016).

16. “Solid Works Finite Element Analysis,” available at www.solidworks.com (accessed on 01/27/2016).

17. Solid Works Fluid Flow Analysis, available at www.solidworks.com (accessed on 01/27/2016).

18. Online bending mount calculator, available at http://bendingmomentdiagram.com (accessed on 01/27/2016).

19. NACA, “Aerodynamics: Airfoil Cambers, Flaps, Slots-Slats and Drag “Smoke Lifts,” National Advisory Committee for Aeronautics, circa 1938, Langley Research Laboratory, available at https://www.youtube.com/watch?v=q_eMQvDoDWk (accessed on 02/01/2016).

APPENDIX A—DETAILS FOR THE ARDUINO-BASED COMMERCIAL OFF-THE-SHELF SYSTEM

The commercial off-the-shelf data acquisition system (DAS) consists of the Arduino UNO, two Measurement Specialties MS4525 0–1 psi differential pressure sensors, a Bosch BMP085 altitude/pressure sensor, and various resistors and capacitors, as detailed in figure A-1. The pressure sensors, Bosch BMP085 (or BMP180), and the small parts are mounted on a Proto shield, which attaches to the UNO. The pinouts are also illustrated in figure A-1.

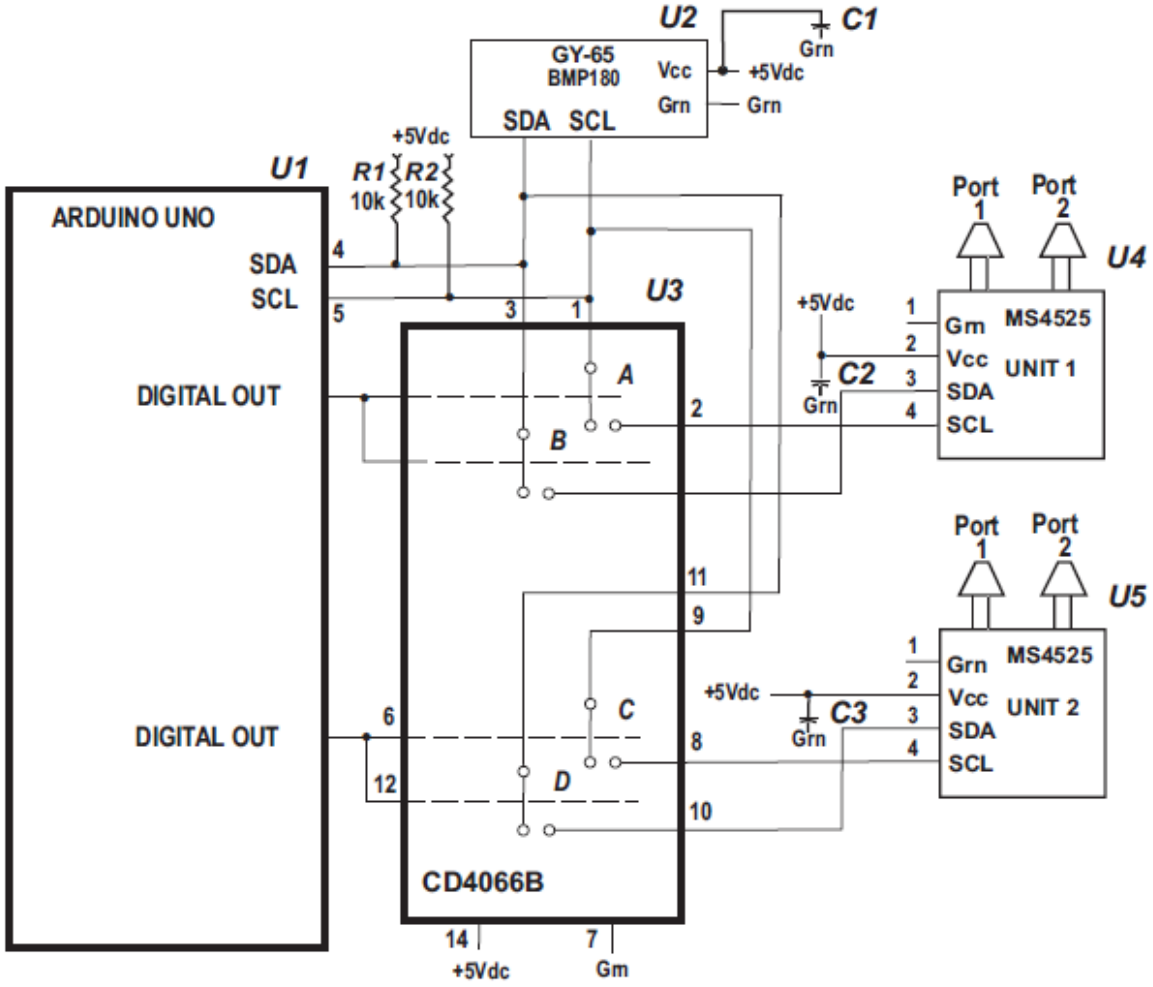

Figure A-1. Block diagram for Arduino DFRDAS

A list of parts, sources, and costs are shown in table A-1.

Table A-1. Parts list and costs—DFRDAS

	Item	Mfr	Mfr No.	Qty	Source	Cost
1	Arduino UNO R3 DIP Edition	Arduino	A000066	1	Newark Elec.	$22.92
2	Proto Shield for Arduino UNO	N/A	STR 104B2P	1	Adafruit	$5.00
3	Bosch GY-65 (BMP085 or BMP180)	Bosch	GY-65/BMP085	1	Component City	$8.75
4	MS4525DO	Measurement Specialties	4525DO - DS 5AI001DP	2	Servoflo Corp.	$42.00
5	CD4066BE	Texas Instruments	CD4066BE	1	Newark Elec.	$0.48
6	Capacitor Alum Elec 0.1 microF 35V 20%	Multicomp	MCMHR63V104 MAX7	2	Newark Elec.	$0.45
7	Cable USB 3FT	Multicomp	SPC20065	1	Newark Elec.	$2.31
8	Resistor, Carbon Film 4.7k Ohm 0.25 W 5%	Multicomp	MCF 0.25W 4K7	2	Newark Elec.	$0.60
9	Tubing Fitting	Avery Tools	SA-F1	2	Straight Female	$9.42
10	Adapter	Cole-Parmer	EW-06365-42	2	1/8″ Male Pipe to 1/8″ Barb	$0.92

The Arduino sketch (program) begins with declaration of the global variables followed by setting up the pins, allowing communication with the hardware (see figure A-2). The main loop first gets the atmospheric pressure from the Bosch BMP085 (or BMP180). Because only MS4525 sensors with a common I2C address were available, it was necessary to multiplex accessing the two MS4525 pressure sensors for P_{fwd} and P_{45}. The P_{fwd} and P_{45} pressure values are acquired as raw counts in the range of 0–16,383. These values are corrected by subtracting the noload values corresponding to 0 differential pressure. The ratio P_{fwd}/P_{45} is then calculated using the noload-corrected P_{fwd} and P_{45} values. The angle of attack (AoA), α, is then determined from the calibration equation. Finally, the result is either printed or displayed, as required.

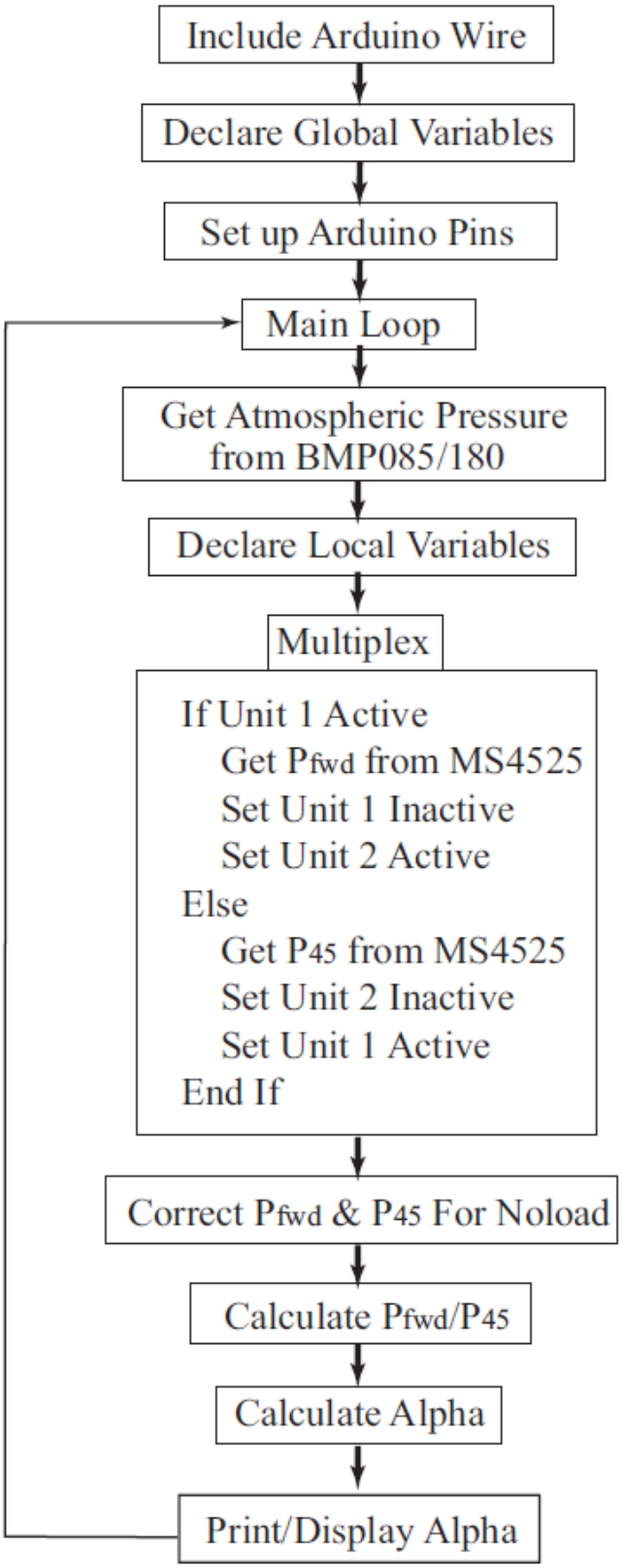

Figure A-2. Block diagram for Arduino DFRDAS sketch (program)

The Arduino code listing that follows is for the DFRDAS AoA DAS used in the flight tests. The linear calibration curve is based on the composite flight test curve shown in figure 41 of the main document. During those flight tests, the probe was mounted at 38.9% of the local wing chord. The calibration curve should be adjusted for any other wing location (see lines 95 and 96 of the following code). The noload values should be adjusted for individual sensors (see lines 98 and 99 of the following code). The probe location should be between an estimated 25% and 60% of the local wing chord outboard of the wing flap.

Arduino Listing:

```
1 // Name: Bar_and_Diff_pressure_V1_4_2.ino
2 // Version: 1_4_2
3 // Date: 29 July 2015
4 // Author: Francisco Rodriguez
5 // Calibration: Alpha2 Linear From DAB 5-26/27/2015
6
7 // Arduino 1.0+ Only
8
9 /* Based largely on code by Jim Lindblom
10
11 // Bar_and_Diff_pressure_V1_4_2
12
13 Get pressure, altitude, and temperature from the BMP085.
14 Serial.print it out at 9600 baud to serial monitor.
15 */
16
17 #include <Wire.h>
18
19 #define BMP085_ADDRESS 0x77 // I2C address of BMP085
20
21 const unsigned char OSS = 0; // Oversampling Setting
22
23 // Calibration values
24 int ac1;
25 int ac2;
26 int ac3;
27 unsigned int ac4;
28 unsigned int ac5;
29 unsigned int ac6;
30 int b1;
31 int b2;
32 int mb;
33 int mc;
34 int md;
35 float pressurepsi;
36 float altitudefeet;
37 float temperaturec;
38 int ver = 142;
39
40
41 // Definitions for Delta Pressure sensor
42
43 int press_address = 40; //1001000 written as decimal number
44 int reading = 0;
```

```
45 int mask = 63; //(0 0 1 1 1 1 1 1 )
46 int maskstatus = 192; //(1 1 0 0 0 0 0 0 )
47 int Status;
48 float deltapressure;
49 float deltapressure1;
50 float deltapressure2;
51
52 // Definitions for Alpha Calculations
53
54 float pfwdnoload, p45noload;
55 float pfwd, p45;
56 float pfwd_p45, Alpha; // pfwd_p45 is Pfwd/P45
57 float pfwdcorr, p45corr, Dtarepfwd,Dtarep45,deltanoloadpfwd;
58 float deltanoloadp45, psi_count;
59 float A, B;
60
61 // Definitions for LED Control
62
63 int led13 = 13;
64 int num1 = 0;
65 int led = 1;
66
67 int unit = 1; // 1 = unit1 selected, 2 = unit2 selected
68
69 // b5 is calculated in bmp085GetTemperature(...)
70 // the b5 variable is also used in bmp085GetPressure(...)
71 // so ...Temperature(...) must be called before ...Pressure(...)
72
73 long b5;
74
75 // Definition of output control
76
77 const int unit1 = 8;
78 const int unit2 = 9;
79
80
81 void setup(){ // Setup loop
82         Serial.begin(9600);
83         Wire.begin();
84
85         pinMode (unit1, OUTPUT); // set pin 8 control for sensor 1
86         pinMode (unit2, OUTPUT); // set pin 9 control for sensor 2
87         digitalWrite( unit1, LOW); // set both units off line
88         digitalWrite( unit2, LOW);
89
90         //----------------Calibration FOR ALPHA 2 ------------------
91
92         //-- ALPHA 2 Right Wing Flight Test Calibration Curve
93          //-- Linear from DAB 5-26/27-2015 Alpha = A*(Pfwd/P45) + B
94
95         A = -16.908083; // These values must be adjusted for individual
96         B = 42.415008; // probes and probe locations
97
98         pfwdnoload = 8162.9; //counts Adjust these values for
99         p45noload = 8186.6; //counts the individual sensors
100
```

```
101       //-------NOTE THE BMP085 IS NOT ACTUALLY NEEDED----------
102       //-------THE SENSOR CAN BE REMOVED FROM THE DFRDAS-----------
103       //-------ALONG WITH THE ASSOCIATED CODE----------------------
104
105       bmp085Calibration();
106       pinMode(led13, OUTPUT);
107 } // end setup loop
108
109 void loop() // Main loop
110 {
111       float temperature = bmp085GetTemperature(bmp085ReadUT()); //MUST be called first
112       float pressure = bmp085GetPressure(bmp085ReadUP());
113       float atm = pressure / 101325; // "Standard Atmosphere Sea Level Pressure"
114       float altitude = calcAltitude(pressure); // Uncompensated calculation - in Meters
115
116       // Various alternative possibilities for output from the BMP085
117
118       // Serial.print("Barometric Pressure = ");
119       pressurepsi = pressure * 0.000145037738; // convert from Pa to psi
120       altitudefeet = altitude * 3.280839895; // convert altitude from meters to feet
121       // Serial.print(pressurepsi, 6);
122       // Serial.println("psi");
123
124       // Serial.print("Barometric Pressure = ");
125       // pressurepsi = pressure * 0.000295; // convert from Pa to inHg
126       // Serial.print(pressurepsi,6);
127       // Serial.println(" inHg");
128
129       // Serial.print("Altitude = ");
130       // altitude = altitude * 3.2808; // convert from Pa to inHg
131       // Serial.print(altitude,2);
132       // Serial.println(" feet");
133       // ---------------------------------------------------------------------------
134       // Serial.print(pressurepsi);
135
136       Serial.print(altitudefeet,2);
137       Serial.print(",");
138
139       if ( num1 > 5 ) // Discard initil 5 inputs for stability
140       {
141                 led =-led;
142                 num1 =0;
143
144                 // Multiplex the two MS4525 pressure sensors
145
146                 if (led < 0)
147                 {
148                           digitalWrite(led13,HIGH);
149                 }
150                 else
151                 {
152                           digitalWrite(led13,LOW);
153                 }
154
155       }
156
```

```
157     num1 =num1+1;
158
159     //-------------------------------------------------
160     // Get Differential Pressure from unit 1
161
162     digitalWrite(unit1,HIGH );
163     unit=1;
164     float pfwd = MS4525Getpressure(unit); // Get Differential Pressure from unit 1
165     digitalWrite( unit1, LOW);
166
167     //pfwd =7814.83; // TEST ==========================
168
169     Serial.print( pfwd); // Print raw counts
170     Serial.print(",");
171
172     pfwdcorr = pfwd - pfwdnoload; // Account for no load
173
174     // Serial.print( pfwdcorr, 6); // Debuggign
175     // Serial.print(" , ");
176
177
178     //-------------------------------------------------
179     // Get Differential Pressure from unit 2
180     digitalWrite(unit2,HIGH );
181
182     unit=2;
183     float p45 = MS4525Getpressure(unit); // Get Differential Pressure from unit 2
184     digitalWrite( unit2, LOW);
185
186     //p45 =7926.78; // TEST============================
187
188     Serial.print( p45); // Print raw counts
189     Serial.print(",");
190
191     p45corr = p45 - p45noload; // Account for noload
192
193     // Serial.print( p45corr,6); // Debugging
194     // Serial.print(" , ");
195
196     digitalWrite(unit2,LOW);
197
198     Serial.flush(); // Clear serial port
199      // get values again.
200
201     // pfwdcorr=1; // TEST==============================
202     // p45corr=-2; // TEST==============================
203
204
205     pfwd_p45 = pfwdcorr/p45corr;
206
207     // Serial.print(pfwd_p45,10);
208     // Serial.print(" ------, ");
209
210     //----------------TEST-----------------------------
211     // pfwd_p45 = 2.1;
212     //----------------END TEST--------------------------
```

```
213
214       Serial.print(pfwd_p45,5);
215       Serial.print(" , ");
216
217       //----- Calculate Alpha From Pfwd/P45 ----------
218
219       Alpha = A*(pfwd_p45) + B;
220
221       Serial.print(Alpha);
222       Serial.print(" , ");
223
224       Serial.print(pfwdnoload);
225
226       Serial.print(" , ");
227       Serial.print(p45noload);
228
229       Serial.print(" , V=");
230       Serial.println(ver);
231
232       // delay(1000); // Debugging
233       // Serial.print("\n");
234
235
236 } // End of main loop
237
238 // Stores all of the bmp085's calibration values into global variables
239 // Calibration values are required to calculate temp and pressure
240 // This function should be called at the beginning of the program
241
242 void bmp085Calibration()
243 {
244       ac1 = bmp085ReadInt(0xAA);
245       ac2 = bmp085ReadInt(0xAC);
246       ac3 = bmp085ReadInt(0xAE);
247       ac4 = bmp085ReadInt(0xB0);
248       ac5 = bmp085ReadInt(0xB2);
249       ac6 = bmp085ReadInt(0xB4);
250       b1 = bmp085ReadInt(0xB6);
251       b2 = bmp085ReadInt(0xB8);
252       mb = bmp085ReadInt(0xBA);
253       mc = bmp085ReadInt(0xBC);
254       md = bmp085ReadInt(0xBE);
255 }
256
257 // Calculate temperature in deg C
258
259 float bmp085GetTemperature(unsigned int ut){
260       long x1, x2;
261
262       x1 = (((long)ut - (long)ac6)*(long)ac5) >> 15;
263       x2 = ((long)mc << 11)/(x1 + md);
264       b5 = x1 + x2;
265
266       float temp = ((b5 + 8)>>4);
267       temp = temp /10;
268
```

```
269       return temp;
270 }
271
272 // Calculate pressure retrieved.
273 // Calibration values must be known.
274 // b5 is also required so bmp085GetTemperature(...) must be called first.
275 // Value returned is pressure in units of Pa.
276
277 long bmp085GetPressure(unsigned long up){
278       long x1, x2, x3, b3, b6, p;
279       unsigned long b4, b7;
280
281       b6 = b5 - 4000;
282
283       // Calculate B3
284       x1 = (b2 * (b6 * b6)>>12)>>11;
285       x2 = (ac2 * b6)>>11;
286       x3 = x1 + x2;
287       b3 = (((((long)ac1)*4 + x3)<<OSS) + 2)>>2;
288
289       // Calculate B4
290       x1 = (ac3 * b6)>>13;
291       x2 = (b1 * ((b6 * b6)>>12))>>16;
292       x3 = ((x1 + x2) + 2)>>2;
293       b4 = (ac4 * (unsigned long)(x3 + 32768))>>15;
294
295       b7 = ((unsigned long)(up - b3) * (50000>>OSS));
296       if (b7 < 0x80000000)
297       p = (b7<<1)/b4;
298       else
299       p = (b7/b4)<<1;
300
301       x1 = (p>>8) * (p>>8);
302       x1 = (x1 * 3038)>>16;
303       x2 = (-7357 * p)>>16;
304       p += (x1 + x2 + 3791)>>4;
305
306       long temp = p;
307       return temp;
308 }
309
310 // Read 1 byte from the BMP085 at 'address'
311
312 char bmp085Read(unsigned char address)
313 {
314       unsigned char data;
315
316       Wire.beginTransmission(BMP085_ADDRESS);
317       Wire.write(address);
318       Wire.endTransmission();
319
320       Wire.requestFrom(BMP085_ADDRESS, 1);
321       while(!Wire.available())
322       ;
323
324       return Wire.read();
```

```
325 }
326
327 // Read 2 bytes from the BMP085
328 // First byte will be from 'address'
329 // Second byte will be from 'address'+1
330
331 int bmp085ReadInt(unsigned char address)
332 {
333     unsigned char msb, lsb;
334
335     Wire.beginTransmission(BMP085_ADDRESS);
336     Wire.write(address);
337     Wire.endTransmission();
338
339     Wire.requestFrom(BMP085_ADDRESS, 2);
340     while(Wire.available()<2)
341     ;
342     msb = Wire.read();
343     lsb = Wire.read();
344
345     return (int) msb<<8 | lsb;
346 }
347
348 // Read the uncompensated temperature value
349
350 unsigned int bmp085ReadUT(){
351     unsigned int ut;
352
353     // Write 0x2E into Register 0xF4
354     // This requests a temperature reading
355     Wire.beginTransmission(BMP085_ADDRESS);
356     Wire.write(0xF4);
357     Wire.write(0x2E);
358     Wire.endTransmission();
359
360     // Wait at least 4.5ms
361     delay(5); // Wait 5 ms
362
363     // Read two bytes from registers 0xF6 and 0xF7
364     ut = bmp085ReadInt(0xF6);
365
366     return ut;
367 }
368
369 // Read the uncompensated pressure value
370
371 unsigned long bmp085ReadUP(){
372
373     unsigned char msb, lsb, xlsb;
374     unsigned long up = 0;
375
376     // Write 0x34+(OSS<<6) into register 0xF4
377     // Request a pressure reading w/ oversampling setting
378     Wire.beginTransmission(BMP085_ADDRESS);
379     Wire.write(0xF4);
380     Wire.write(0x34 + (OSS<<6));
```

```
381       Wire.endTransmission();
382
383       // Wait for conversion, delay time dependent on OSS
384       delay(2 + (3<<OSS));
385
386       // Read register 0xF6 (MSB), 0xF7 (LSB), and 0xF8 (XLSB)
387       msb = bmp085Read(0xF6);
388       lsb = bmp085Read(0xF7);
389       xlsb = bmp085Read(0xF8);
390
391       up = (((unsigned long) msb << 16) | ((unsigned long) lsb << 8) | (unsigned long) xlsb) >> (8-OSS);
392       //Serial.print(up);
393       //Serial.print(" , ");
394       return up;
395 }
396
397 void writeRegister(int deviceAddress, byte address, byte val) {
398       Wire.beginTransmission(deviceAddress); // start transmission to device
399       Wire.write(address); // send register address
400       Wire.write(val); // send value to write
401       Wire.endTransmission(); // end transmission
402 }
403
404 int readRegister(int deviceAddress, byte address){
405
406       int v;
407       Wire.beginTransmission(deviceAddress);
408       Wire.write(address); // register to read
409       Wire.endTransmission();
410
411       Wire.requestFrom(deviceAddress, 1); // read a byte
412
413       while(!Wire.available()) {
414                 // waiting
415       }
416
417       v = Wire.read();
418       return v;
419 }
420
421 float calcAltitude(float pressure){
422
423       float A = pressure/101325;
424       float B = 1/5.25588;
425       float C = pow(A,B);
426       C = 1 - C;
427       C = C /0.0000225577;
428
429       return C;
430 }
431
432 // Get Delta Pressure from MS4525 ----------------------------------------
433
434 //Reads Differential Pressure from I2C Ms4525 sensor
435 //
436 float MS4525Getpressure(int unit){
```

```
437     deltapressure =0;
438
439     //Send a request
440     //Start talking to the device at the specified address
441     Wire.beginTransmission(press_address);
442     //Send a bit asking for register zero, the data register
443     Wire.write(0);
444     //Complete Transmission
445     Wire.endTransmission();
446
447     //Request 2 Byte from the specified address
448     Wire.requestFrom(press_address, 2);
449     //wait for response for 2 bytes
450
451     if(2 <=Wire.available())
452     {
453             reading = Wire.read(); // byte 1
454             //Status = reading & maskstatus; // check status
455             //Status = Status >>6;
456             //Serial.println(Status);
457
458             //if ( Status <= 0)
459             //{
460             reading = reading & mask;
461
462             reading = reading << 8; //
463
464             reading |= Wire.read(); // read byte 2
465             //Serial.print(reading);
466             //Serial.print(",");
467             deltapressure =reading;
468             //deltapressure = deltapressure/16383 - .5;
469
470             // Serial.println(pressure,4);
471             // }
472     }
473     //delay(50);
474     return(deltapressure);
475
```

APPENDIX B—MECHANICAL DRAWINGS, GENERAL ASSEMBLY, GROUND AND FLIGHT TESTING

The following pages contain mechanical drawings for the right wing-tip air data boom. This installation is intended for the Cessna 182-N721A. The drawings represent the three boom sections, three mounting blocks, three boom straps, and three L brackets shown in figure B-1. The L brackets are attached to the right wing-tip rib using rivets, per AC 43.13-2B.

The blocks attach to the L brackets through the aircraft's skin. The top of each block has a nut plate installed over each of the four block holes. Blocks are fastened to the nut plates with AN3 bolts. Straps are fastened to blocks with 10–32″ x 2 3/4″ bolts and associated hardware. The two most aft boom tubes are constrained with one 10–32″ x 2 3/4″ bolt and associated hardware, as shown in figures B-2–B-5. The two swivel head boom segments and middle boom tube are constrained with one 10″–32″ x 2 1/4″ bolt and associated hardware, as shown in figures B-6–B-8.

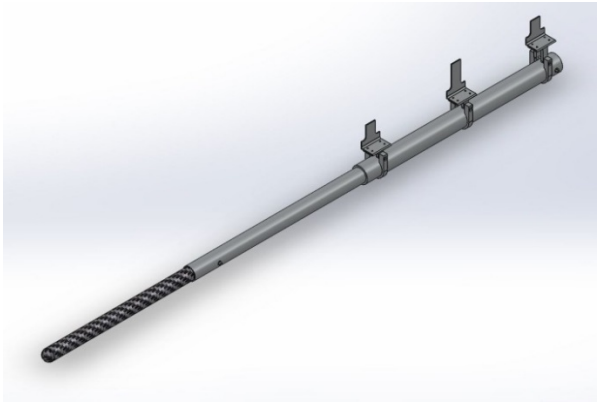

Figure B-1. Isometric view

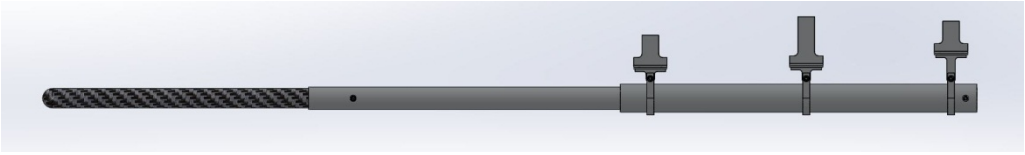

Figure B-2. Side view

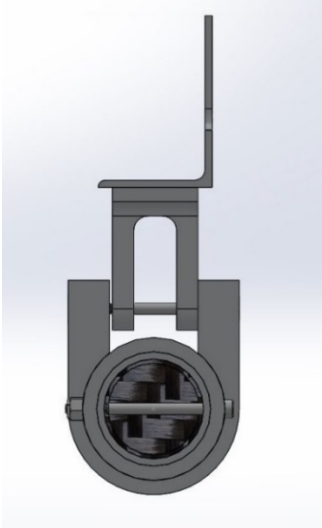

Figure B-3. Front view

Figure B-4. Top view

Figure B-5. Right wing tip with boom (side view)

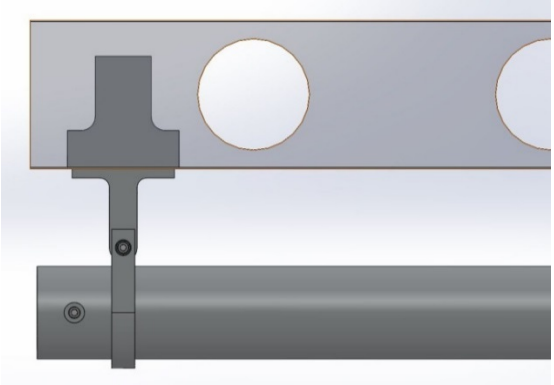

Figure B-6. Right wing tip (side view)

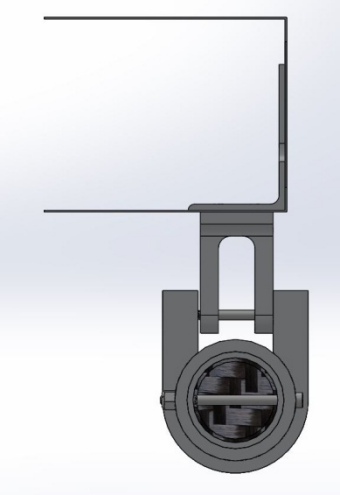

Figure B-7. Right wing tip with boom (view looking forward)

Figure B-8. Angle of attack data boom

STRUCTURAL ANALYSIS OVERVIEW

Flight test booms are exposed to various loads during in-flight operations. The purpose of this test is to physically test the boom structural behavior on the ground. The boom is designed to withstand an in-flight load of 4.4 G. Details of the design and analysis are not included in this report.

The boom, shown in figure B-8, is modeled with a swivel head at the tip, which weighs approximately 1 lb., and four sections with different distributed loads. The first section, starting at the tip, is made of carbon fiber, the second section consists of aluminum and carbon fiber, and the remaining sections are made of aluminum. Note that sections are superimposed; this has been considered in the analysis. The boom is attached to the wing with three hinges. Inside the wing, brackets, stiffeners, and shims are used to strengthen the outboard wing rib and skin. In figure B-9, the distributed loads for each section are shown, as is as the point load because of the tip probe. The point and distributed loads represent a 4.4 G of in-flight load. The assumptions for the finite element analysis (FEA) are shown at the top right of figure B-9.

Ground tests used point loads representative of the resultant forces to reproduce the shear and bending moment diagram shown in figures B-10 and B-11. All point loads were rounded up to the closest available weight. The theoretical and actual loads are described in figure B-12. Note that the actual loads are the ones in parentheses (all loads were conservative).

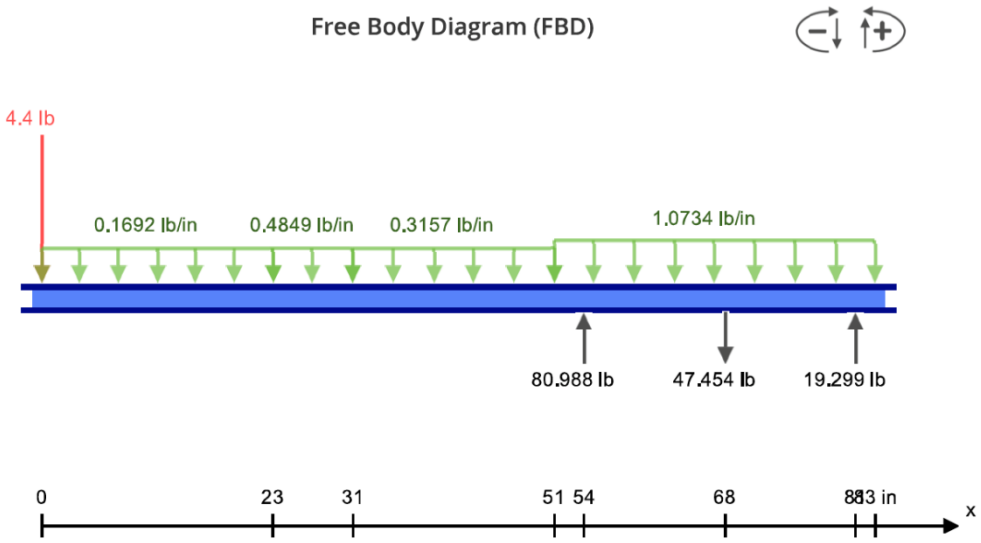

Figure B-9. Data boom free body diagram

A shear force and bending moment diagram was created. The highest shear force is located at point 5 in figure B-11, with a magnitude of 59.283 lb. As expected, the highest shear force is located at the forward attachment point. The maximum bending moment occurs at point 4 in figure B-12, which is consistent with the location of the maximum shear force. The magnitude of the maximum bending moment is -594.64 lb.-in.

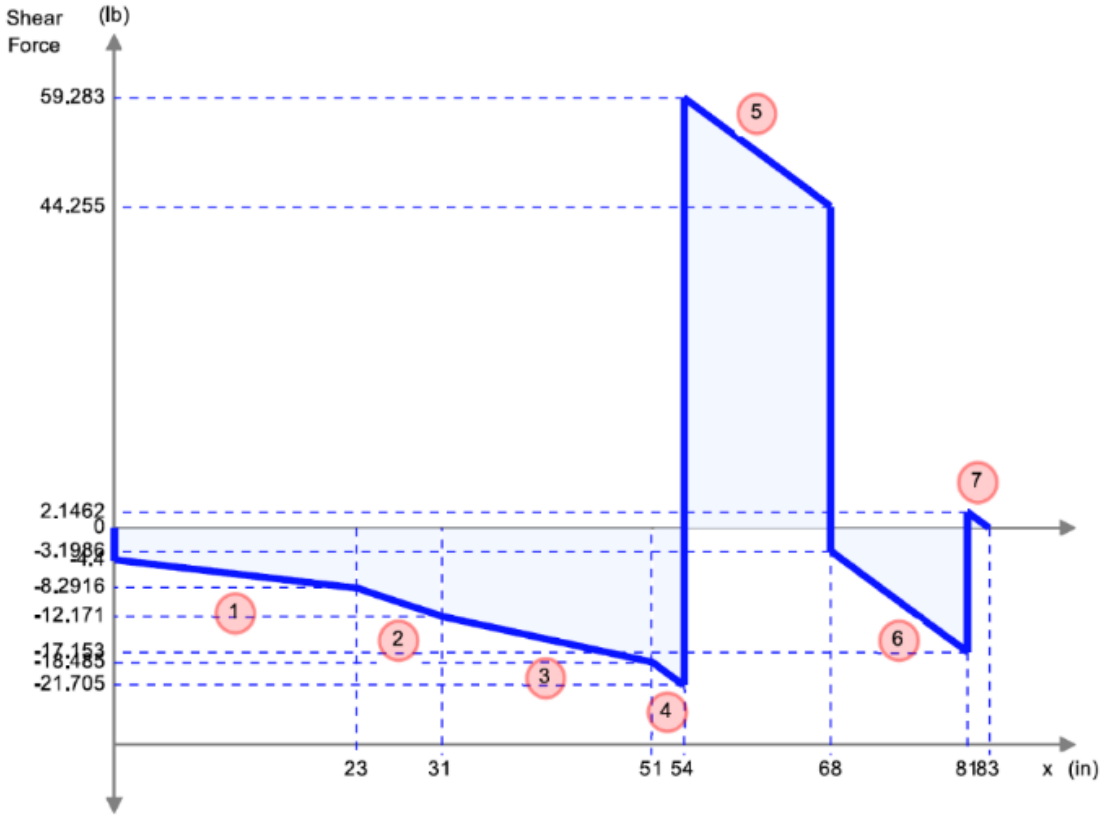

Figure B-10. Shear force diagram

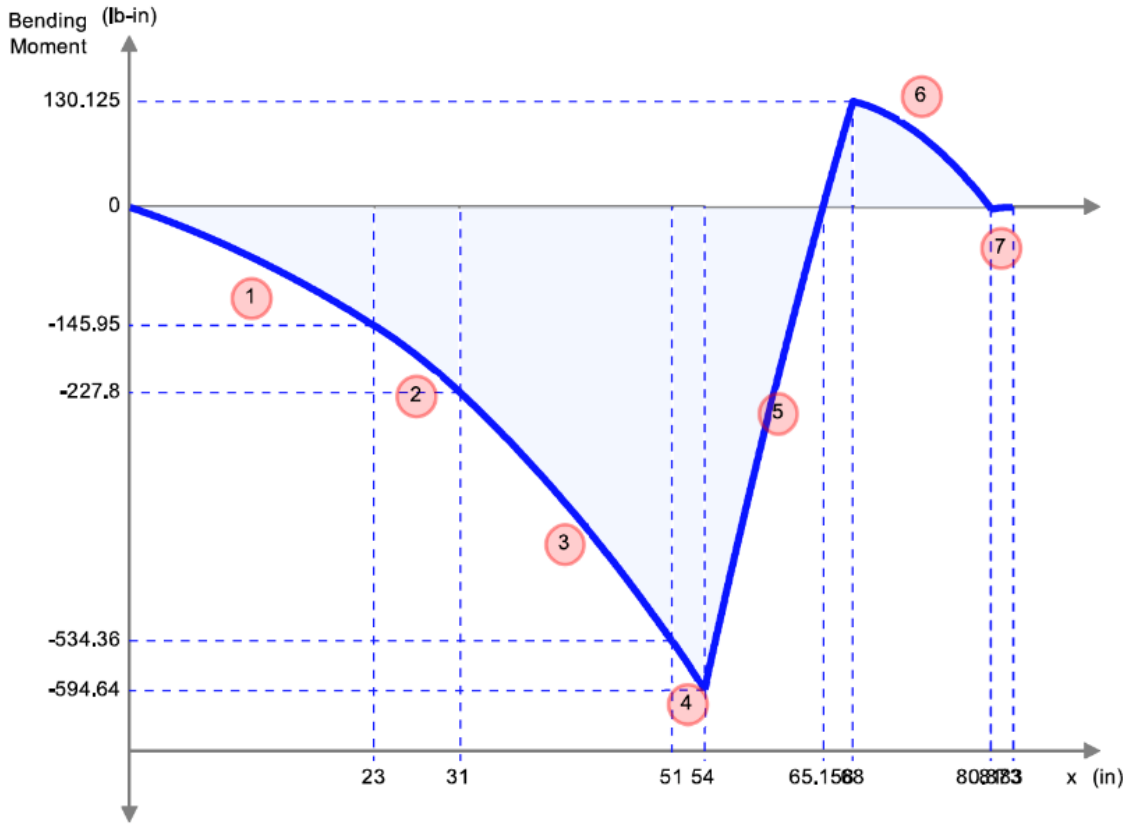

Figure B-11. Bending moment diagram

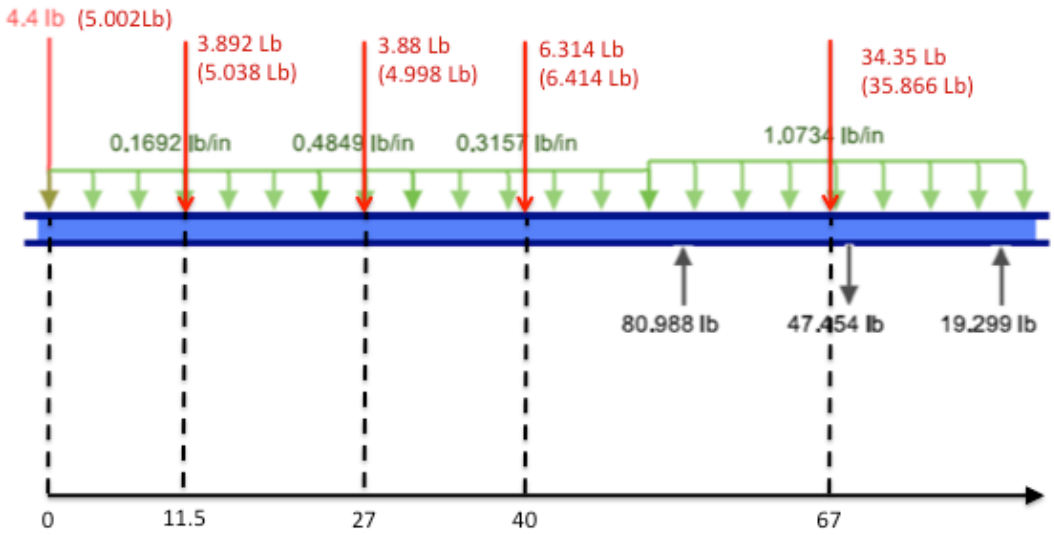

Figure B-12. Point loads magnitude and position

Based on available weights, the expected deflection of the beam was 0.219″ at the tip, as shown in figure B-13. The actual maximum shear and bending moment located at the forward attachment of the boom-versus-wing deflection at all three connections were negligible.

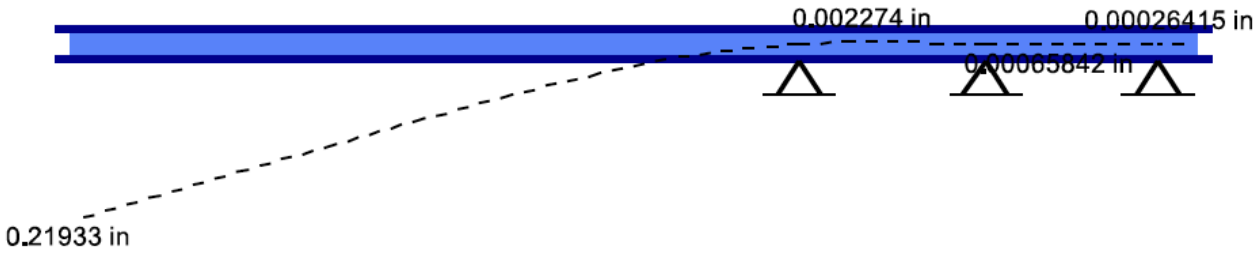

Figure B-13. Predicted deflection

TEST SETUP

With the boom mounted on the right wing, point loads were placed as shown in figure B-14. Two scissor car jacks were used to support the base holding the weights. Two rulers were vertically aligned, with respect to the boom, and attached to a white board in the background. One ruler was used for tip deflection, the other for root deflection. Two cameras were positioned using a level to align the edge of the boom with the rulers. Extra measurements were made at the leading and trailing edges. In addition, the deflection angle was measured with an inclinometer at different stations, denoted with blue tape in figure B-15.

Figure B-14. Test setup with boom unloaded

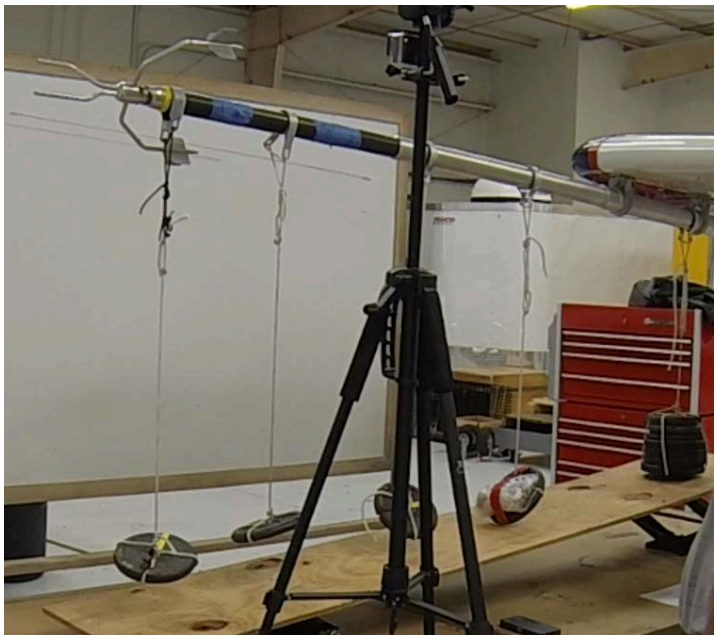

Figure B-15. Test setup—boom loaded

POINT LOADS HARDWARE

The setup is shown in figure B-16. The clamps shown in figure B-17 were covered with rubber to avoid scratching the boom. Each of the point loads were weighed and identified with colored tape (yellow = 5 lb., red = 6.414 lb., no color = 35 lb.). Weights were arranged according to figure B-18 to ensure each weight was attached at the right location.

Figure B-16. Rulers, clamps, and inclinometer stations setup

Figure B-17. Clamps

Figure B-18. Weights with the correspondent clamp

PROCEDURE

At setup completion, the leading and trailing edges and the inclination at each marked station were measured. Next, loads were slowly applied by lowering the base jacks progressively from root to tip using the car jacks. During the process, deformation was monitored while checking for abnormal noises. Knock-it-off test limits were a tip deflection of 1″. All ground test personnel had knock-it-off authority. Once all weights cleared the base, the loading was maintained for one minute. Measurements of deflection and displacement were taken again. The boom was then unloaded, detached, and inspected.

RESULTS

Table B-1 shows the results of the measurements before and after the 1-minute constant load. The total deflection at the tip, using the superposition method, was 0.741″, which approximates the measurement from the ruler located at the tip, as shown in figure B-16. However, while the boom was loaded, it experienced a rotation, which set the tip 0.203″ lower. In addition, the wing experienced a displacement of 0.25″, which resulted in 0.288″ of actual deflection at tip.

Table B-1. Deflection and displacement

Inclination [deg.]								Leading Edge	Trailing Edge
Unloaded	0.1	0.1	0.1	0.1		0.2	0.2	41 3/4	40
Loaded	0.1	0.2	0.4	0.5		0.8	0.8	41 1/2	39 3/4
Location (root to tip) [in.]	8.38	22.3	37.38	49.8	66	76.8	83.00	1/4	1/4
Unloaded deflection	0.015	0.039	0.065	0.087		0.181	0.203		
Loaded deflection	0.015	0.063	0.169	0.277		0.654	0.741		
Rotation	0.000	0.024	0.103	0.190		0.473	0.538		
				Experimental			0.288		
				Expected			0.219		
				% ERROR			31.50		

From the FEA, the expected deflection was 0.219″ at the tip, which represents a 31.5% calculation error. The limit for the test was set to 1″ deflection, leaving the resulting value within the acceptable range. The difference between the actual load (available hardware) and the true load varied from 1.5%–29.4%. This results in a more conservative test because in-flight loads are not expected to be greater than 4.4 G.

As the boom was unloaded, the tip returned to its initial position (see figure B-19).

During the post-test inspection, all brackets, fasteners, and rivets, and the boom itself, were checked. There were no signs of cracks, fatigue, or deformation in any of the inspected elements.

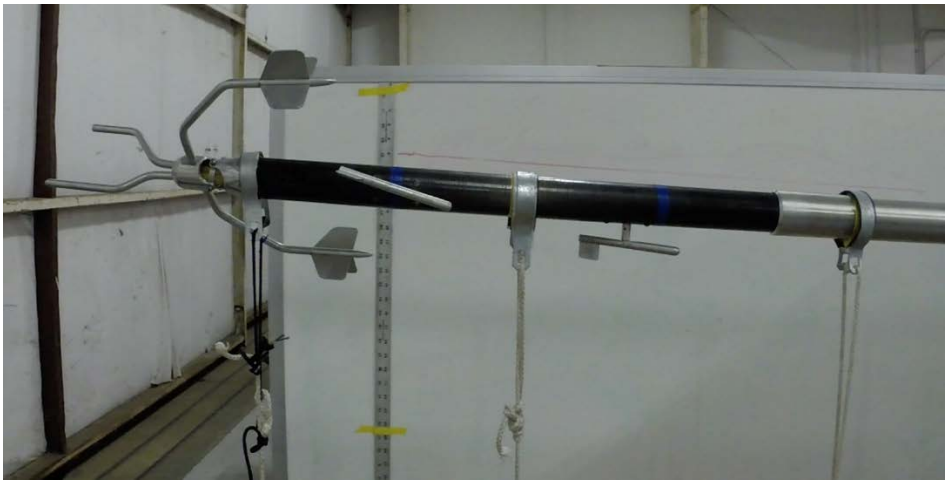

Figure B-19. Boom–tip deflection

DATA ACQUISITION AND INSTRUMENTATION

The aircraft's data acquisition system (DAS) collects data from the inertial measurement unit (IMU), global position system (GPS) unit, total and static pressure transducers, and angle of attack (AoA) and angle of sideslip control position transducers (CPT). The IMU installed in the flight test aircraft is the Honeywell HG1700. The IMU is able to record the aircraft's velocity relative to the ground, all pitch, roll, yaw rates, and angles, and any accelerations acting on the aircraft. For position reporting, the IMU communicates with the ProPak-V3 GPS unit manufactured by NovAtel.

The aircraft is equipped with a precision differential pressure transducer and precision static pressure transducer (PPT), used to measure total pressure and static pressure, respectively. These PPTs, manufactured by Honeywell, transform changes in pressure measured at the air data boom into a digital signal that is recorded by the DAS. Additionally, the air data boom has an AoA vane and angle of sideslip vane that are attached to separate potentiometers. These potentiometers, also known as CPT, send angle of sideslip and AoA measurements to the DAS via changes in signal voltage. Similar to the PPT, the CPT require calibration before they can be implemented.

Once these systems were installed on the aircraft, an initial ground calibration was completed. The boom pitot and static ports were connected to a ground pitot-static tester and the system was tested for airspeeds between 38 and 159 knots and pressure altitudes between -100' and 9985'. Furthermore, the angle of sideslip and AoA vanes were both tested between -90º and 90º. The resulting conversion equations are given here for airspeed, pressure altitude, AoA, and angle of sideslip, respectively. It is important to note that the boom's pitot-static system was tested and verified to be leak free, and any inherent instrument error is negligible for the purposes of the subsequent analysis.

$$V_i = 206.28 \times {q_{ci}}^{0.5203}$$
$$H_i = -2158.7 \times P_s + 31552$$
$$\propto_i = -0.00281 \times v_{\propto} + 0.53235$$
$$\beta_i = -0.00295 \times v_{\beta} + 0.53892$$

The outside air temperature (OAT) and fuel quantities were manually entered into the DAS control panel on the flight test engineers' (FTE) laptop throughout flight. The fuel remaining quantities entered by the FTE were obtained from a J.P. Instruments Fuel Scan 450 fuel monitoring system, which reports fuel flow, fuel used, and fuel remaining, and was part of the extra instrumentation that was installed previously on the aircraft. This system was tested and calibrated through a functional check flight prior to its use for subsequent flight testing. Next, the OAT was read directly off of the temperature gauge on the aircraft's Aspen Evolution 1000 primary flight display.

The IMU, GPS, PPT, and CPT signals were interpreted by a National Instruments CompactRIO (Reconfigurable Input/Output) communications module. The CompactRIO simultaneously logged this data in a raw format and output the data to an FTE laptop. The laptop served as both a master control module for the DAS system as well as a data-processing and -logging device. The laptop saved the processed data into a comma-separated value file that was then reduced and interpreted post-flight.

Table B-2 and figure B-20 represent the sensor locations and type of data (analog/digital) used in this research.

Table B-2. Cessna 182Q instrumentation

1	Angle of Sideslip Probe
2	Angle of Sideslip Sensor I/F Module P/N DSTR-ANGLE OF SIDESLIP-1975
3	Pitot Tube
4	Display I/F Module P/N DSTR-Angle of Sideslip-9525DDUAL
5	Port – Eagle Display/Starboard – Hawk Display
6	SMART Pressurized I/F Module P/N DSTR-Angle of Sideslip-XXXX
7	Angle of Sideslip System audio output
8	Angle of Sideslip Sensor I/F Module P/N DSTR-ANGLE OF SIDESLIP-1975
9	Angle of Sideslip Probe
10	Angle of Sideslip Vane
11	Angle of Sideslip Vane
12	Honeywell Precision Differential Pressure Transducer
13	Honeywell Precision Static Pressure Transducer
14	Static Pressure Source

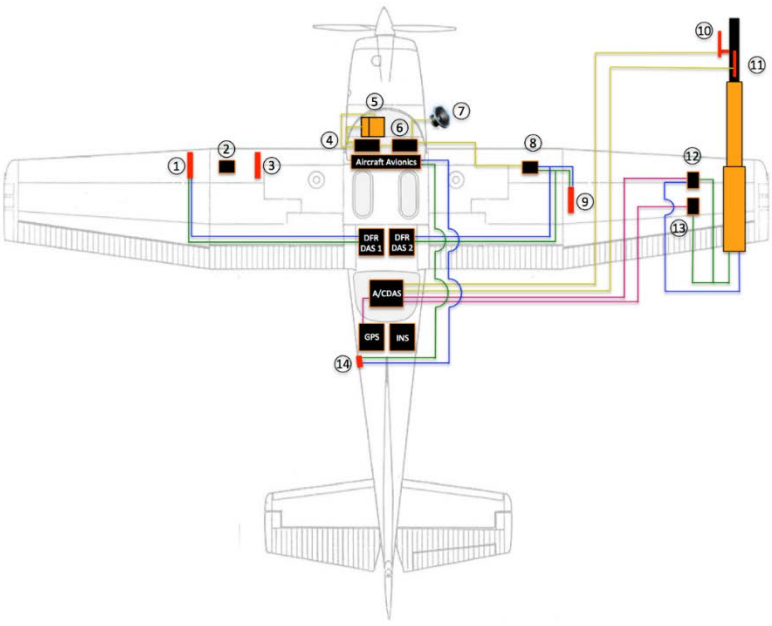

Figure B-20. Air data boom pneumatic and digital wiring

GROUND CALIBRATION

The following static pressure calibration illustrates the ground calibration procedure (See table B-3 and figure B-21). Additional calibrations (not shown) were accomplished for dynamic pressure, AoA, and angle of sideslip.

PPT (static pressure)

- Altitudes were commanded from the calibration unit at the Embry-Riddle Aeronautical University (ERAU) maintenance center.
- Altitude was increased in 1000' increments from 0'–10,000' and back to 0.
- Pressure outputs were recorded from the PPT measuring static pressure.
- Commanded altitude values were read from the calibration unit and corrected according to the calibration sheet.

Table B-3. Commanded altitude vs. measured pressure

Commanded Alt. [ft.]	Static Pressure [psi]
-100	14.752
1045	14.152
1980	13.684
2990	13.188
4035	12.684
6049	11.79
6965	11.359
7960	10.944
8962.5	10.522
9985	10.113
8952.5	10.516
8000	10.914
6885	11.386
6010	11.774
5002.5	12.23
4005	12.695
3010	13.173
2010	13.666
1015	14.176
-100	14.757

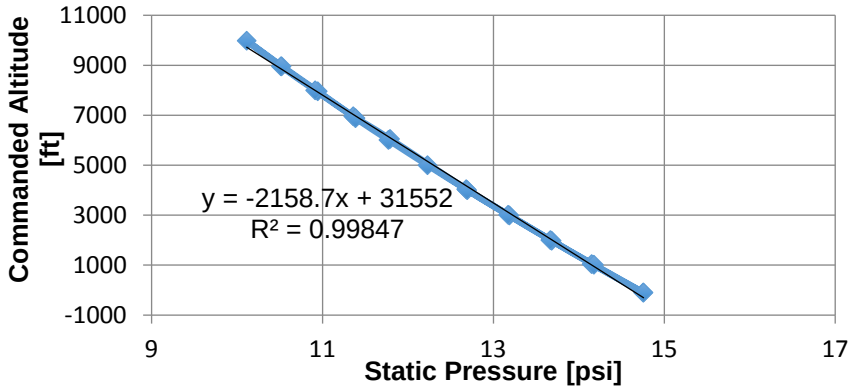

Figure B-21. Commanded altitude vs. static pressure

INFLIGHT CALIBRATION THEORY

Air Data System Calibration

In flight tests, air data sensors are commonly placed at the end of a boom to collect air data not affected by the aircraft. Although air data booms alleviate errors associated with this flow field disturbance, it is impossible to place the sensors in completely undisturbed air because the boom would need to be longer than feasible to retain rigidity in flight.

In this flight-test technique, pressure position error correction (ΔP_{PC}), airspeed static pressure position error correction (ΔV_{PC}), and static altitude pressure error correction (ΔH_{PC}) are calculated. Plots are created to show how these correction factors change with airspeed. These plots and correction factors are used in subsequent flights to obtain corrected airspeeds and altitudes.

Airspeed Correction

To determine the airspeed correction factor, several quantities must be computed. The first is the airspeed static pressure position error correction (ΔV_{PC}), which is the difference between calibrated and indicated airspeeds. The relationship can be mathematically represented as follows:

$$V_i = V_C - \Delta V_{PC} \tag{B-1}$$

where V_C is calibrated airspeed, V_i is indicated airspeed, and ΔV_{PC} is the correction factor.

Because the data for the Air Data System (ADS) calibration were recorded over approximately 2 hours, the change in aircraft weight due to fuel consumption must be considered. This was done

by standardizing the test results with a given reference weight. The following equation computes weight-corrected velocity:

$$V_{i,w} = \sqrt{\frac{W_{ref}}{W_{test}}} \tag{B-2}$$

where $V_{i,w}$ is weight-corrected indicated airspeed, W_{ref} is maximum gross aircraft weight, and W_{test} is gross aircraft weight less fuel used.

At Mach numbers below 0.3, compressibility effects can be ignored. Under these conditions, TAS and EAS (V_E) are assumed equal. The relationship between equivalent and TAS is:

$$V_E = \sqrt{\sigma} \cdot V_T \tag{B-3}$$

where V_T is TAS and σ is density ratio.

Position Correction

The second correction factor is the static pressure position error coefficient. This correction nondimensionalizes the data to compare and graph the results of the ADS calibration. The measured dynamic pressure is:

$$q_{Ci} = P_{SSL}\left(\left(\frac{\rho_{SSL} \cdot {V_{i,w}}^2}{(P_{SSL} \cdot 7)+1}\right)^{\gamma/\gamma-1} - 1\right) \tag{B-4}$$

where q_{Ci} is the measured dynamic pressure.

The static pressure position coefficient is calculated by taking the difference between the two dynamic pressures:

$$\Delta P_{PC} = q_C - q_{Ci} \tag{B-5}$$

Altitude Correction

The last correction factor is the altitude static position error (ΔH_{PC}), which accounts for the altimeter static pressure error. This factor is computed using the hydrostatic equation:

$$\Delta H_{PC} = \frac{\Delta P_{PC}}{\rho g} \tag{B-6}$$

Upwash Calibration

Upwash calibration is used to determine errors in the indicated AoA that result from upwash in the flow field. Upwash decreases ahead of the wing leading edge and, theoretically, if placed far enough forward, upwash is negligible. Theory suggests that this distance is at least 1.5 fuselage diameters ahead of the wing. Completely removing any upwash sensed by the boom would require

an unfeasibly long boom. The upwash correction removes this error and obtains the true AoA, measured with respect to the fuselage reference line (FRL) in-flight.

Because of the way the DAS sensors are installed, other measurement errors need to be accounted for. After reducing data, a correction factor is then determined to calculate the true AoA, which is then compared to other AoA instruments to determine its accuracy.

A direct way of calculating upwash is to compare the indicated AoA to the true AoA, given by:

$$\Delta\alpha = |\alpha_T - \alpha_i| \tag{B-7}$$

where α_{true} is:

$$\alpha_{true} = \theta - \gamma \tag{B-8}$$

and θ is pitch attitude and γ is flight path angle. The flight path angle can be determined from:

$$\gamma = \sin^{-1}\left(\frac{\frac{dh}{dt}}{V_T}\right) \tag{B-9}$$

During straight and level unaccelerated flight, γ is 0. This justifies the assumption that AoA is equal to pitch angle in straight and level unaccelerated flight. The upwash angle is calculated from:

$$\Delta\alpha = \sin^{-1}(n_{xaccel} - n_{xpress}) \tag{B-10}$$

where n_{xaccel} and n_{xpress} are defined, respectively, as:

$$n_{xaccel} = n_{xb}cos\alpha_i - n_{zb}sin\alpha_i \tag{B-11}$$

$$n_{xpress} = \frac{\dot{h}}{V_T} + \frac{\dot{V_T}}{g} \tag{B-12}$$

where n_{xb} is the instrumented body-axis longitudinal load factor, n_{zb} is the instrumented body-axis vertical load factor, $\dot{h}$ is the geometric climb rate from pressure altitude corrected for test day temperature, V_T is the TAS, $\dot{V_T}$ is the rate of change of TAS, g is gravitational acceleration constant, α_i is indicated AoA, and n_{xpress} is used to correct for small vertical velocities or accelerations that are present during steady state trim shots.

IN-FLIGHT CALIBRATION RESULTS

ADS Calibration

Table B-4 contains the POH velocity static pressure position corrections along with the reported indicated airspeed corrections. The aircraft's calibrated airspeed was calculated using the airspeeds in the reduction algorithm. For a graphical representation of these correction factors, refer to figure B-22.

Table B-5 contains correction factors calculated using an ADS calibration reduction algorithm. These values were then used throughout the rest of the algorithm, including upwash calibration and stall testing plots. Individual equations and graphical representations are included in figures B-23, B-24, and B-25.

Table B-4. Velocity corrections as listed in the Pilot's Operating Handbook (POH)

Airspeed	POH Values											
KIAS	50	60	70	80	90	100	110	120	130	140	150	160
KCAS	60	64	71	80	89	99	108	117	127	136	145	155
Aircraft Calculated KCAS	55.4	63.7	72.2	80.7	89.2	97.8	106.5	115.2	124.0	132.9	141.8	150.7
% Error	7.7%	0.4%	1.6%	0.8%	0.2%	1.2%	1.4%	1.5%	2.4%	2.3%	2.2%	2.7%

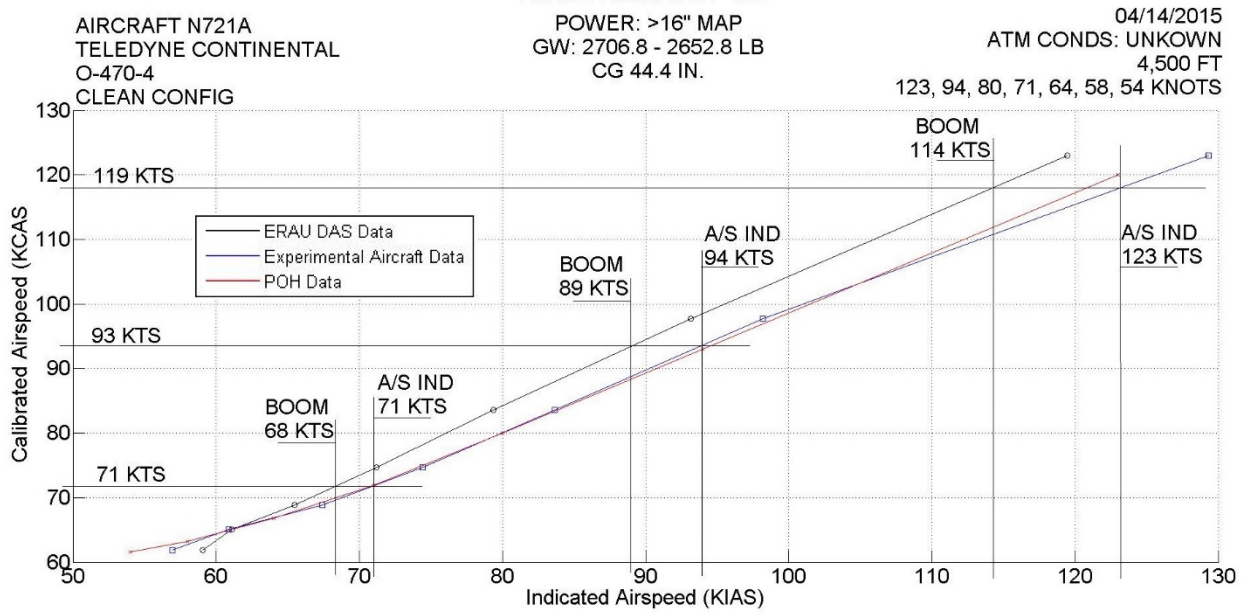

Figure B-22. Values for the POH and ERAU DAS airspeeds in graphical format

Table B-5. Correction values determined during ADS calibration

Viw_DAS	PEC_DAS	dVpc_DAS	dHpc_DAS
KIAS	Unitless	Knots	Feet
119.48	0.06	3.48	41.66
93.17	0.10	4.51	42.50
79.39	0.11	4.22	33.77
71.20	0.10	3.46	24.68
65.48	0.11	3.40	22.34
61.09	0.13	3.95	24.38
59.05	0.10	2.82	16.64

Figure B-22 represents the accuracy of the calculated correction factors. Various horizontal and vertical lines are used to show that, when corrected, both pitot and ERAU DAS indicated airspeeds provide the same calibrated airspeeds. These values fell within +/- 0.5 knots of each other. Figure B-23 shows the results of the ADS calibration on the trimmed DAS data.

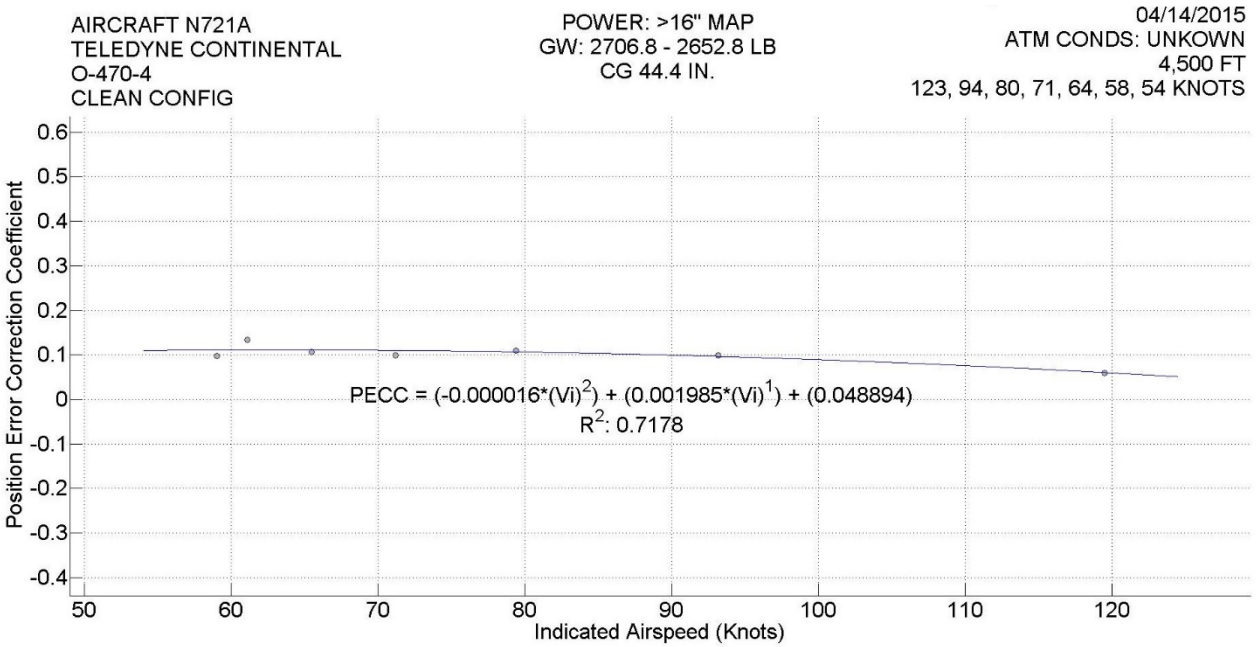

Figure B-23. Static pressure position error (Δ*PPC*) vs. indicated airspeed

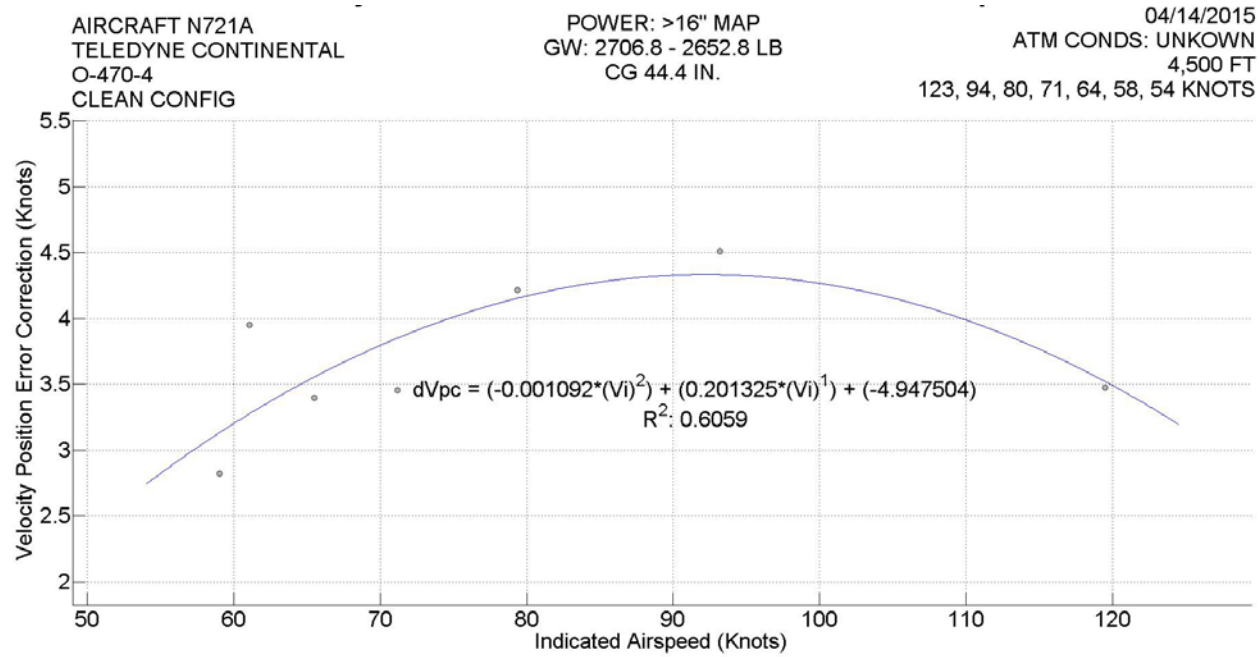

Figure B-24. Velocity static pressure position error (Δ*VPC*) vs. indicated airspeed

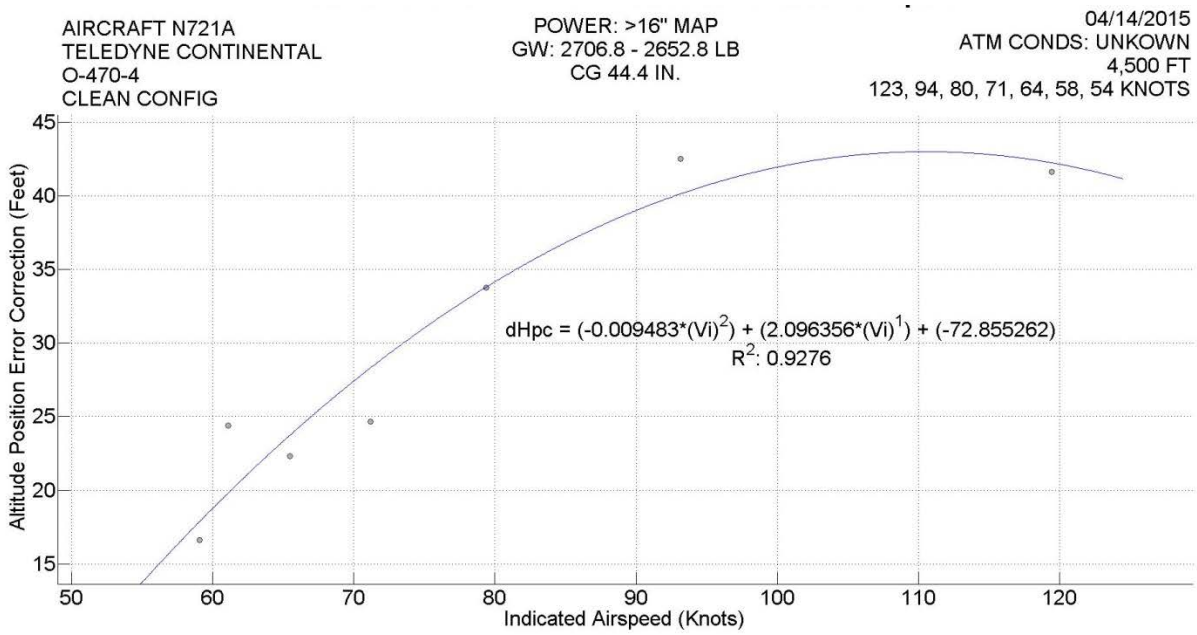

Figure B-25. Altitude static position error vs. indicated airspeed

As the indicated airspeed increases, the error correction remains relatively constant. This shows that the static port is well-placed because the static pressure does not change as the flow field changes. The data point at 61 KIAS is a slight outlier to the trend, caused by failing to maintain test tolerances, a changing air mass composition, or turbulence.

The graph shown in figure B-24 shows how the velocity position error correction changes with indicated airspeed. The best fit line between ΔV_{PC} and indicated airspeed is parabolic. Once again, the 61 KIAS value is an outlier.

Figure B-25 shows a parabolic relationship between altitude position error correction and airspeed. At low speeds, there is a small correction; however, as indicated airspeed increases, a larger correction must be applied.

Upwash Calibration

The following figures were obtained for the upwash calibration. Figure B-25 is a sample figure for $\Delta\alpha$ vs. time, α vs. time, airspeed vs. time, and altitude vs. time for the first leg of the flight test. Figure B-26 shows the $\Delta\alpha$ vs. time for all legs of the flight test, figure B-27 shows $\Delta\alpha$ vs. αi for all legs of the flight test, and figure B-28 shows α_T vs. α_i for all legs of the flight test. Two correction factors were included: 0.4° for α_i and 7.08° for α_T. The correction factor for α_i was due to the air data boom being mounted exactly 0.4° below the FRL. This correction factor was added to α_i. The correction factor for α_T was due to the inertial navigation system mounted at a -7.08° incline. With these correction factors, α_T and α_i are with respect to the FRL.

Two methods are used to calculate upwash. The first method's results can be seen in figure B-25, and the second method can be seen in figure B-26. The first method uses equations B-10–B-12.

Figure B-26 shows the trends of the airspeed, altitude, AoA, and upwash vs. time for the trimmed record data. The *y*-axis for airspeed and altitude are set at the flight test tolerance bands for the trim shots performed. This figure uses the first method of calculating upwash. The second method was used in figure B-27. This takes into account the flight path angle using equations B-7–B-9.

As shown in figure B-26, altitude and airspeed were flown within tolerances. The AoA and upwash measured during trim shots stayed relatively constant.

Figure B-28 shows the upwash correction vs. measured AoA for all 28 trim shots. This upwash was calculated using equations B-10–B-12. This is the first method of calculating upwash. The measured AoA increases as the upwash correction increases. The data is scattered along the line, reflected in the R^2 value.

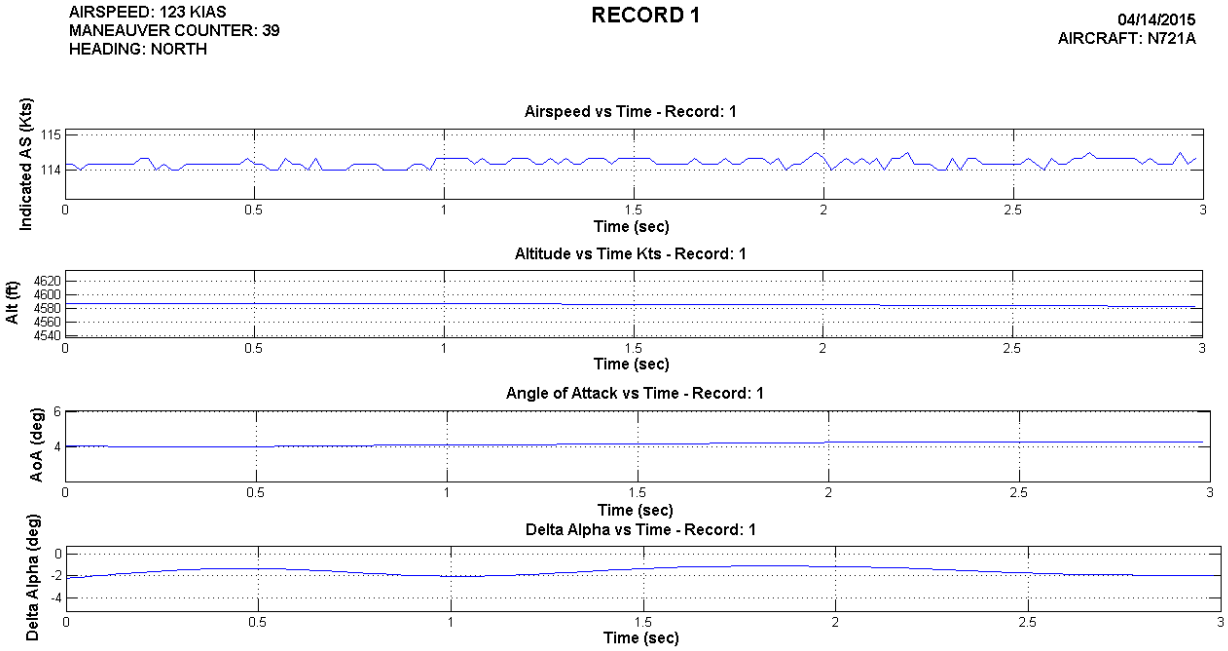

Figure B-26. Δ*α* vs. time, *α* vs. time, airspeed vs. time, and altitude vs. time for record 1

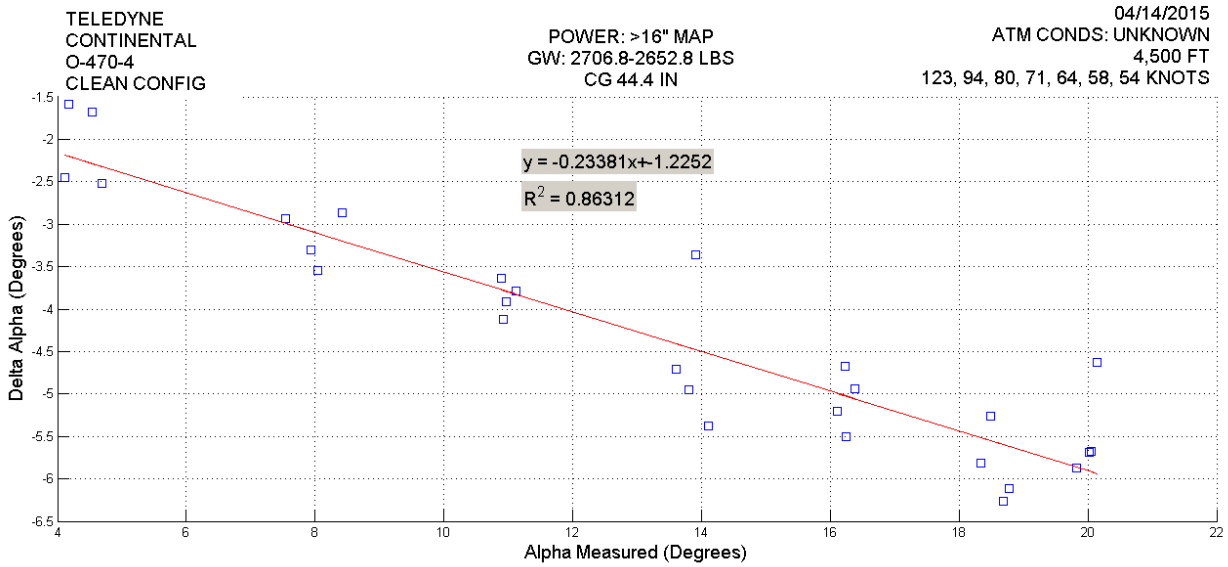

Figure B-27. $\Delta\alpha$ vs. αi for all legs. Alpha measured with respect to the FRL

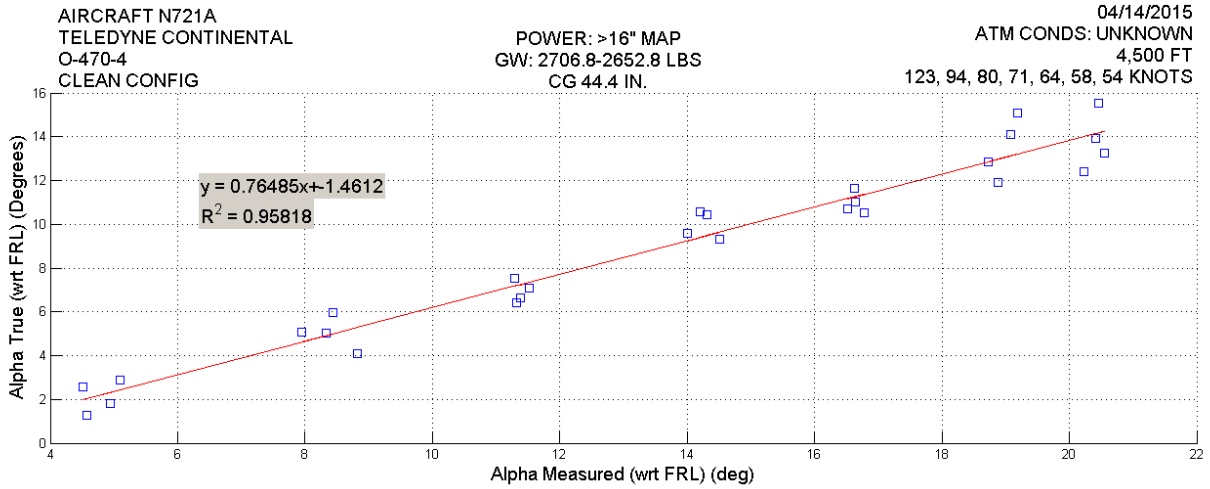

Figure B-28. α_{true} vs. α_i for all legs

Figure B-28 shows that as α_i increases, α_T increases as well. Thus, it can also be said that as α_i increases, upwash also increases.

The upwash results can be validated by comparing figures B-27 and B-28. As shown in equation B-7, a direct way to find the upwash is by calculating the difference between α_T and α_i. The second method to calculate upwash was used to generate figure B-28. In figure B-28, at an α_i of 10°, α_T is 6°. Thus, the upwash for method one is approximately 4°. As shown in figure B-27, at

an α_i of 10°, the upwash can be seen to be approximately 3.5°. This validates the results presented in figures B-27 and B-28 and shows a difference of 13.3%.

STALL TESTING

Data for the analysis of lift behavior at stall were collected during two stall maneuvers performed on April 22, 2015. Figure B-29 show the aerodynamic model for the first stall. The maximum coefficient of lift was found to be 1.42 and occurred at an AoA of 16.5°. Figure B-29 shows the lift coefficient versus. angle attack for the second stall. The maximum coefficient of lift was shown as 1.38 at an AoA of 16°.

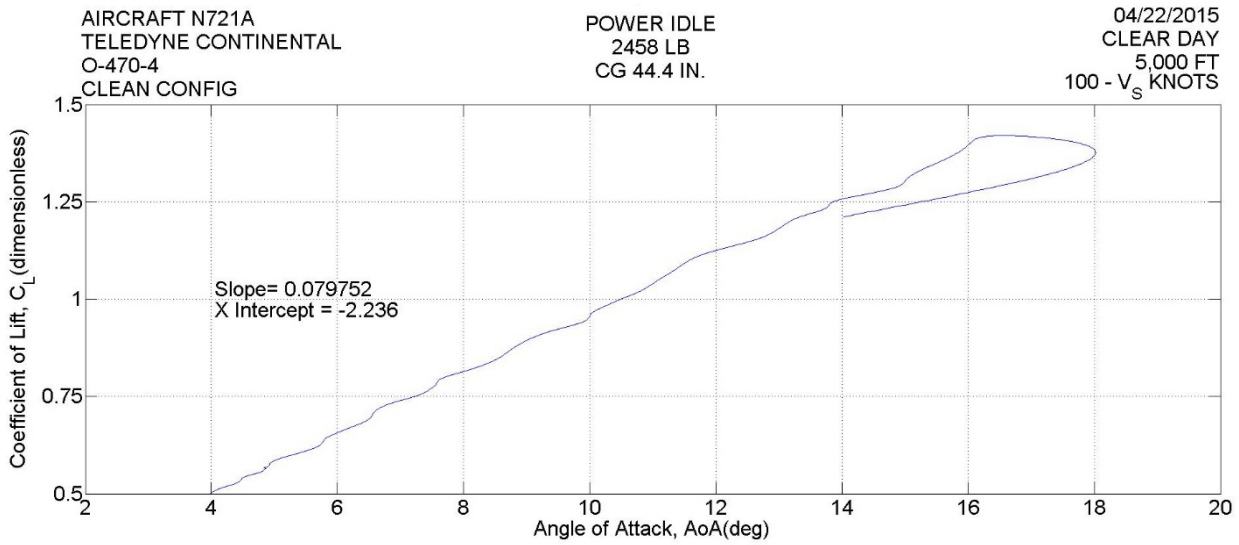

Figure B-29. Stall 1 lift coefficient vs. AoA

Figure B-31 overlays figures B-29 and B-30 to compare Stall 1 and Stall 2. The data show a consistent lift curve slope between both stalls. The difference of the maximum coefficient of lift between both two stalls is 3.15%. For the stall AoA, the difference is 3.08%.

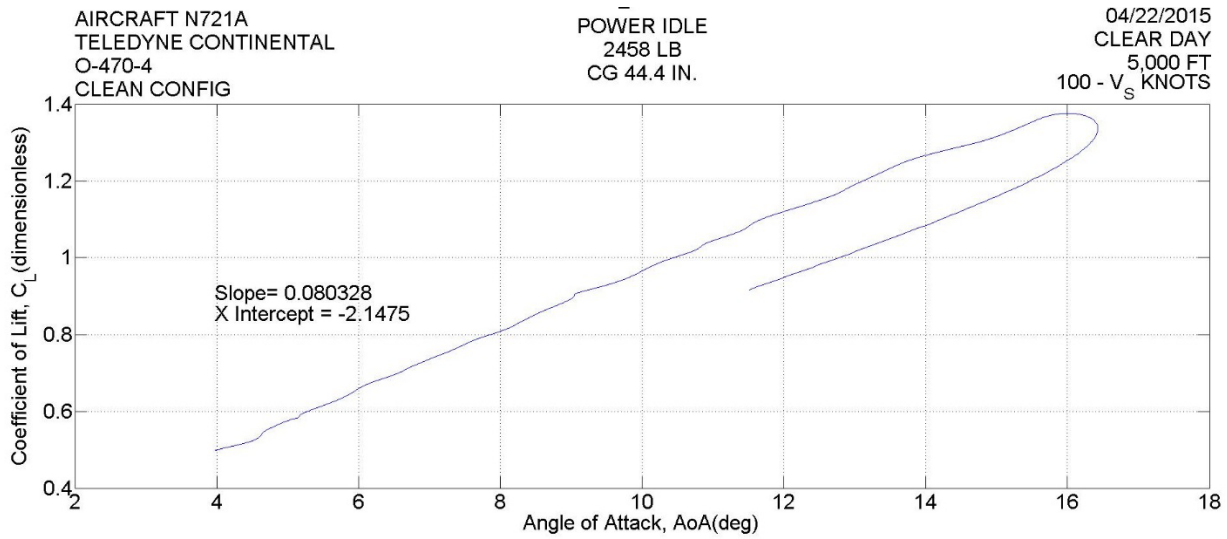

Figure B-30. Stall 2 lift coefficient vs. AoA

Figures B-32 and B-33 show the calibrated airspeeds of the Cessna 182Q during the stalls. The average bleed rate observed for Stall 1 was 0.80 knots per second; for Stall 2, it was 0.68 knots per second, a 15.97% difference. The differences in bleed rate will cause variations in the lift coefficient and change observed aerodynamic behavior. These effects can cause the maximum coefficient of lift and the stall AoA to increase with increased bleed rate. This could explain why Stall 1 has a larger maximum coefficient of lift and stall AoA than Stall 2. Figures B-34 and B-35 show the calibrated AoA of the Cessna 182Q during the stalls.

The weight difference between the two stalls is 5.4 lb., a difference of 0.19%—resulting in a negligible change in maximum lift coefficient.

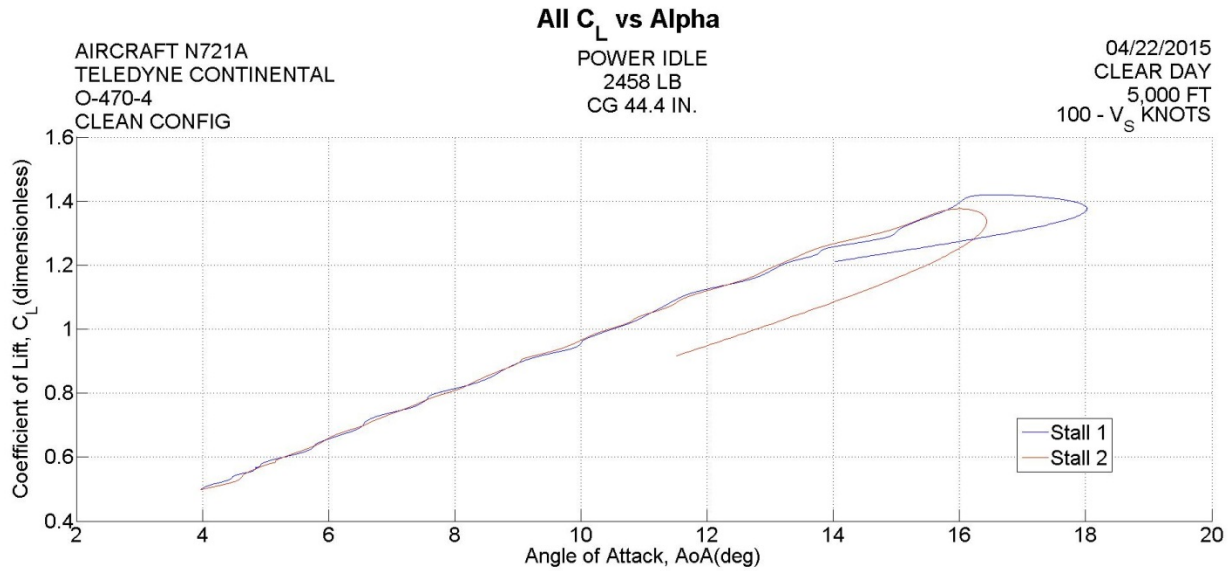

Figure B-31. Comparison between stalls 1 and 2

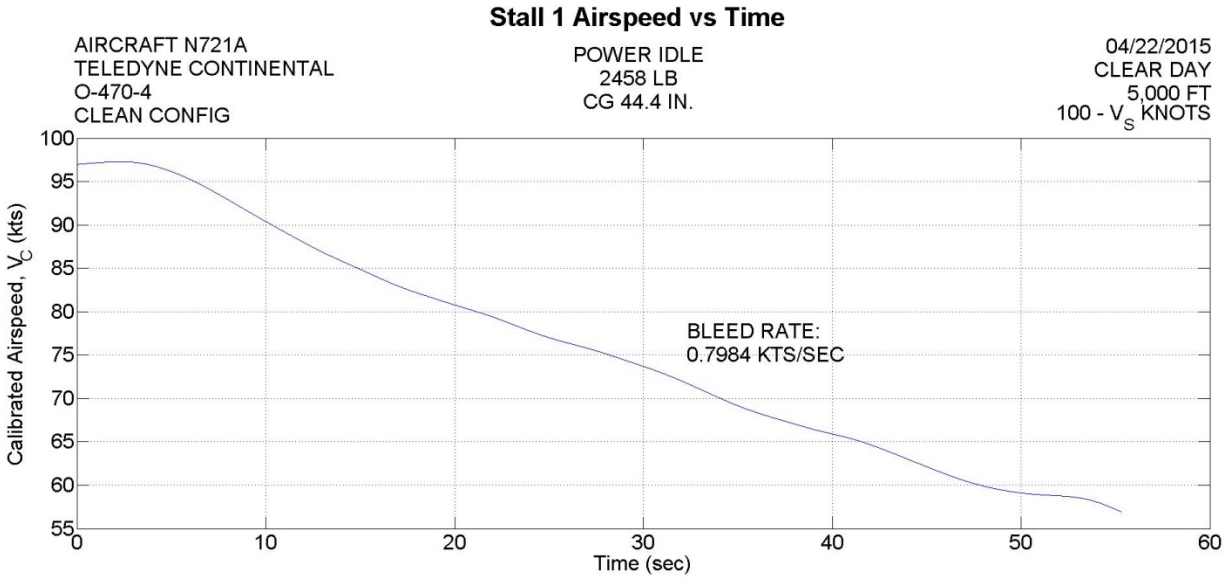

Figure B-32. Calibrated airspeed during stall 1

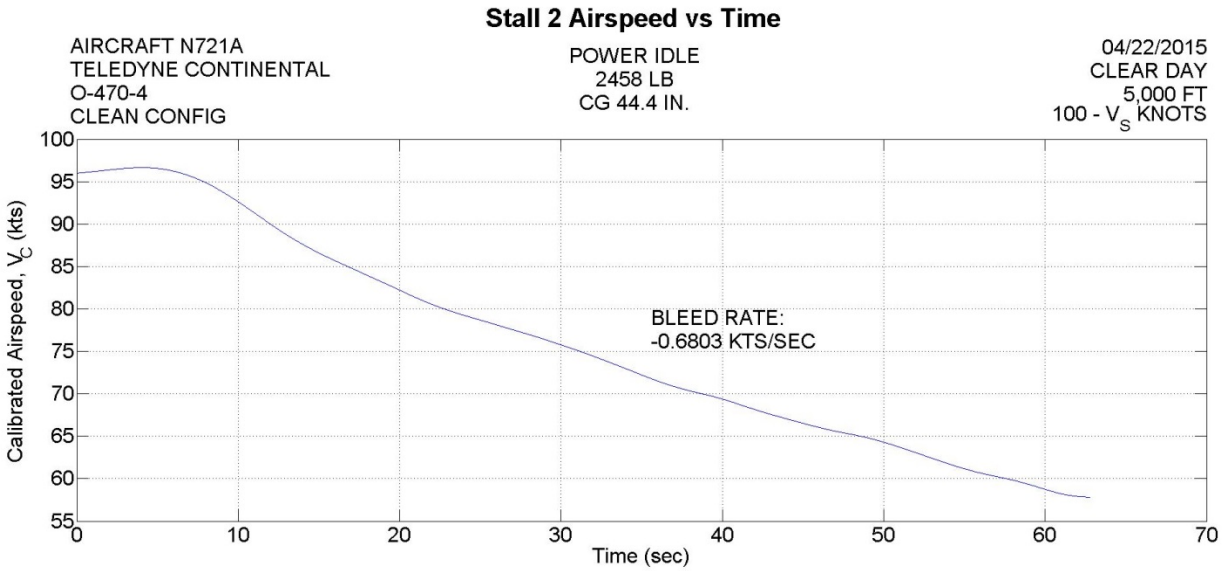

Figure B-33. Calibrated airspeed during stall 2

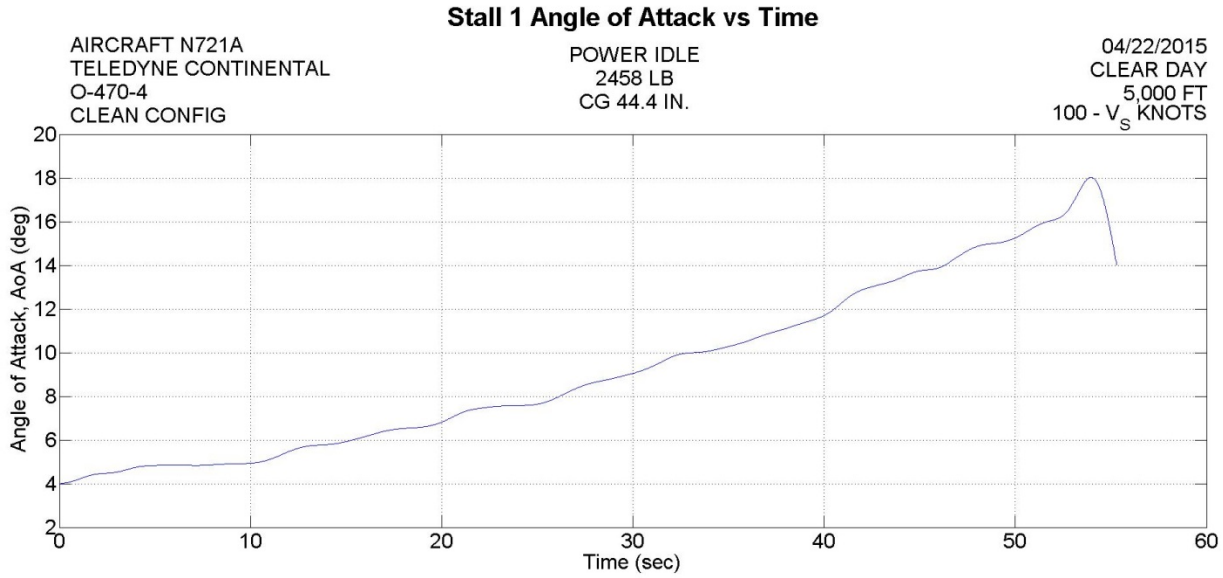

Figure B-34. Calibrated AoA during stall 1

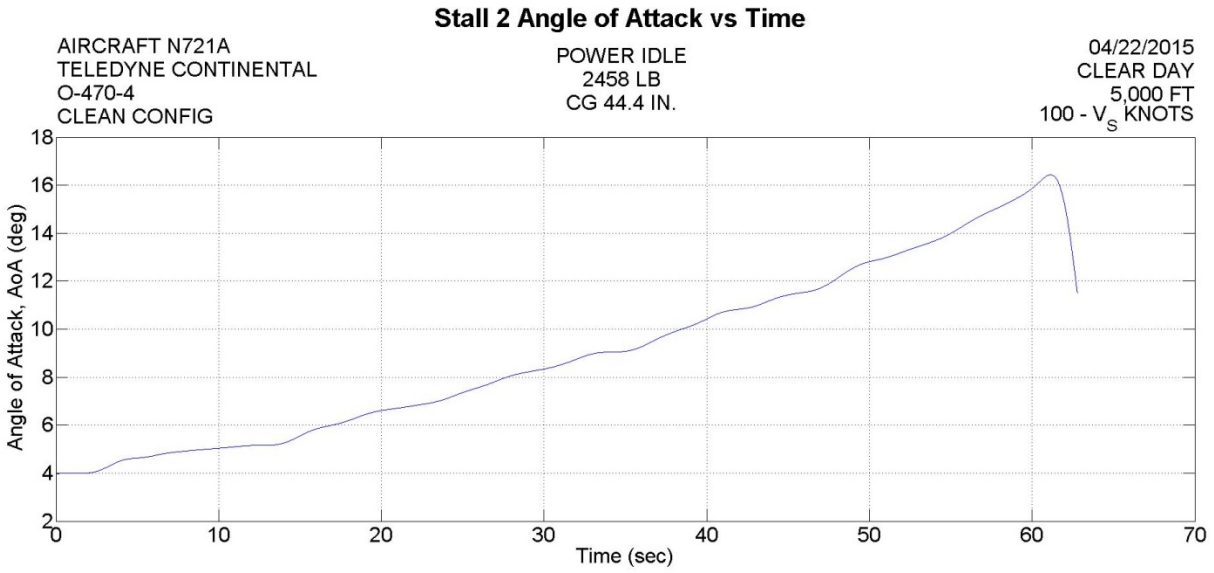

Figure B-35. Calibrated AoA during stall 2

The theoretical value for the lift curve slope of the Cessna 182Q was estimated at 0.08 per degree. Comparing this theoretical value to each individual stall, Stall 1 showed a difference of 0.057%, with a 0.41% difference for Stall 2. The average of the data was 0.0800 per degree, which has 0 difference. Significant figures failed to capture the exact difference. The NACA 2412 airfoil in this aircraft has a maximum coefficient of lift of 1.5–1.7 at a geometric AoA of approximately 16º, depending on the aerodynamic center location and atmospheric conditions. With the assumption that 90% of the airfoil max lift coefficient can estimate the theoretical max lift coefficient of the aircraft, the Cessna 182Q should have a theoretical value of 1.44 for the max lift coefficient. The average max coefficient of lift value was 1.40, a 2.86% difference from the theoretical value. The average geometric stall AoA was 16.25º, differing by 1.55% from the airfoil's theoretical value.

The calibration methods showed a parabolic relationship for dV_{pc} and dH_{pc}, whereas the position error correction remained fairly constant. The dV_{pc} correction factor peaks at 94 KIAS at an approximate value of 4.5 knots. Compared to the POH data, the velocity pressure position corrections at each indicated airspeed show a largest error of 7.7%. The dH_{pc} correction factor peaks at approximately 110 KIAS with an approximate value of 43'. Furthermore, the results of the upwash calibration determined that as the AoA increases, the upwash correction also increases. A validation of these results was done by using two different methods to reach the same conclusion, showing a 13.3% difference in $\Delta\alpha$ at an α of 10º. The last flight test technique showed that the maximum lift coefficient and stall AoA had errors of 5.71% and 12.1%, respectively.

APPENDIX C—AERODYNAMICS OF WHY A LINEAR CALIBRATION WORKS

Six frame grabs from a 1938 NACA film [19] are shown in figure C-1. These images illustrate the underlying principle that results in a linear calibration curve for under-wing mounted differential AoA probes. The airfoil in the frame grabs is a symmetrical airfoil.

The pressure on the surface of the airfoil referenced to the free stream (atmospheric) pressure is positive in the vicinity of the stagnation point but generally negative on the upper surface and may be negative or positive on the lower surface (figure C-2). Generally, other than near the stagnation point, if the pressure relative to the atmosphere pressure is positive on the lower surface, it is positive at low AoA near the trailing edge or when flaps are deployed.

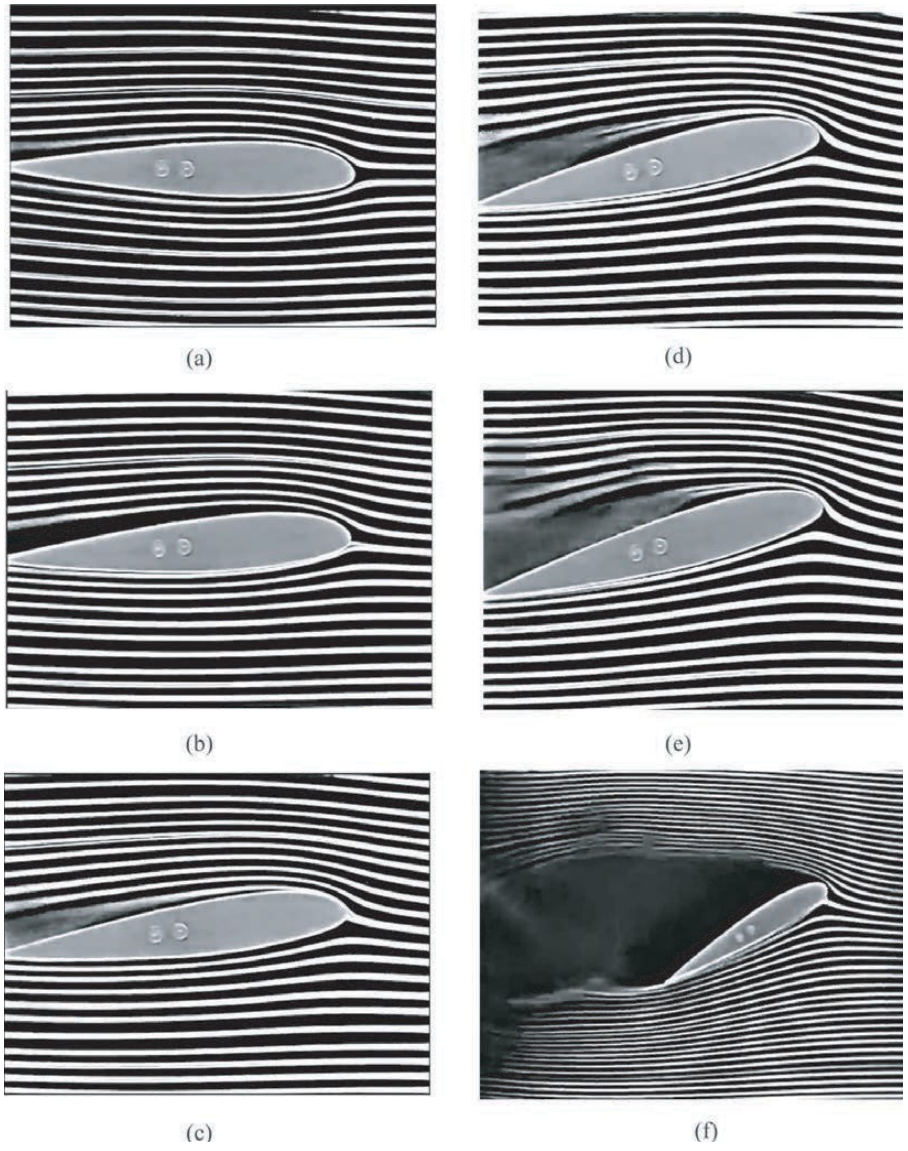

Figure C-1. Frame grabs showing the streamlines around an airfoil without flaps extended

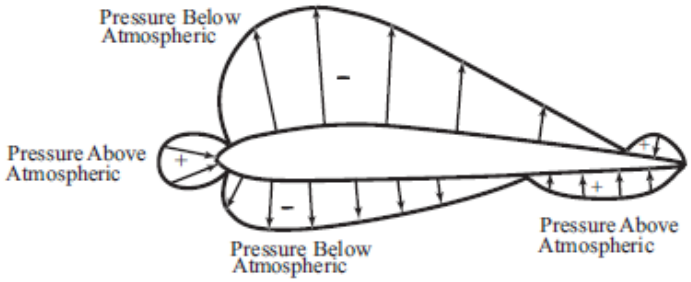

Figure C-2. Sketch of the pressure distribution on the surface of a typical airfoil

Returning to figure C-1, notice that the pressure is below atmospheric pressure except near the leading and trailing edges. Therefore, the pressure is increasing away from the airfoil surface. Because P_{fwd} has a significant dynamic pressure component for typical AoA, P_{fwd} is larger than P_{45}. Therefore, provided that the AoA probe is mounted behind the forward stagnation positive pressure region and ahead of the trailing edge positive pressure region, the P_{fwd}/P_{45} pressure ratio smoothly varies as the AoA changes. The data from the current flight tests suggest that the variation is linear.

A careful look at figures C-1(a)–C-1(f) reveals that figure C-1(a) is at 0 AoA, and AoA increases in each of the successive figures (b–f). Also notice that the 11th and 12th streamlines from the bottom of figure C-1(a) pass above and below the airfoil, respectively.

There is a streamline between the 11th and 12th streamlines (not shown) that impacts exactly on the nose of the airfoil. That streamline is called the stagnation streamline; the point where it impacts the airfoil is called the stagnation point. At the stagnation point, all the energy of motion in the airflow is converted to pressure—the stagnation pressure. The stagnation pressure is larger (positive) with respect to the static (atmospheric) pressure in the free stream.

Now notice that the 11th streamline from the bottom in figure C-1(a) passes just below the airfoil, as does the 11th streamline in figure C-1(b). However, in figure C-1(c), the 11th streamline passes just above the airfoil, as does the 11th streamline in figures C-1(d) and C-1(e). This means that as the AoA increases, the stagnation point and stagnation streamline move below the nose of the airfoil. This is also true in figure C-1(f), but more streamlines are shown, so it is no longer between the 11th and 12th streamlines; however, the 22nd line from the bottom appears to be the stagnation streamline itself.

The pressure on the surface of the airfoil referenced to the free stream (atmospheric) pressure is positive in the vicinity of the stagnation point but generally negative on the upper surface and may be negative or positive on the lower surface (figure C-2). Generally, other than near the stagnation point, if the pressure relative to the atmosphere pressure is positive on the lower surface, it is positive at low AoA near the trailing edge or when flaps are deployed.

Returning now to figure C-1, notice that the flow over the upper surface of the airfoil continues to separate as the AoA increases, until it is fully separated (stalled) in figure C-1(f). However, looking at the bottom surface of the airfoil, notice that the flow along the surface is smooth and unseparated

at any AoA shown. Thus, a bottom-mounted AoA probe is operating in a smoothly varying pressure field. The pressure far away from the airfoil surface must return to freestream (atmospheric) pressure.

Figure C-3 shows several frame grabs from the video [19] for the same airfoil with a flap deployed. Again, the streamlines on the lower surface are smooth and remain smooth with increasing AoA. Therefore, the pressure field on the bottom of the airfoil is also smooth. Thus, the AoA probe behaves in a similar manner as without a flap deployed.

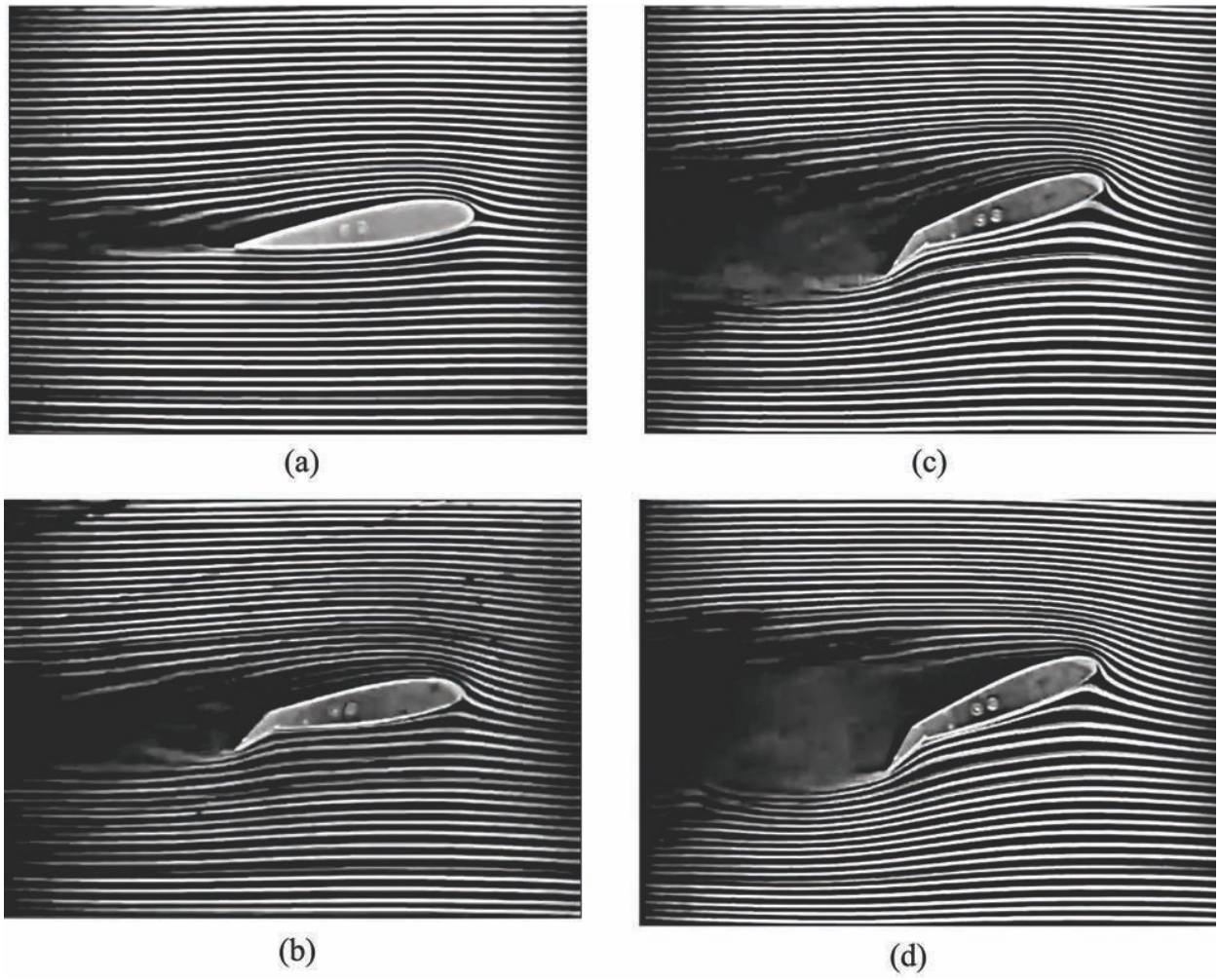

Figure C-3. Frame grabs showing the streamlines around an airfoil with flaps extended

APPENDIX D—THE EFFECT OF THE AVERAGE OF AN AVERAGE

The difference in angle of attack (AoA) for a given value of P_{fwd}/P_{45} is likely a result of the method used to determine both the AoA and P_{fwd}/P_{45}. Specifically, the noload value used in the April 22, 2015 flight test was determined by averaging 100 data points and was not changed, nor should it have been, for the two flight tests on May 26/27 and August 18/19, 2015. The 100 values for P_{fwd}/P_{45} for each leg of the 4-leg global position system (GPS) horseshoe heading box pattern were averaged—and the four averaged values were then averaged again. The four TAS determined from each of the triads of the 4-leg GPS horseshoe heading data were averaged to obtain the TAS for each data point. In short, the values represented by the data points are an average of an average. Finally, the calibration curve was determined by a statistical fit to the averaged data.

To illustrate the effect of averaging the averages, consider figure D-1, which shows the data from the DFRDAS-2 for a single leg of the 4-leg GPS run at an indicated speed for $V_{L/Dmax}$ at a pressure altitude of 6000'. The red data symbols and the red axis show the variation in P_{fwd}/P_{45}, whereas the solid red line shows the average of the 100 data points at 1.868. The standard deviation is 0.028, whereas the maximum deviation is 0.075 at a time of approximately 7.53 minutes. Recall that the AoA is derived from P_{fwd}/P_{45}.

The blue data symbols show the variation in AoA, whereas the solid blue line shows the average of the 100 data points as 10.43°. The standard deviation is 0.49°. However, the maximum deviation for this data set is 1.33°, again at a time of approximately 7.53 minutes, as expected.

In addition to the effect of the average of an average, there is ringing of the transducer in the pressure sensor, which accounts for 1/4% of full scale (i.e., 1/4% of 1.0 psi, or 0.0025 psi).

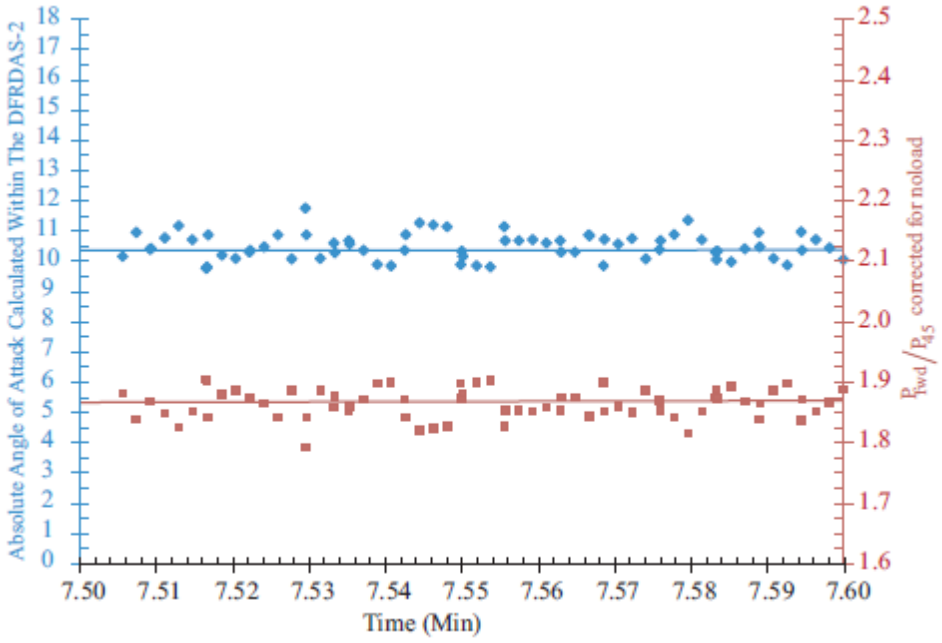

Figure D-1. Values for AoA and P_{fwd}/P_{45} from DFRDAS-2 for one leg of the 4-leg GPS data point for $V_{L/Dmax}$ for the May 26, 2015 flight test

APPENDIX E—THE RESPONSE OF THE DFRDAS TO VARIOUS STALL CONFIGURATIONS

Below is a series of graphs pertaining to the response of the DFRDAS to various stall configurations. The available configurations are detailed in table E-1. The flap angle was measured between the upper wing surface of the right wing just ahead of the flap and at the flap trailing edge approximately 5″ outboard of the fuselage. A digital inclinometer was used.

Unless otherwise stated, all stalls were performed as standard FAA stall (i.e., using a deceleration of one KIAS per second). Accelerated stalls were performed using a deceleration of five KIAS per second. All banks are to the right.

Table E-1. Stall series

Figure	Flaps	Bank	Accelerated
E-1	0	0	No
E-2	0	20	No
E-3	0	30	No
E-4	0	0	Yes
E-5	0	0	Yes
E-6	21.5	0	No
E-7	21.5	20	No
E-8	21.5	30	No
E-9	21.5	0	Yes
E-10	30	0	No
E-11	30	20	No
E-12	30	30	No
E-13	30	0	Yes
E-14	40	0	LCO

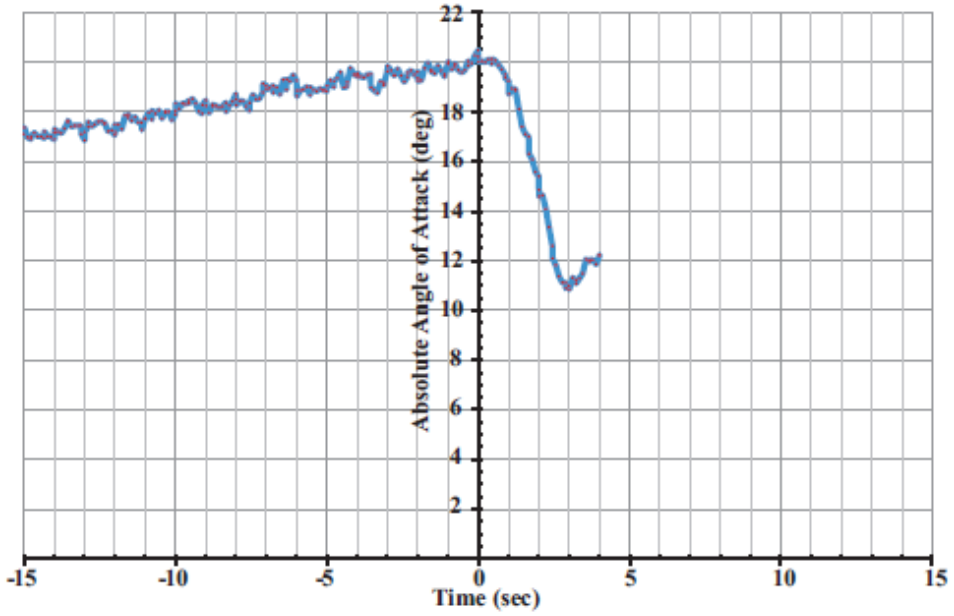

Figure E-1. FAA standard stall with flaps 0° and bank 0° DFRDAS-2 probe on the right wing at 38.9% of the local chord

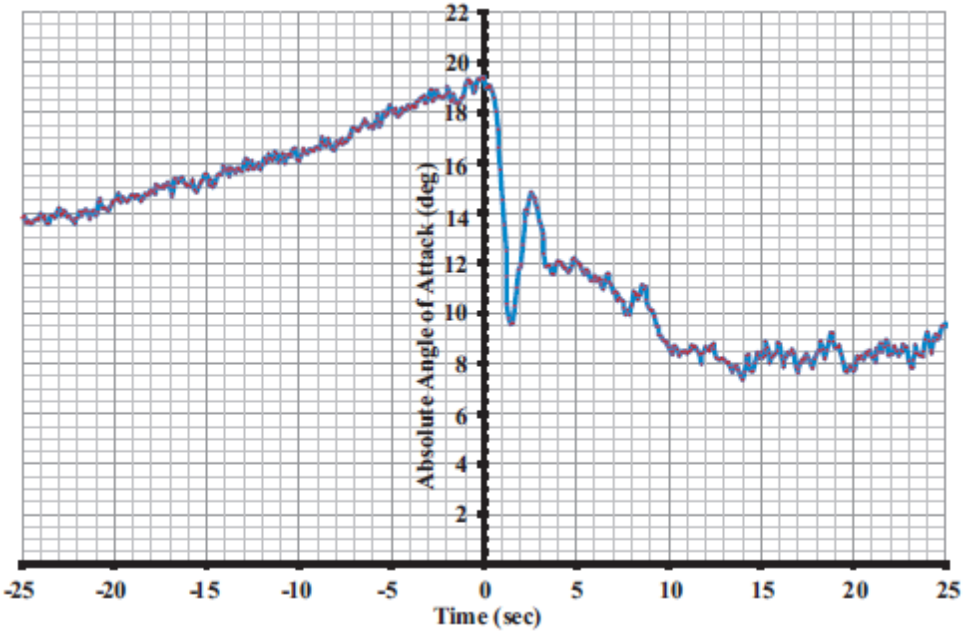

Figure E-2. FAA standard stall with flaps 0° and bank 20° DFRDAS-2 probe on the right wing at 38.9% of the local chord

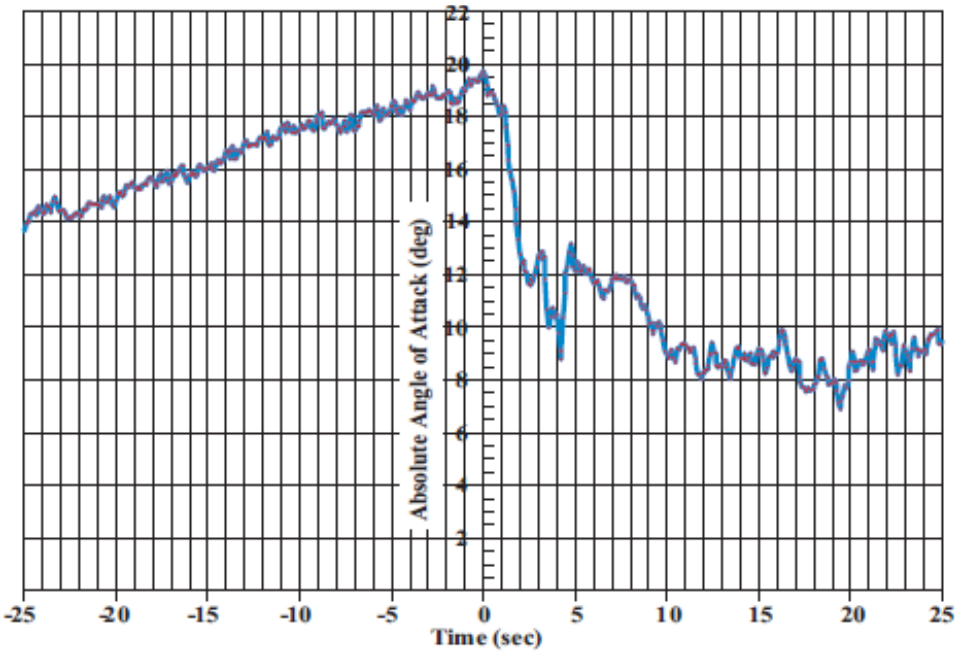

Figure E-3. FAA standard stall with flaps 0° and bank 30° DFRDAS-2 probe on the right wing at 38.9% of the local chord

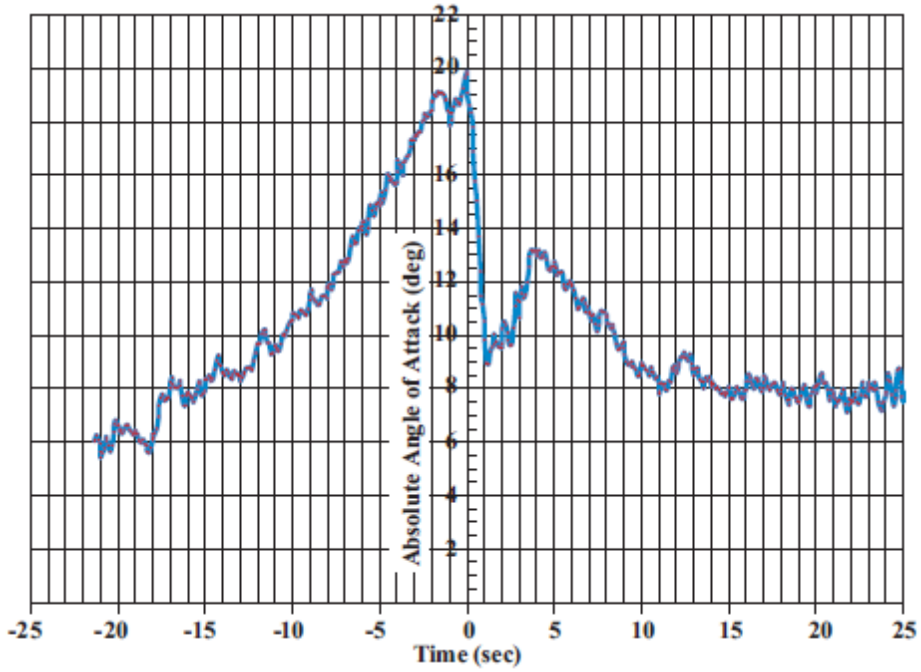

Figure E-4. FAA accelerated stall with flaps 0° and bank 0° DFRDAS-2 probe on the right wing at 38.9% of the local chord

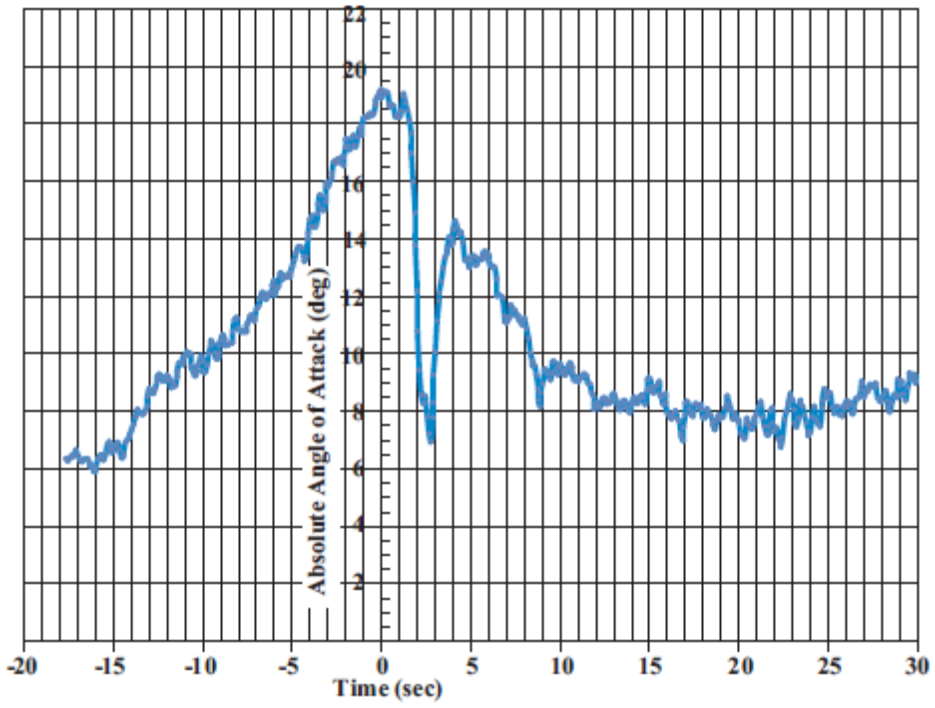

Figure E-5. FAA accelerated stall with flaps 0°and bank 0° DFRDAS-2 probe on the right wing at 38.9% of the local chord

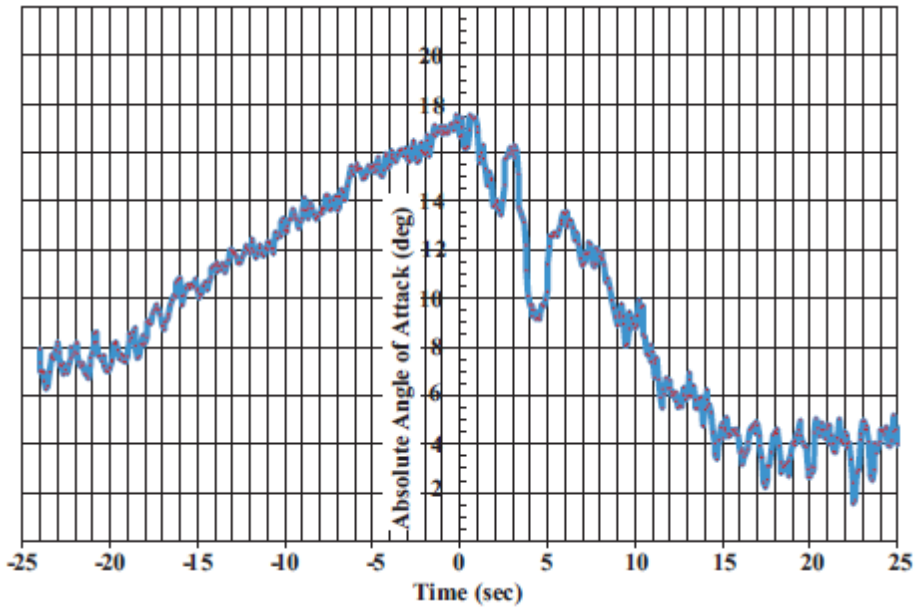

Figure E-6. FAA accelerated stall with flaps 21.5° and bank 0° DFRDAS-2 probe on the right wing at 38.9% of the local chord

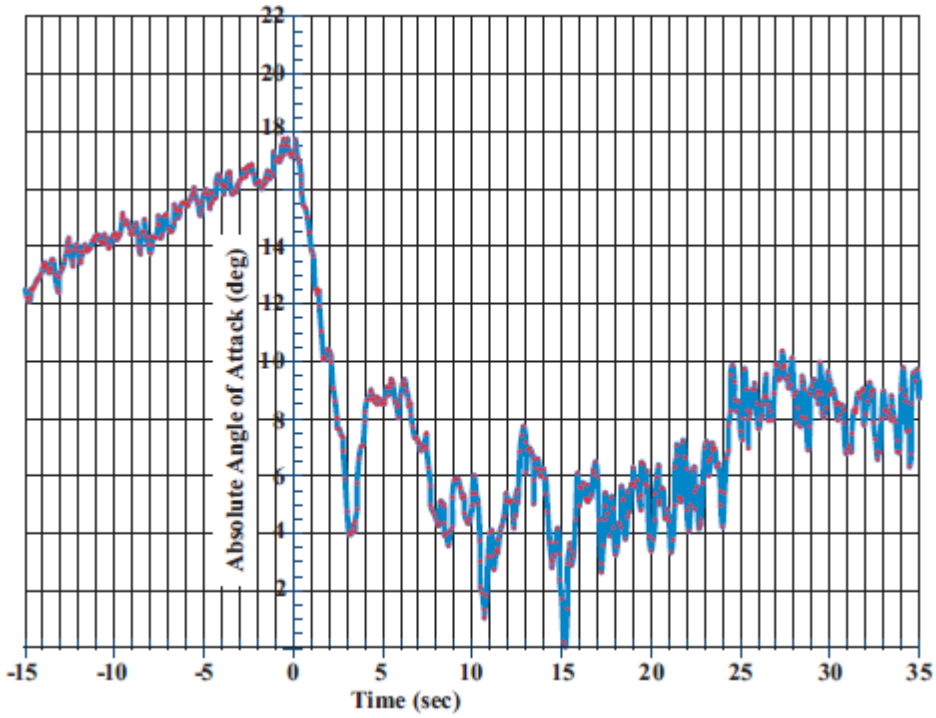

Figure E-7. FAA standard stall with flaps 21.5° and bank 20° DFRDAS-2 probe on the right wing at 38.9% of the local chord

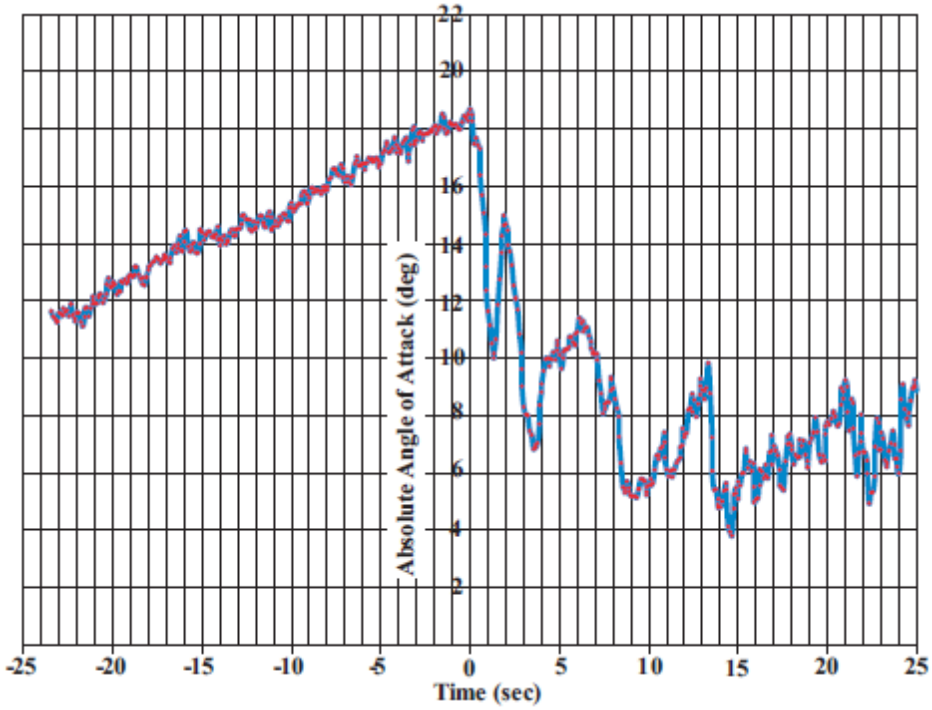

Figure E-8. FAA standard stall with flaps 21.5° and bank 30° DFRDAS-2 probe on the right wing at 38.9% of the local chord

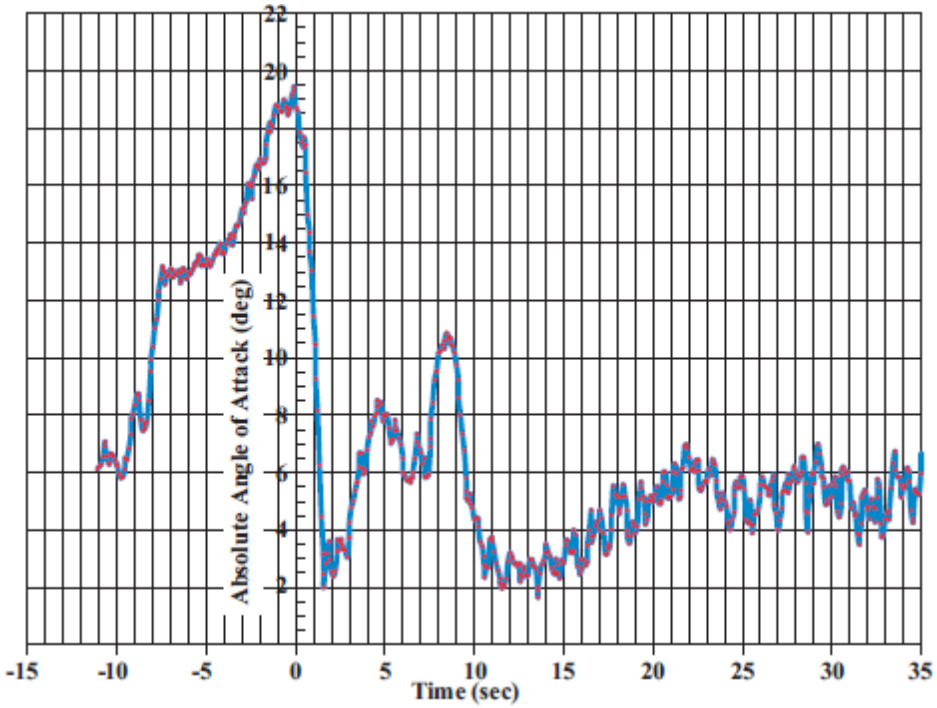

Figure E-9. FAA accelerated stall with flaps 21.5° and bank 0° DFRDAS-2 probe on the right wing at 38.9% of the local chord

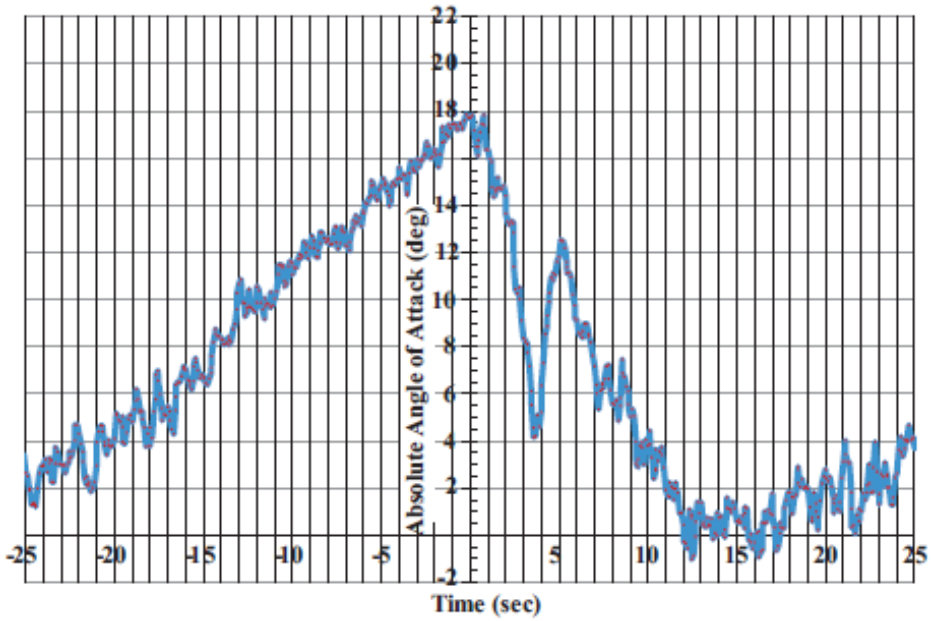

Figure E-10. FAA standard stall with flaps 30° and bank 0° DFRDAS-2 probe on the right wing at 38.9% of the local chord

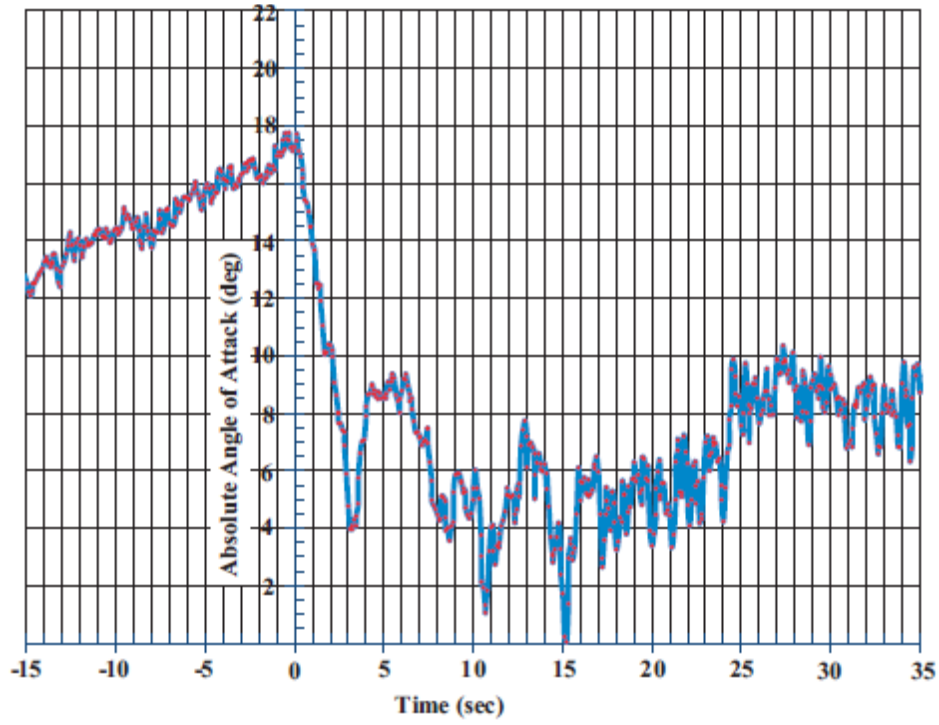

Figure E-11. FAA standard stall with flaps 30° and bank 20° DFRDAS-2 probe on the right wing at 38.9% of the local chord

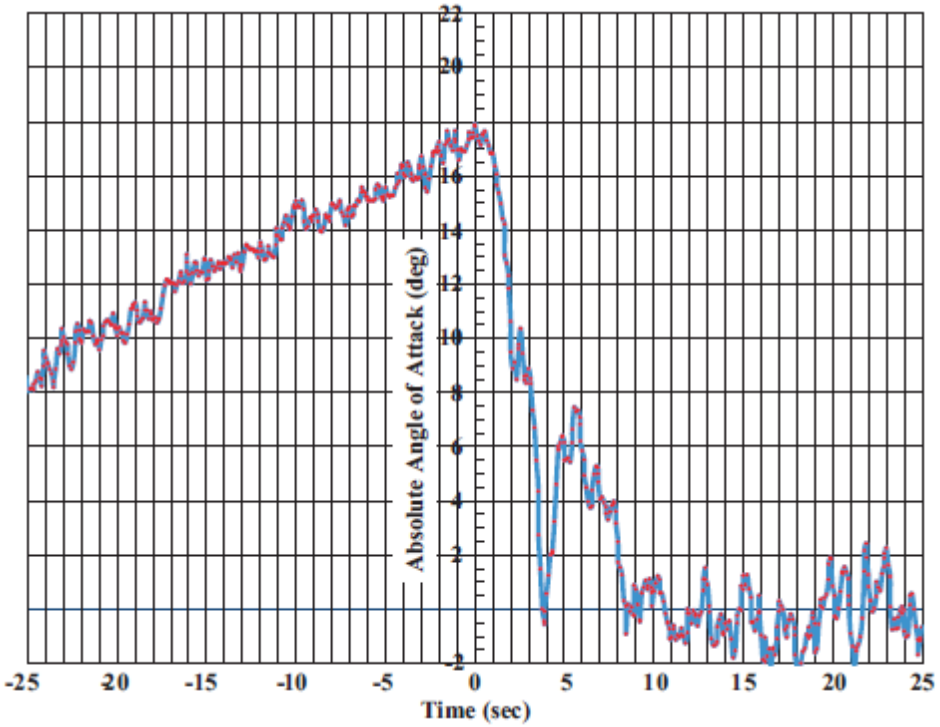

Figure E-12. FAA standard stall with flaps 30° and bank 30° DFRDAS-2 probe on the right wing at 38.9% of the local chord

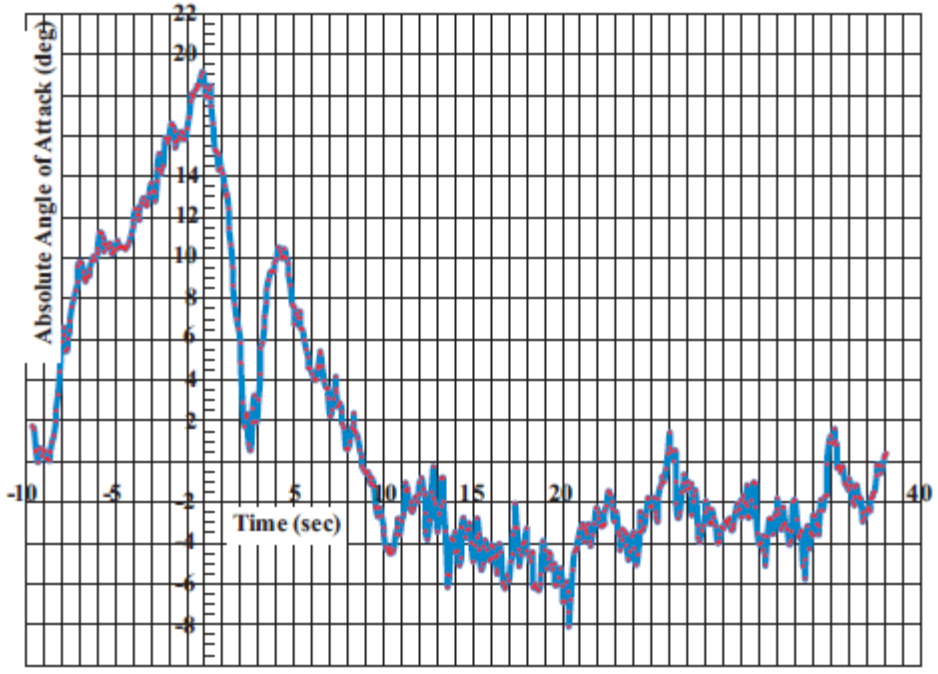

Figure E-13. FAA accelerated stall with flaps 30° and bank 0° DFRDAS-2 probe on the right wing at 38.9% of the local chord

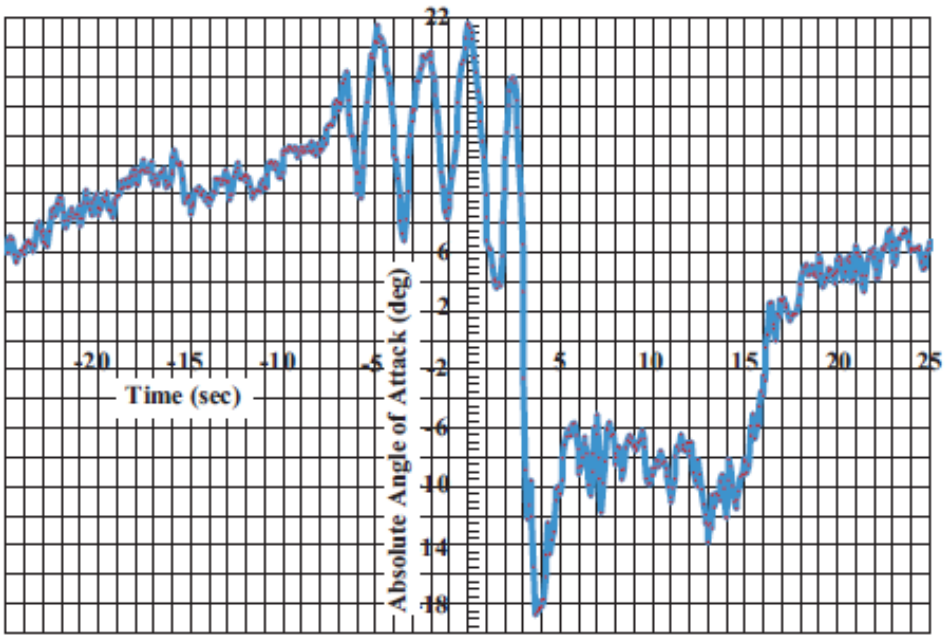

Figure E-14. FAA standard stall with flaps 30° and bank 30° DFRDAS-2 probe on the right wing at 38.9% of the local chord. This is a four-cycle limit cycle oscillation

EFRC SAFETY FINDING

SAFETY FINDING TITLE
FUNCTIONAL CHECK FLIGHT

PROJECT	AIRCRAFT (N NUMBER)	DATE
FAA-AOA-GRANT	Cessna 182Q (N721A)	April 2015

CONCLUSION AND RECOMMENDATIONS

1. A Hazards Review was completed on 01 April 2015 for the Federal Aviation Administration (FAA) Angle Of Attack (AOA) grant flights. These flights include functional check flights in Daytona Beach, Florida (KDAB). All Hazard Reports, hazard mitigations, and safety related issues were identified, discussed, assessed, and assigned an appropriate Hazard Risk and Probability after all hazard mitigations were applied.

2. A total of 4 Hazards were identified for this mission.

   - HR-AOA-02 In flight collision with other aircraft I-E
   - HR-AOA-03 Injury or Emergency egress blockage due to loose equipment I-E
   - HR-AOA-04 Electrical fire and smoke I-E
   - HR-AOA-05 Air data boom structural failure I-E

   All four hazards were assigned a I-E

3. In addition to the FAR's the following flight limitations were identified for the flight(s).

   - All flights must be conducted in VMC (no flight through visible moisture).
   - No over-water flight below 1,000 FT AGL.
   - No flight operations / RTB if lightning is observed within 25 nm radius.

4. The following Mission Rules were identified for the flight(s).
   For All Flight Operations:

   - Minimum flight crew is two qualified pilots.
   - One pilot will maintain visual look-out for traffic at all times.
   - Attempt to remain in communication with airspace controlling agency at all times.
   - Attempt to remain in positive radar contact at all times.

A structural functional check flight was completed on 31 March 2015 for the FAA Angle of Attach research mission. The following conclusions and recommendations are made:

1. No handling or structural anomalies up to +2.5/-0.5g's and 157 KIAS.
2. When the air data boom is installed V_{NE} is 143 KIAS. All others speeds are as outlined in the POH.
3. Mitigations and controls for all hazards are adequate for safe flight.
4. Air data boom flights are approved.

NAME / SIGNATURE	DATE
Scott Martin	4/1/15

Figure F-1. EFRC safety finding

EFRC FLIGHT PERMIT (FP)

FLIGHT PERMIT TITLE
MISSION FLIGHTS

PROJECT	**AIRCRAFT (N NUMBER)**	**DATE**
FAA-AOA-GRANT	Cessna 182Q (N721A)	April 2015

FLIGHT ACTIVITY *(Specify type of flight operation.)*

☒ Flight Research ☐ Flight Training / Proficiency

☐ Flight Support ☐ **Other (Specify):** _____

FLIGHT LIMITATIONS *(List aircraft and flight limitations due to experimental hardware, software, weather conditions, pilot qualification, allowable aircrew, etc.)*
Flight Limitations in addition to the FAR's:

1. All flights must be conducted in VMC (no flight through visible moisture).
2. No over-water flight below 1,000 ft AGL.
3. No flight operations / RTB if lightning is observed within 25 nmi radius.
4. All flight operations will be conducted within the normal operating limits of the aircraft with the following limitations: the maximum load factor is restricted to +2.0g and 0.0g and the maximum allowable airspeed is restricted to 143 KIAS (V_{NO}).

Mission Rules For All Flight Operations

1. Minimum flight crew is one qualified pilot.
2. Attempt to remain in communication with airspace controlling agency at all times.
3. Attempt to remain in positive radar contact at all times.

CONTACT INFORMATION *(List personnel responsible for engineering and operations.)*
Engineering: Agustin Giovagnoli / EFRC, (386) 506-2340
Aircraft Maintenance: Daniel Stinelli / EFRC, (239) 287-1622
Flight Operations: Pat Anderson / EFRC, (386) 323-8876
Instrumentation / Systems: Daniel Stinelli / EFRC, (239) 287-1622
Science / Principal Investigator: Borja Martos / EFRC, (386) 323-8870

SIGNATURE / DATE (Head of Flight Operations)

4/1/2015

Figure F-2. EFRC flight permit

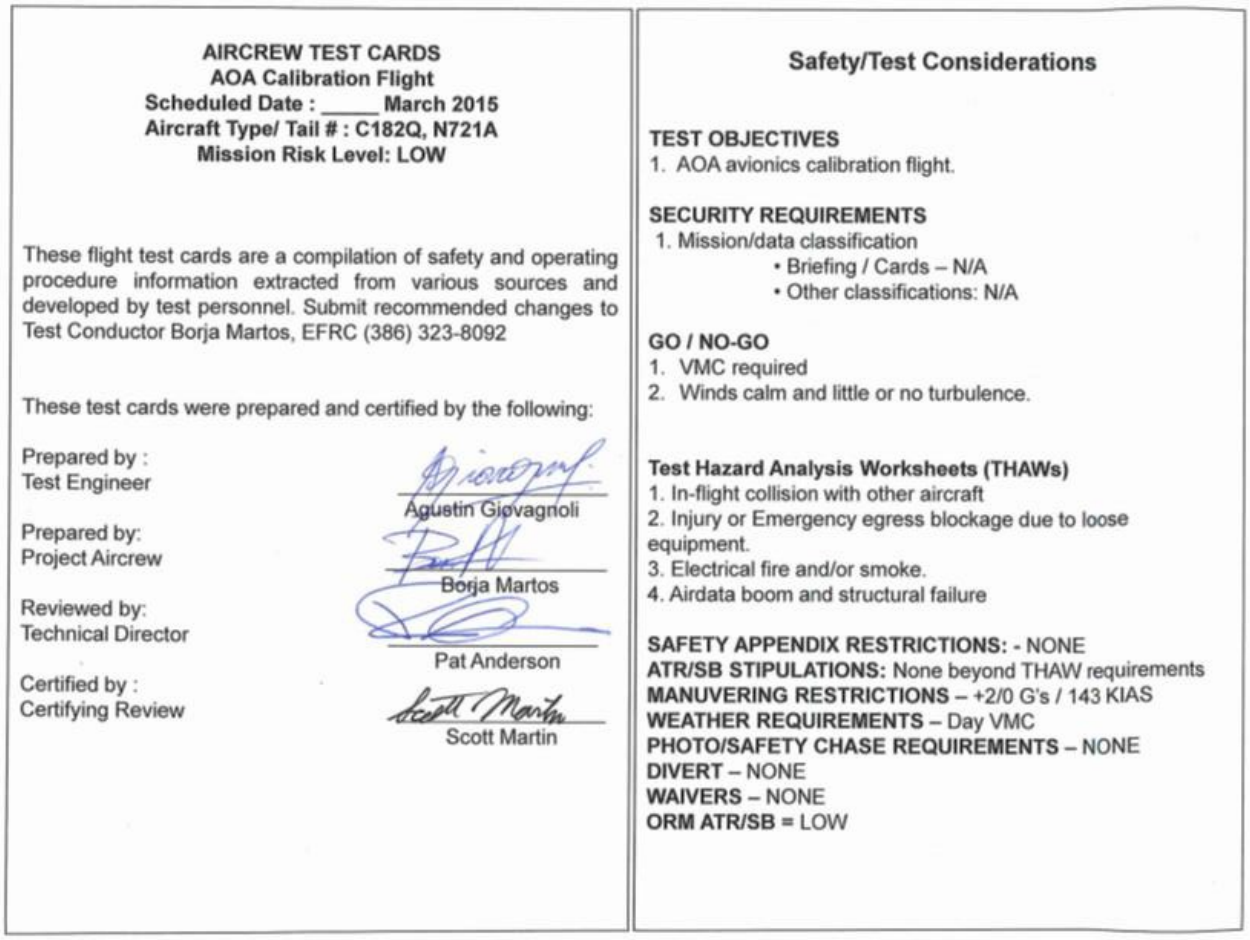

AIRCREW TEST CARDS
AOA Calibration Flight
Scheduled Date : _____ March 2015
Aircraft Type/ Tail # : C182Q, N721A
Mission Risk Level: LOW

These flight test cards are a compilation of safety and operating procedure information extracted from various sources and developed by test personnel. Submit recommended changes to Test Conductor Borja Martos, EFRC (386) 323-8092

These test cards were prepared and certified by the following:

Prepared by :
Test Engineer
Agustin Giovagnoli

Prepared by:
Project Aircrew
Borja Martos

Reviewed by:
Technical Director
Pat Anderson

Certified by :
Certifying Review
Scott Martin

Safety/Test Considerations

TEST OBJECTIVES
1. AOA avionics calibration flight.

SECURITY REQUIREMENTS
1. Mission/data classification
   - Briefing / Cards – N/A
   - Other classifications: N/A

GO / NO-GO
1. VMC required
2. Winds calm and little or no turbulence.

Test Hazard Analysis Worksheets (THAWs)
1. In-flight collision with other aircraft
2. Injury or Emergency egress blockage due to loose equipment.
3. Electrical fire and/or smoke.
4. Airdata boom and structural failure

SAFETY APPENDIX RESTRICTIONS: - NONE
ATR/SB STIPULATIONS: None beyond THAW requirements
MANUVERING RESTRICTIONS – +2/0 G's / 143 KIAS
WEATHER REQUIREMENTS – Day VMC
PHOTO/SAFETY CHASE REQUIREMENTS – NONE
DIVERT – NONE
WAIVERS – NONE
ORM ATR/SB = LOW

Figure F-3. Test cards and safety/test considerations cover

HAZARD MATRIX AND SAFETY PROCESS

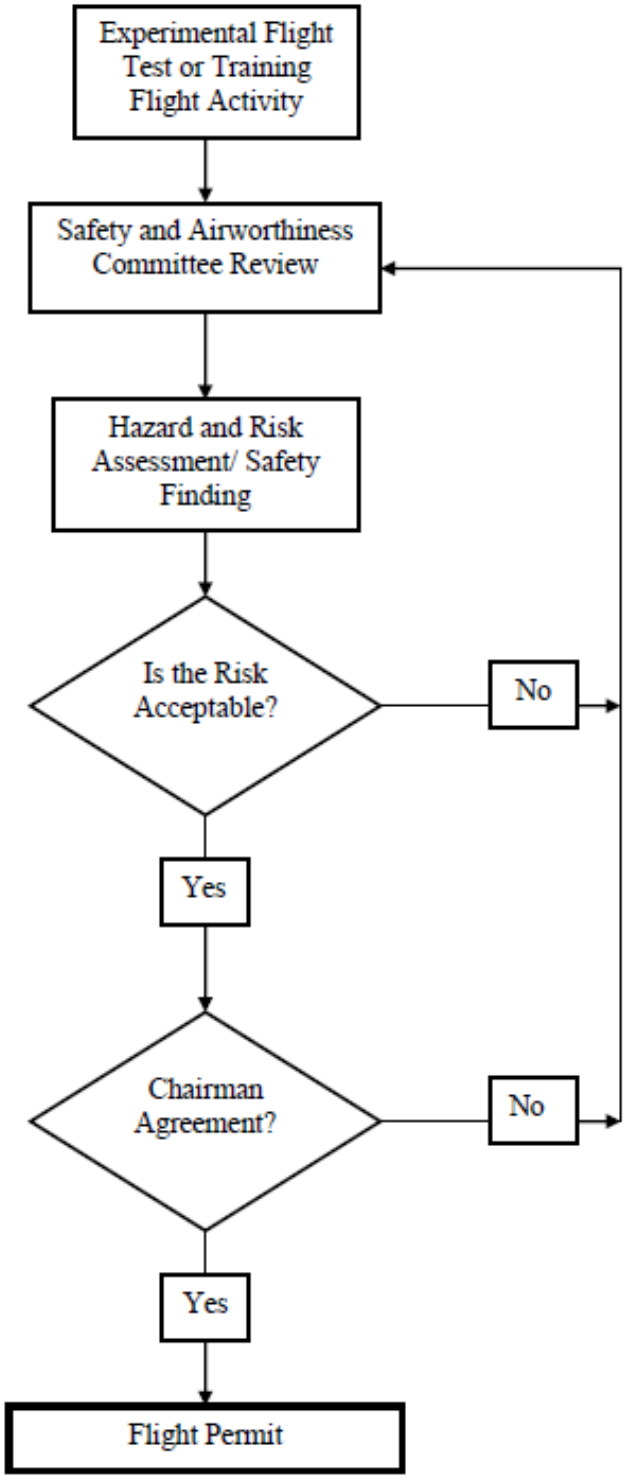

Figure F-4. Airworthiness and safety process

Table F-1. Definitions of severity categories (Reference: MILSTD-882D)

Description	Category	Environmental, Safety, and Health Result Criteria
Catastrophic	I	Could result in death, permanent total disability, or irreversible severe environmental damage that violates law or regulation
Critical	II	Could result in permanent partial disability, injuries, or occupational illness that may result in hospitalization of personnel, or reversible environmental damage causing a violation of law or regulation
Marginal	III	Could result in injury or occupational illness resulting in one or more lost work days, or mitigatable environmental damage without violation of law or regulation where restoration activities can be accomplished
Negligible	IV	Could result in injury or illness not resulting in a lost work day or minimal environmental damage not violating law or regulation

Table F-2. Mishap probability levels (Reference: MILSTD-882D)

Description	Level	Quantitative Probability	Qualitative Probability
Frequent	A	Likely to occur often in the life of an item, with a probability of occurrence greater than 10^{-1} in that life	Continuously experienced
Probable	B	Will occur several times in the life of an item, with a probability of occurrence less than 10^{-1} but greater than 10_{-2} in that life	Will occur frequently
Occasional	C	Likely to occur at some point in the life of an item, with a probability of occurrence less than 10^{-2} but greater than 10_{-3} in that life	Will occur several times
Remote	D	Unlikely but possible to occur in the life of an item, with a probability of occurrence less than 10^{-3} but greater than 10_{-6} in that life	Unlikely, but can reasonably be expected to occur
Improbable	E	So unlikely it can be assumed occurrence may not be experienced, with a probability of occurrence less than 10^{-6} in that life	Unlikely to occur, but possible

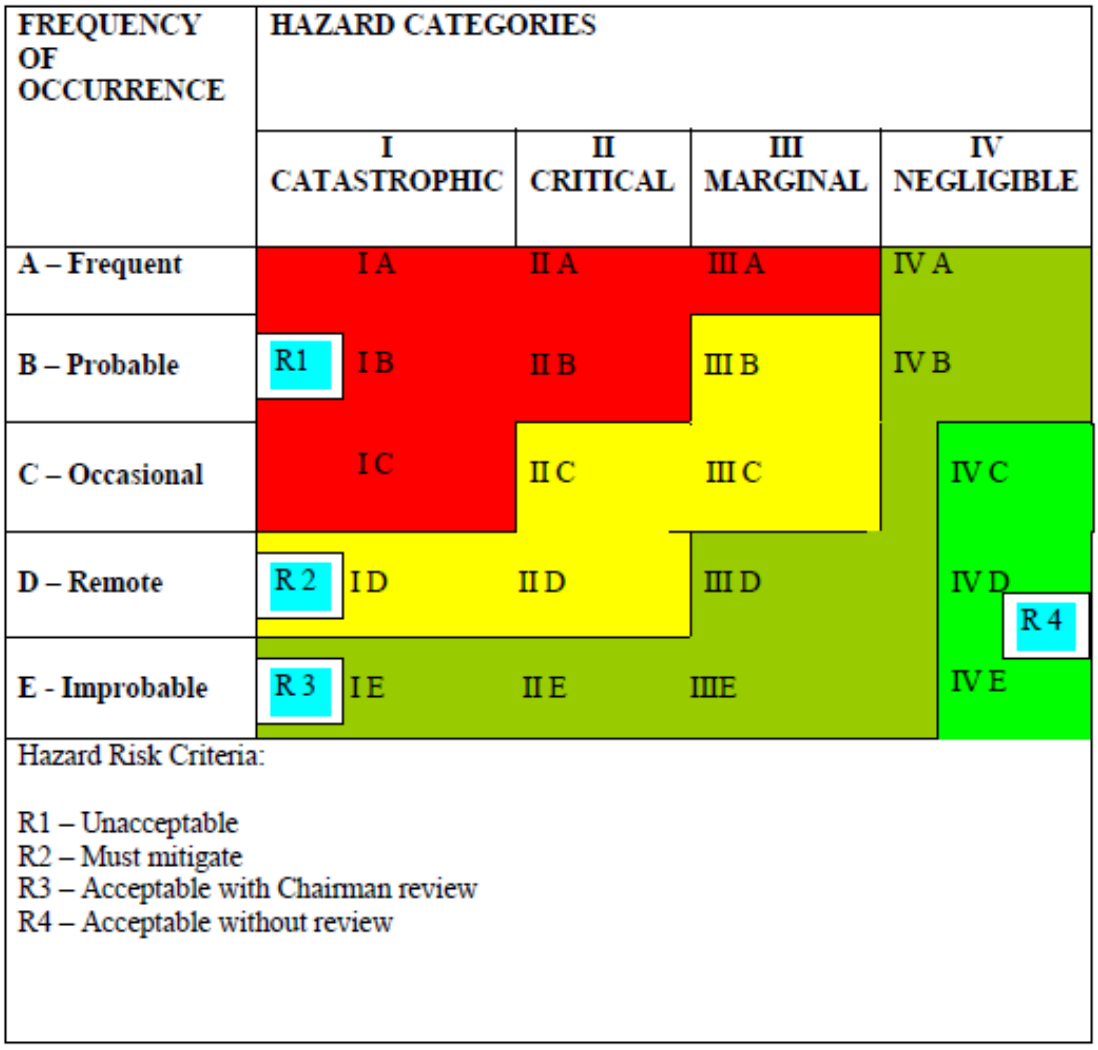

Figure F-5. Comparative risk assessment matrix (Reference: MILSTD-882C)

FLIGHT LOG

Table F-3. Flight log

Date	Flight	Pilot	Time [hr.]
15-Jan-15	FCF - FUEL SCAN	Martos	1.4
16-Jan-15	FCF - GPS 4 LEG	Martos	2.7
16-Jan-15	FCF - AUTOPILOT	Martos	1.1
20-Jan-15	KDAF-KCAE-W29 (FERRY FLT)	Martos	5.3
21-Jan-15	W29 (DATA FLT)	Martos	1.0
22-Jan-15	W29 (DATA FLT)	Martos	3.1
22-Jan-15	W29-KCAE-KDAB (FERRY FLT)	Martos	6.2
24-Mar-15	HIGH SPEED TAXI	Martos	0.5
31-Mar-15	Air Data Boom FCF	Martos	1.5
1-Apr-15	DAS FCF & INIT ADS	Martos	1.3
7-Apr-15	INIT UPWASH CAL	Martos	1.3
14-Apr-15	ADS Calibration	Martos	2.3
16-Apr-15	Stall Flights	Martos	1.2
16-Apr-15	Depot Star Calibration	Martos	0.7
20-Apr-15	Depot Star Calibration	Martos	1.5
22-Apr-15	DFR (DATA FLT) TWO MASTS	Martos	2.0
24-Apr-15	Stall Flights	Martos	1.3
1-May-15	GPS Step Decrease	Martos	1.4
8-May-15	Checkout DAS New Laptop	Martos	1.2
12-May-15	Checkout DAS New Laptop	Martos	1.2
12-May-15	Stall Flights - Defeat Guidance	Martos	0.7
21-May-15	Stall Flights - Defeat Guidance	Martos	1.1
26-May-15	KDAF-KCAE-W29 (FERRY FLT)	Martos	5.5
26-May-15	W29 (DATA FLT)	Martos	2.0
27-May-15	W29 (DATA FLT)	Martos	1.6
15-Jun-15	W29-KDAB (FERRY FLT)	Martin	5.4
17-Aug-15	KDAF-W29 (FERRY FLT)	Martos	5.8
18-Aug-15	W29 (DATA FLT)	Martos	1.5
18-Aug-15	W29 (DATA FLT)	Martos	2.3

Table F-3. Flight log (continued)

Date	Flight	Pilot	Time
18-Aug-15	W29 (DATA FLT)	Martos	1.7
19-Aug-15	W29 (DATA FLT)	Martos	1.8
19-Aug-15	W29-KDAB (FERRY FLT)	Martos	6.7
		Total	74.3